MEASUREMENT OF ELECTRON NEUTRINO AND ANTINEUTRINO APPEARANCE WITH THE NOνA EXPERIMENT

BY

SHIQI YU

Submitted in partial fulfillment of the
requirements for the degree of
Doctor of Philosophy in Physics
in the Graduate College of the
Illinois Institute of Technology

Approved 
Advisor

Chicago, Illinois
December 2020

ACKNOWLEDGMENT

致我亲爱的爸爸妈妈，你们让我看到生活的美好。路漫漫其修远兮，吾将上下而求索。To my parents, Lihua and Xuehui, who have always supported me all these years. That is why I have come so far and can keep moving on. My office is at Argonne National Laboratory (ANL) and it is like a home to me. My adviser at ANL, Zelimir, is always there whenever I need to talk with someone. He has been as patient with me as with his little daughter Anna. When Ryan and Ranjan were there, some afternoons, I made coffee in my office, and we gathered in my office talking about NOvA and physics. Sometimes Maury came over, listening to us with a big smile like our grandpa. Maury can give us wise suggestions on everything, from the Universe to baseball games. Aleena joined ANL later, and we became friends. Dan is my adviser at Illinois Institute of Technology. He made me realize that every single detail should be taken great care of with zero tolerance for any mistakes. I learned a lot from him during my thesis writing. Bryce, Pavel, and Gady are my committee members. They gave me lots of suggestions during my Ph.D. study. My first friend on NOvA is Nitish. Later I became friends with Matt S., Liudmila, and Tomas during the 2018 analysis. There were people who impressed me with their hard work, such as Micah, Erika, Karl, and Fernanda. Alex and Chris were the conveners when I first joined the analysis group. Jeremy W., Louis, and Michael B. became my conveners later. They all gave me strong support in my analysis work, just as Adam, Jeremy H., and Oleg did in my light model tuning study. I also want to thank Peter and Tricia as our spokespersons for being dedicated to NOvA. I have seen many times their speaking out loudly for NOvA, which made me feel so proud to be a member of the NOvA collaboration. I came to Chicago in 2013 and went back to China once, in 2017. This has been a long journey for me. I've enjoyed my studies and been excited by what I've learned and the opportunity to learn even more.

TABLE OF CONTENTS

Page

ACKNOWLEDGEMENT iii

LIST OF TABLES vi

LIST OF FIGURES vii

LIST OF SYMBOLS xii

ABSTRACT xiv

CHAPTER

1. INTRODUCTION 1

2. THE NOVA EXPERIMENT 7

3. NOVA LIGHT MODEL 14

3.1. Scintillation and Cherenkov Models 15
3.2. MC Simulations 16
3.3. Selections 18
3.4. Sample Validations 19
3.5. Fitting Technique 23
3.6. Result and Systematic Studies 28

4. NOVA RECONSTRUCTION 35

4.1. Basic Reconstruction Techniques 35
4.2. Final-state Particle Reconstruction 36
4.3. Convolutional Neural Network 42
4.4. Prong CNNs 48

5. ELECTRON (ANTI)NEUTRINO ENERGY RECONSTRUCTION 61

5.1. Selection 61
5.2. Philosophy of Energy Estimator 63
5.3. Result and Discussion 66
5.4. Interaction Modes 68

6. OSCILLATION ANALYSIS 74

6.1. Disappearance Analysis 75

6.2. Appearance Analysis 87
6.3. Oscillation Result of Joint Analysis 105

7. CONCLUSION 115

BIBLIOGRAPHY 120

LIST OF TABLES

Table		Page
3.1	Composition of Selected ND Beam MC Samples	21
3.2	First Round Fitting Results	24
3.3	Second Round Fitting Results	28
3.4	Normalization Constants for Minimal χ^2 Values	33
4.1	Values of 3D Prong Purity Selections	52
4.2	Composition of Training Sample Before Selections Applied	53
5.1	Chi-square Fit Results	67
5.2	Composition of FD ν_e Signal Sample by Interaction Mode	69
6.1	Fractional Mean and Resolution Values	80
6.2	Cosmic-rejection BDT and PID Selections for Core Samples	89
6.3	Cosmic-rejection BDT and PID Selections for ν_e ($\bar{\nu}_e$) Peripheral Sample	91
6.4	PID Bin Intervals of Core Samples	91
6.5	Changes of Beam ν_e from Ancestor Fluxes in PID Bins	102
6.6	Changes of MC Components	103
6.7	Best-fit Oscillation Parameters of NOvA 2020 Analysis	109

LIST OF FIGURES

Figure		Page
2.1	Locations of detectors	7
2.2	Neutrinos at NuMI neutrino beamline	8
2.3	Forward (reversed) horn-current mode shown at the top (bottom) providing (anti)neutrino flux	8
2.4	Flux compositions of ν_μ (top) and $\bar{\nu}_\mu$ (bottom) charged current interactions at ND	10
2.5	Cartoon of NOvA detectors with a human figure shown for scale and view of PVC structure	11
2.6	Signal-processing chain of NOvA FD	13
3.1	Data and MC comparison of residual track length	20
3.2	Data and MC comparison of path length	21
3.3	Data and MC comparison of pre-calibrated energy of hits	22
3.4	MC composition of number of Cherenkov photons distributions for selected ND beam samples	22
3.5	MC composition of Birks suppressed energy deposition distributions for selected ND beam samples	23
3.6	Spectra of selected data samples that are used as input to the fit in both rounds of light model tuning	25
3.7	Spectra of selected MC samples that are used as input to the fit in the first round of light model tuning	26
3.8	Spectra of selected MC samples after fitting in the first round of light model tuning	27
3.9	Spectra of selected new MC samples after fitting in the second round of light model tuning	29
3.10	Distributions of PE per unit path length before (dashed) and after (solid) fitting in first (blue) and second (red) rounds of light model tuning	30
3.11	Energy loss per unit track length vs. residual track length distributions with red (black) histogram representing peak profile of MC (data) sample	31

3.12 Peak profiles of the $\frac{dE}{dx}$ vs. residual track length distributions from Figure 3.11 with ratio of data to MC shown at the bottom of each plot 32

4.1 Event display of a simulated electron neutrino interaction in the FD with two 2D prongs in each view [23] 37

4.2 Energy deposition patterns of 2D prongs with scales of x-axis varied by 2D prong length [23] 38

4.3 Event display of a simulated ν_e event with proton (red) and electron (purple) overlapped in xz view 40

4.4 Multiplicity distributions of unmatched 2D prongs 41

4.5 Event displays of simulated ν_μ (top), ν_e (middle), and neutral-current (bottom) events with outgoing particles labeled by MC truth . . . 43

4.6 Graphical representation of a generic CNN taking a simulated electron as input to hidden layers in gray box 44

4.7 Pixel maps of event view of the ν_e CCQE interaction in Figure 4.3 showing proton (bottom) and electron (top) trajectories well separated in yz view but overlapped in xz view 45

4.8 2×2 max pooling layer kernel sliding across input feature map to extract local maximum values and fill output feature map 47

4.9 Pixel maps of a matched 3D prong 48

4.10 Pixel maps of an unmatched 2D prong with no 2D prong in xz view and one 2D proton prong in yz view 49

4.11 Structure of 2D prong CNN 50

4.12 Loss calculated on the training data set (blue) and test data set (green), and accuracy calculated on test data set (red) as functions of iteration count 55

4.13 Unnormalized classification matrix of true labels (row) vs. predicted labels (column) with color representing number of 2D prongs in each entry 57

4.14 Column normalized matrix of true labels (row) vs. predicted labels (column) with color representing fraction of 2D prongs 57

4.15 Distributions of 2D prong CNN predicted particle ID with red histograms representing true particles and gray histograms representing all the other types of particles (background) 59

5.1 True neutrino energy distribution of selected FD MC events . . . 64

5.2 Hadronic energy vs. reconstructed electromagnetic energy distribution with color representing weighted average true neutrino energy in GeV . . . 65

5.3 Distributions of fractional energy reconstruction error with mean value of 0 and RMS value of 0.103 (0.091) for FHC (RHC) energy estimator . . . 67

5.4 Fractional energy reconstruction error along true neutrino energy distributions with flattening weight applied and pink dashes showing the bias along true energy . . . 68

5.5 Fractional energy reconstruction error distributions broken down by interaction mode . . . 69

5.6 Distributions of hadronic energy vs. EM shower energy broken down by interaction mode with flattening weight applied and color representing number of events . . . 70

5.7 Fractional energy reconstruction error along true neutrino energy distributions broken down by interaction mode with flattening weight applied and pink dashes showing the bias along true energy . . . 72

6.1 Event display of a real data ν_μ candidate in the FD . . . 76

6.2 Hadronic fraction vs. reconstructed neutrino energy spectrum of unoscillated FD selected ν_μ MC sample divided by blue curves into four quartiles with color representing number of events . . . 79

6.3 Distributions of the ND selected ν_μ data and MC samples in ν_μ analysis bins with MC normalized to the areas of data distributions to show their shapes . . . 81

6.4 Near-to-far extrapolation cartoon for the ν_μ analysis with red (blue) curves representing the original (decomposition-corrected) MC samples; top left plot showing the reconstructed ν_μ energy distributions of the ND selected data (black) and MC samples; top right plot showing the FD predicted MC samples; and bottom plots from left to right showing ND reco-to-true matrix, ND true ν_μ energy, ratio of true ν_μ energies at FD and ND, ν_μ disappearance probability curve, FD true ν_μ energy, and FD true-to-reco matrix . . . 84

6.5 MC sample distributions of reconstructed transverse momentum vs. reconstructed ν_μ energy of outgoing lepton in four quartiles with each divided into three p_t-quantiles by red curves . . . 86

6.6 Predicted FD ν_μ MC samples in four quartiles with background (gray) consisting of predicted cosmic ray background and MC background components 87

6.7 Flow chart of ν_e selection. 90

6.8 Distributions of cosmic-rejection BDT vs. PID values for FD ν_e selected data (pink circles) and MC signal (blue) samples with boxes representing cosmic ray background and red lines indicating the cut boundaries 92

6.9 Distributions of predicted ν_e and $\bar{\nu}_e$ samples in bins of PID/energy with signal (unfilled purple), cosmic ray background (light blue), and MC simulated beam background components stacked 93

6.10 Stacked true neutrino energy distributions of ND ν_μ CC flux broken down by ancestor flux type 95

6.11 Stacked true neutrino energy distributions of ND beam ν_e flux broken down by ancestor flux type 96

6.12 Reconstructed ν_μ energy distributions of ND selected ν_μ contained data (black circles) and MC (color-filled and stacked) samples . . 97

6.13 Reconstructed ν_μ energy distributions of ND selected ν_μ uncontained data (black circles) and MC (color-filled and stacked) samples . . 97

6.14 Original 2D spectrum of ancestor π^+ true momentum space (p_z, p_t) for selected contained ν_μ CC MC events from ancestor π^+ flux . . 99

6.15 Original 2D spectrum of ancestor π^+ true momentum space (p_z, p_t) for beam ν_e MC events from ancestor π^+ flux 100

6.16 Distributions of ND selected beam ν_e MC events in bins of PID/energy broken down by ancestor flux type (colored histograms), before (dash) and after (solid) BEN-Decomp 102

6.17 Distributions of ND ν_e selected data and MC (stacked) samples in bins of PID/energy before (dashed) and after (solid) decomposition corrections applied with ratio of data to MC shown at bottom . . 103

6.18 Distributions of ND $\bar{\nu}_e$ selected data and MC (stacked) samples in bins of PID/energy before (dashed) and after (solid) decomposition corrections applied with ratio of data to MC shown at bottom . . 104

6.19 Two dimensional spectra of Δm^2_{32} vs. $\sin^2\theta_{23}$ by assuming normal (left) or inverted (right) mass ordering with colors representing significance levels before FC method is applied 109

6.20 Two dimensional spectra of $\sin^2\theta_{23}$ vs. δ_{CP} by assuming normal (left) or inverted (right) mass ordering with colors representing significance levels before FC method is applied 109

6.21 Two dimensional spectra of Δm^2_{32} vs. $\sin^2\theta_{23}$ by assuming normal (left) or inverted (right) mass ordering with colors representing significance levels after FC method is applied 110

6.22 Two dimensional spectra of $\sin^2\theta_{23}$ vs. δ_{CP} by assuming normal (left) or inverted (right) mass ordering with colors representing significance levels after FC method is applied 110

6.23 Contours of 90% C.L. for $\sin^2\theta_{23}$ and Δm^2_{32} space with colors representing different experiments 111

6.24 Significance vs. oscillation parameter values by assuming normal (blue) or inverted (red) mass ordering, or assuming $\sin^2\theta_{23} > 0.5$ (solid) or $\sin^2\theta_{23} < 0.5$ (dashed) after FC method is applied . . . 112

6.25 Categorized systematic (blue) and statistical (red) uncertainties in numbers of events for predicted FD MC samples 113

6.26 Categorized systematic (blue) and statistical (red) uncertainties in oscillation parameters for predicted FD MC samples 114

7.1 Distributions of ν_μ (top) and $\bar{\nu}_\mu$ (bottom) data and predicted MC samples at FD 116

7.2 Distributions of ν_e (top) and $\bar{\nu}_e$ (bottom) data and predicted MC samples at FD 117

7.3 Electron antineutrino and neutrino combined appearance probability curves with normal (blue) and inverted (red) mass orderings, preferred values of the remaining oscillation parameters, observed data samples (black cross), and best-fit point (purple star) of NOvA 2020 analysis 118

LIST OF SYMBOLS

Symbol	Definition
e	electron
μ	muon
ν	neutrino
$\bar{\nu}$	antineutrino
θ_{ij}	mixing angle of neutrino mass eigenstate i and j
Δm^2_{ij}	difference of squared neutrino mass eigenstates i and j
δ_{CP}	charge conjugation and parity symmetry phase parameter
h	Planck's constant, 6.626×10^{-34} m^2kg/s
p	proton
e^+	positron
n	neutron
c	speed of light, 3×10^8 m/s
E	energy
t	time
$\vec{p}$	three-momentum, (p_x, p_y, p_z)
L	distance
π^+	positively charged pion
μ^+	antimuon
K^+	positively charged kaon
π^-	negatively charged pion
K^-	negatively charged kaon

K_L^0	long-lived neutral kaon
γ	photon
k_B	Birks constant
χ^2	chi-square statistic value
σ	standard deviation
β	ratio of particle speed to speed of light
E_{EM}	reconstructed electromagnetic shower energy
E_{HAD}	reconstructed hadronic shower energy
E_{reco}	reconstructed neutrino energy
E_{true}	true neutrino energy
$\in$	belong to
p_t	transverse momentum
p_z	forward momentum
$\cup$	union of two intervals

ABSTRACT

As a long-baseline neutrino oscillation experiment, the NuMI Off-axis ν_e Appearance (NOvA) experiment aims at studying neutrino physics by measuring neutrino oscillation parameters using the neutrino flux from the Main Injector (NuMI) beam. It has two functionally identical detectors. The near detector is onsite at Fermi National Accelerator Laboratory. The far detector is 810 km away from the source of neutrinos and antineutrinos, at Ash River, Minnesota. At the near detector, muon neutrinos or antineutrinos, before significant oscillations take place, are used to correct the Monte Carlo simulation. At the far detector, the neutrino and antineutrino fluxes after significant oscillations have happened are measured and analyzed to study neutrino oscillation. The NOvA experiment is sensitive to the values of $\sin^2\theta_{23}$, Δm^2_{32}, and δ_{CP}. The latest values from the NOvA 2020 analysis are as follows: $\sin^2\theta_{23} = 0.57^{+0.03}_{-0.04}$, $\Delta m^2_{32} = (2.41 \pm 0.07) \times 10^{-3}$ eV^2/c^4, and $\delta_{CP} = 0.82\pi$ with a wide 1σ interval of uncertainty. My study is focused on the neutrino oscillation analysis with NOvA, including detector light model tuning, particle classification with convolutional neural network, electron neutrino and antineutrino energy reconstruction, and oscillation background estimation. Most of my studies have been used in the latest NOvA publication and the NOvA 2020 analysis.

CHAPTER 1

INTRODUCTION

In 1930, the neutrino, a neutral particle, was introduced by W. Pauli to conserve energy and momentum in beta decay, in which a neutron transforms into a proton while emitting an electron. At that time, the energy spectrum of the outgoing electron had been observed to be continuous, which conflicted with energy conservation. The neutrino was proposed to be emitted together with the electron and to have an intrinsic angular momentum, so-called spin, of $\frac{\hbar}{2}$, where $\hbar = \frac{h}{2\pi}$ (h is Planck's constant). The neutrino interacted so weakly with matter that no one was able to detect it until 1956, when Clyde Cowan and Fred Reines performed an experiment using a nuclear reactor at Savannah River in South Carolina, USA [1]. In their experiment, antineutrinos that were produced by nuclear fission interacted in the detector through inverse beta decay ($\bar{\nu} + p \rightarrow e^+ + n$), releasing a positron and a neutron. The positron quickly annihilated with an electron producing a photon pair. The neutron could be captured by a nucleus releasing gamma rays. The coincidence of detecting both positron annihilation and neutron capture was the signal of antineutrino interactions.

Two years after the Cowan and Reines experiment, Maurice Goldhaber and his co-workers, at the Brookhaven National Laboratory, in the US, demonstrated the left-handedness of neutrinos by studying the decay products of a europium-152 source [2]. Left-handedness means the spin of the particle always points in the opposite direction as its momentum, so that when you curl the four fingers of your left hand towards the direction of spin of the particle, your thumb points along its direction of motion. When a europium-152 nucleus captures an electron, a samarium-152 nucleus along with a neutrino are produced. Then the samarium-152 may de-excite and emit a gamma ray. When the gamma ray and the neutrino are emitted back-to-back, their spin directions have to be opposite to conserve angular momentum. By measuring the

handedness of the gamma ray with a polarizing filter, they showed that the neutrinos are always left-handed. This conclusion implies that neutrinos have to be massless particles. Otherwise, according to special relativity, it would be possible to observe massive neutrinos moving in the opposite direction with the same spin direction, which would be right-handed. Since no right-handed neutrinos had been observed, scientists concluded that neutrinos were massless, which was assumed in the Standard Model.

The Standard Model includes all the known constituents of matter, six leptons and six quarks. These quarks and leptons are grouped into three generations. The lightest generation includes up and down quarks, which make up protons and neutrons, and the electron and electron neutrino. The two heavier generations of quarks are charm and strange, and top and bottom. The heavier generations of leptons are the muon and tau and the corresponding neutrinos, the muon and tau neutrinos. These quarks and leptons are all fermions. A fermion is a particle with odd half-integer spin while a boson is a particle with integer spin, such as the photon and Higgs boson as discussed below.

The Standard Model also includes the force carriers between the fundamental particles, such as photons carrying the electromagnetic force; gluons mediating the strong force; and Z and W bosons mediating the weak force. The Higgs boson is assumed to have zero spin and to manifest itself everywhere, even in vacuum. When an elementary particle collides with a Higgs boson, the particle acquires mass and changes handedness. If a left-handed neutrino interacted with Higgs bosons, it would acquire mass and change to right-handed. Since no right-handed neutrino is observed, the Standard Model states that the neutrinos are massless.

As described above, in the Standard Model, neutrinos have three flavors: electron neutrino, muon neutrino and tau neutrino. They are very abundant particles in

the universe, but they cannot be easily detected because they interact only through the weak interaction. It was long thought that neutrinos were massless. However, many neutrino experiments, such as Homestake, Super-K, SNO, and KamLAND, have demonstrated that neutrinos mix, and therefore must have nonzero masses.

In the 1960s, Ray Davis's Homestake experiment found that the observed solar neutrino rate was only one-third of the predicted rate [3]. This result was known as the solar neutrino problem. To explain the discrepancy between the observed and predicted rates of solar neutrinos, neutrino masses and mixing were introduced. The Homestake experiment was designed to detect only electron neutrinos. If neutrinos have mass, they may be observed in a different flavor from what they were produced as. The discrepancy between the measured and predicted neutrino rates may then be explained by the transformation in flight of the electron neutrinos into other flavors. This phenomenon is known as neutrino oscillation.

The Super-Kamiokande experiment (Super-K) is a neutrino experiment in Japan. The Super-K Collaboration announced the first evidence of atmospheric muon neutrino disappearance in 1998 [4]. It provided strong experimental evidence supporting the theory of neutrino mixing and nonzero masses.

The Sudbury Neutrino Observatory (SNO) is a neutrino observatory sited 2100 m underground in a mine in Canada to study solar neutrinos. The SNO detector was a large tank of heavy water. Before the SNO experiment, solar neutrino detectors had been designed to be sensitive primarily to electron neutrinos. The SNO detector was able to observe the charged current interactions of solar ν_e and also the neutral current interactions of all three neutrino types. Charged (neutral) current interaction are those in which neutrinos interact with matter by exchanging W bosons (a Z boson). SNO thus measured the total flux of solar neutrinos on the Earth. The total measured flux, including all neutrino types, was consistent with the

predicted flux of ν_e emitted by the Sun. Therefore, SNO's results demonstrated that the solar neutrinos changed flavors. In 2001, the first scientific results of SNO [5] were published, bringing the first clear evidence that solar neutrinos oscillate. SNO's results supported the nonzero neutrino masses and mixing models. Since then, neutrino experiments have focused on confirming neutrino oscillations and improving the precision of oscillation parameter measurements. In 2002, the Kamioka Liquid-scintillator Anti-Neutrino Detector Experiment (KamLAND) found the first evidence of electron antineutrino disappearance, using nuclear reactors in Japan [6]. In 2008, the KamLAND collaboration published precise results combining their data with the SNO data assuming a two-neutrino framework [7].

There have been many other experiments studying the behavior of neutrinos, such as the Double Chooz, Daya Bay and RENO reactor neutrino experiments. Also, the accelerator-based Main Injector Neutrino Oscillation Search (MINOS) and KEK to Kamioka (K2K) experiments provided the first precise measurements of muon neutrino disappearance. After decades of effort, neutrino oscillation has been broadly accepted as an explanation for neutrino flavor transformations. The mechanism of neutrino oscillation is discussed next.

The neutrinos are created through weak interactions in their flavor eigenstates, which are superpositions of the mass eigenstates. The mass eigenstates propagate as plane waves (in natural units $c = 1, \hbar = 1$): $|\nu_i(t)\rangle = e^{-i(E_i t - \vec{p}_i \cdot \vec{x})} |\nu_i(0)\rangle$, where t is the time of travel from the starting point, E_i is the energy of the mass eigenstate i, x_i is the position of the neutrino and $\vec{p}_i$ is its three momentum. Since the neutrino has a tiny mass, it travels relatively fast, close to the speed of light. With $m_i \ll |\vec{p}|$, the neutrino energy can be approximated as $E_i = \sqrt{p_i^2 + m_i^2} \simeq p + \frac{m_i^2}{2p}$. Here, we assume the neutrino is produced with a momentum p, which is the same for all its mass eigenstates. The distance of travel, L, is used instead of the time, t. Then,

the wave function can be rewritten as $|\nu_i(L)\rangle = e^{-i\frac{m_i^2 L}{2E}} |\nu_i(0)\rangle$, where $E \approx p$ is the average energy of all the mass eigenstates. There are three mass eigenstates and they propagate with different frequencies. The heavier the mass term m_i is, the faster the mass eigenstate oscillates. As the superposition of the mass eigenstates, the flavor eigenstate is then affected by the mass eigenstates. Thus, a neutrino initially created as a muon neutrino might be observed as an electron neutrino after some distance of travel. This is what we call neutrino oscillation.

The eigenstates of neutrino flavor are related to the eigenstates of neutrino mass by a unitary matrix, the Pontecorvo–Maki–Nakagawa–Sakata (PMNS) matrix (U^{PMNS}):

$$\begin{bmatrix} \nu_e \\ \nu_\mu \\ \nu_\tau \end{bmatrix} = U^{\mathrm{PMNS}} \begin{bmatrix} \nu_1 \\ \nu_2 \\ \nu_3 \end{bmatrix} \tag{1.1}$$

$$= \begin{bmatrix} c_{12}c_{13} & s_{12}s_{13} & s_{13}e^{-i\delta_{CP}} \\ -s_{12}c_{23} - c_{12}s_{23}s_{13}e^{i\delta_{CP}} & c_{12}c_{23} - s_{12}s_{23}s_{13}e^{i\delta_{CP}} & s_{23}c_{13} \\ s_{12}s_{23} - c_{12}c_{23}s_{13}e^{i\delta_{CP}} & -c_{12}s_{23} - s_{12}c_{23}s_{13}e^{i\delta_{CP}} & c_{23}c_{13} \end{bmatrix} \begin{bmatrix} \nu_1 \\ \nu_2 \\ \nu_3 \end{bmatrix}, \tag{1.2}$$

where c_{ij} stands for $\cos\theta_{ij}$, s_{ij} means $\sin\theta_{ij}$, and θ_{ij} is the mixing angle between mass eigenstates i and j $(i, j = 1, 2, 3)$. The vector on the left side represents the neutrino flavor eigenstates and the vector on the right side represents the neutrino mass eigenstates. There are three neutrino mixing angles $(\theta_{12}, \theta_{13}, \theta_{23})$ and one phase (δ_{CP}) in the PMNS matrix.

Using the elements of the PMNS matrix, the probability of observing the

change of neutrino flavors is described as:

$$
\begin{aligned}
P_{\alpha\to\beta} = |\langle \nu_\beta(L)|\, \nu_\alpha\rangle|^2 &= \left|\sum_j U^*_{\alpha j} U_{\beta j} e^{-i\frac{m_j^2 L}{2E}}\right|^2 \\
&= \delta_{\alpha\beta} - 4\sum_{i>j} \mathrm{Re}\left(U^*_{\alpha i} U_{\beta i} U_{\alpha j} U^*_{\beta j}\right) \sin^2\left(\frac{\Delta m^2_{ij} L}{4E}\right) \\
&+ 2\sum_{i>j} \mathrm{Im}\left(U^*_{\alpha i} U_{\beta i} U_{\alpha j} U^*_{\beta j}\right) \sin\left(\frac{\Delta m^2_{ij} L}{2E}\right),
\end{aligned}
\tag{1.3}
$$

where $\Delta m^2_{ij} \equiv m^2_i - m^2_j$ is the squared-mass difference. θ_{12} and Δm^2_{21} are measured by solar neutrino experiments such as SNO, using the neutrino flux produced by the Sun, and also by KamLAND, using electron antineutrinos from nuclear reactors. θ_{23} and Δm^2_{32} are measured by the experiments studying atmospheric neutrinos, such as the Super-K experiment. Short-baseline reactor experiments, such as the Daya Bay experiment, measure θ_{13} and Δm^2_{31} with electron antineutrinos from reactors. There is also another type of experiment, which uses ν_μ and $\bar{\nu}_\mu$ from a particle accelerator beam. The experiments of this type aim to measure values of the θ_{23}, Δm^2_{32} and δ_{CP} parameters—for example, the NOvA and Tokai to Kamioka (T2K) experiments.

My thesis is focused on measurements of neutrino oscillation parameters with the NOvA experiment.

CHAPTER 2

THE NOVA EXPERIMENT

NOvA is a long-baseline neutrino oscillation experiment with two functionally identical detectors. The energy spectrum of the neutrinos is measured by the near detector (ND) located 1 km from the NuMI target. The neutrinos are subsequently detected 810 km away in the far detector (FD) near Ash River, MN. Both detectors are located off the central beam-axis by 14 milliradians to get a narrow neutrino energy spectrum with an energy peak around 1.8 GeV, which is optimized to measure the electron neutrino appearance channel [8]. Figure 2.1 shows the locations of the NOvA detectors on Google Maps.

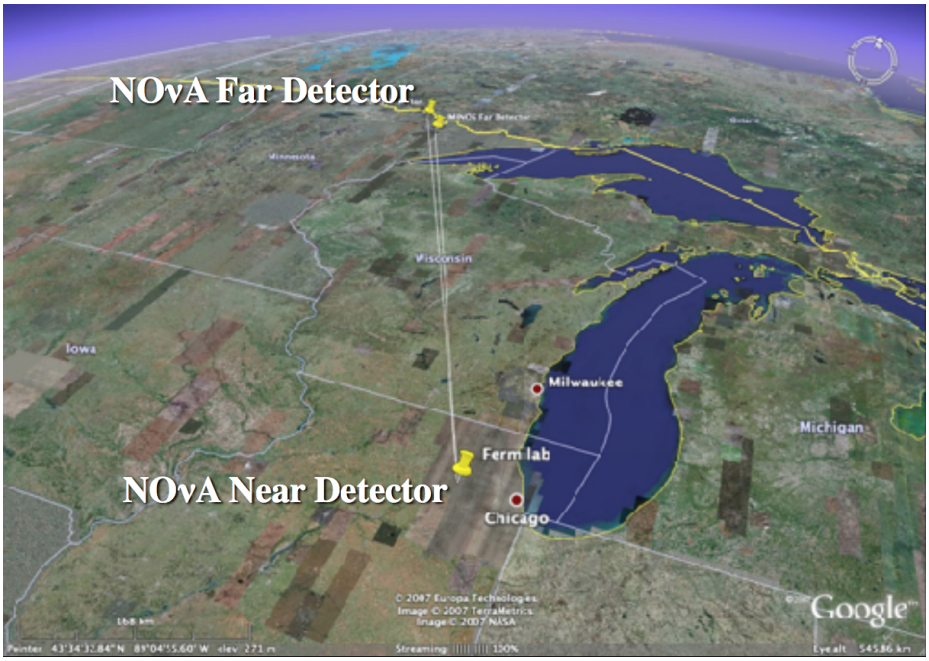

Figure 2.1. Locations of detectors

NOvA employs the Neutrinos at the Main Injector (NuMI) beam at Fermi National Accelerator Laboratory. As shown in Figure 2.2, the NuMI beam facility produces neutrinos and antineutrinos by steering a 120 GeV proton beam onto a

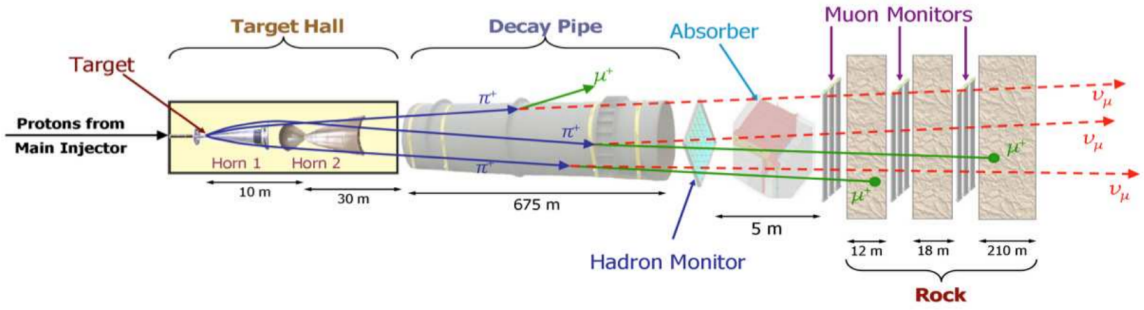

Figure 2.2. Neutrinos at NuMI neutrino beamline

narrow graphite target approximately 1 m in length. The produced hadrons are then focused by the two magnetic horns. As shown in Figure 2.3, forward horn current (FHC) mode provides mostly neutrino flux, and reversed horn current (RHC) mode provides mostly antineutrino flux. In both modes, most of the hadrons coming out from the target subsequently decay into (anti)neutrinos, among other particles, in a long decay pipe.

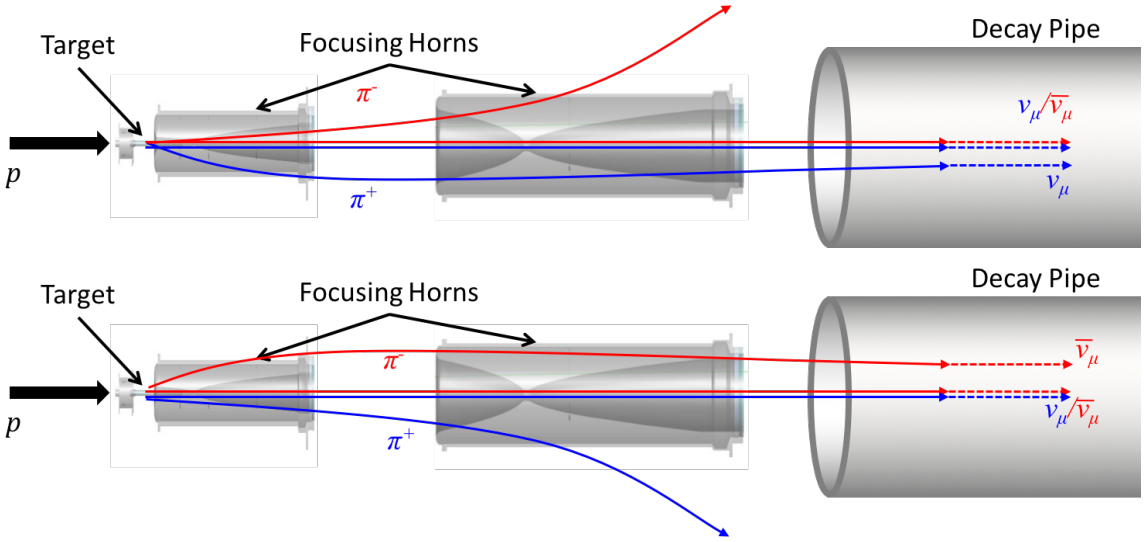

Figure 2.3. Forward (reversed) horn-current mode shown at the top (bottom) providing (anti)neutrino flux

Three major contributions to the neutrino beam originate from the following decays:

$$\pi^+ \rightarrow \nu_\mu + \mu^+; \tag{2.1}$$

$$\mu^+ \rightarrow \bar{\nu}_\mu + \nu_e + e^+; \tag{2.2}$$

$$K^+ \rightarrow \nu_\mu + \mu^+. \tag{2.3}$$

In the FHC mode, most of the muon neutrinos with the desired energy at the ND are results of π^+ decay. There are also a big fraction of the muon neutrinos with higher energy from the decay of K^+. There are also some other hadron products coming off the target such as π^-, K^- and K^0_L. These hadrons contribute the majority of background in the oscillation analysis. The focusing horns aim to focus most of the π^- flux while the remaining flux components are not well focused, or unfocused.

A similar story takes place in the RHC mode with the sign of the charge flipping everywhere. Three major contributions originate from:

$$\pi^- \rightarrow \bar{\nu}_\mu + \mu^-; \tag{2.4}$$

$$\mu^- \rightarrow \nu_\mu + \bar{\nu}_e + e^-; \tag{2.5}$$

$$K^- \rightarrow \bar{\nu}_\mu + \mu^-. \tag{2.6}$$

The contributions of different hadron products are shown in Figure 2.4 [9] for both neutrino and antineutrino beams. The ND is positioned to maximize the similarity between the neutrino energy spectra observed at the two detectors. This helps reduce some types of systematic uncertainties in the oscillation analysis. The data collected at the ND are also being used to make precise measurements of various neutrino cross sections.

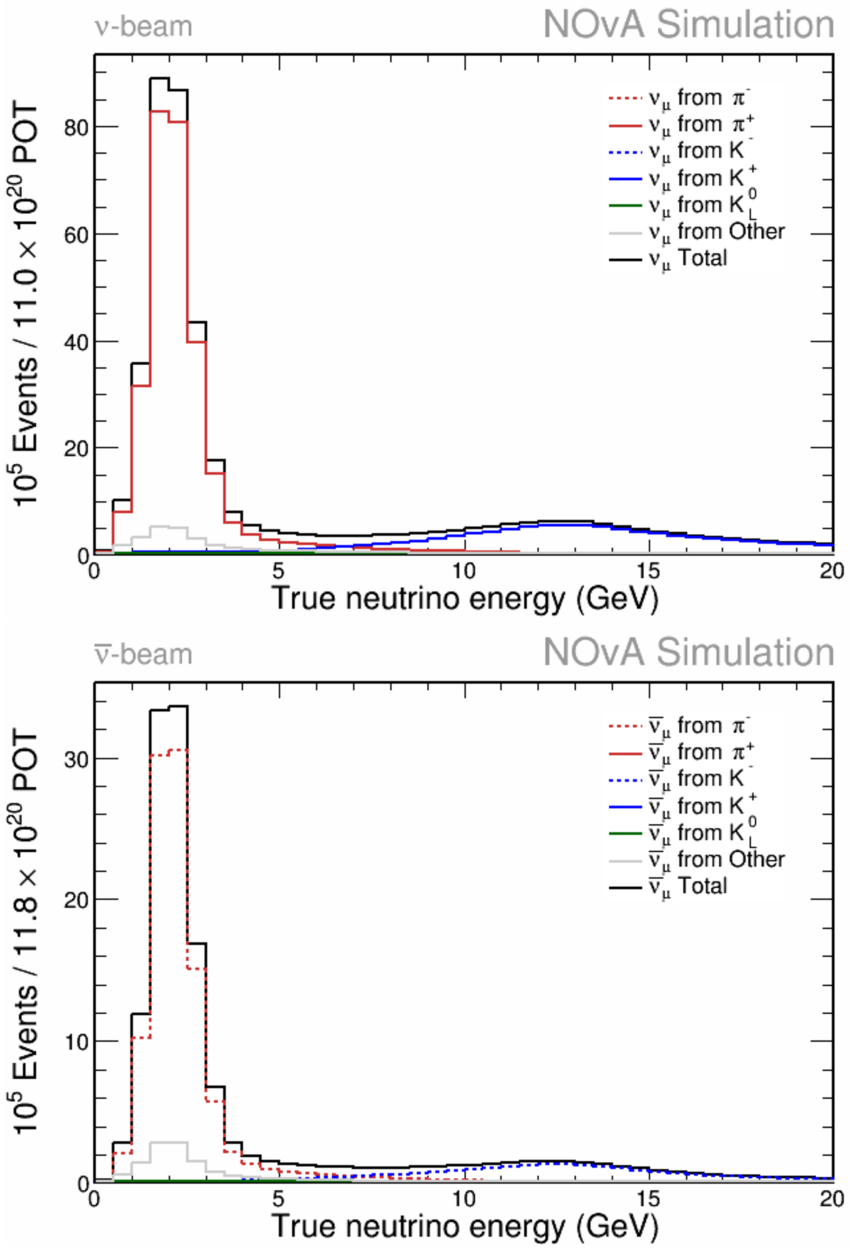

Figure 2.4. Flux compositions of ν_μ (top) and $\bar{\nu}_\mu$ (bottom) charged current interactions at ND

The NOvA detectors use liquid scintillator tracking so that they can image final-state electrons in ν_e charged current interactions. The detectors are finely segmented and use low-Z materials, which have a low atomic number (Z) of protons in the nucleus. The NOvA detectors are made of alternating layers, as shown in

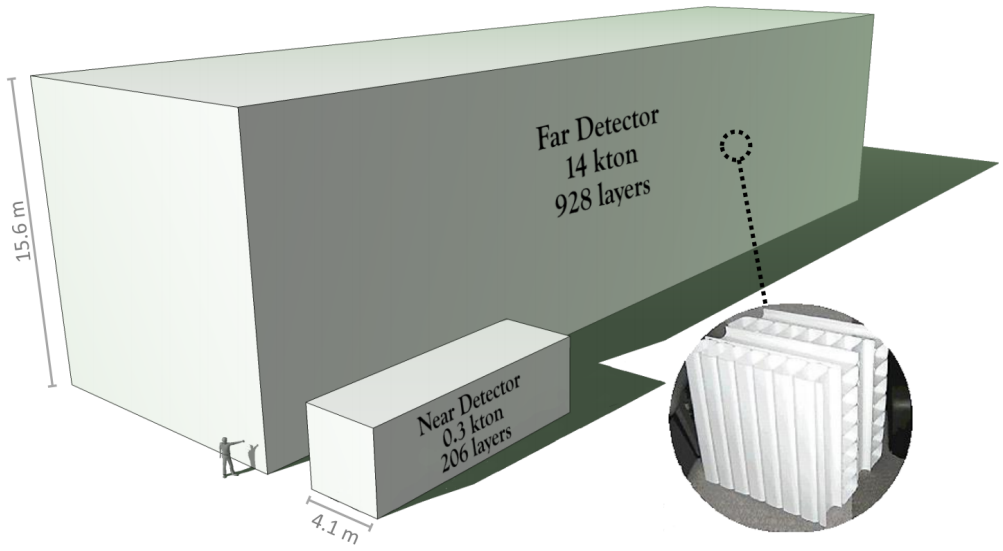

Figure 2.5. Cartoon of NOvA detectors with a human figure shown for scale and view of PVC structure

Figure 2.5 [10]. Each layer is constructed from aligned polyvinyl chloride (PVC) cells with cross sectional size 6 cm by 3.87 cm. One layer of horizontal PVC cells is followed by one layer of vertical PVC cells. The ND and the FD are different in both numbers and lengths of cells. The FD has 928 layers, each of which has 384 cells, while the ND has 206 layers, each with 96 cells. The length of the cells is the same as the detector's width and height, which is 15.6 m in the FD and 4.1 m in the ND. The FD is 59.8 m in length and the ND is 12.67 m in length. At the downstream end of the ND (not shown in the figure), a 2.9 m tall by 4.1 m wide by 3.23 m long muon range stack (muon-catcher) is used to stop and measure outgoing muons generated by neutrino interactions. The muon-catcher is made of standard detector layers interleaved with 4-inch steel plates. The FD is on the surface of the Earth, which receives a very high rate of cosmic rays. The ND is approximately 100 m underground, receiving a negligible rate of cosmic rays during the beam spills.

Each detector cell contains a wavelength-shifting (WLS) fiber which is twice the length of the cell and looped at the end of the cell. Both ends of the fiber are connected to one pixel of the 32-pixel avalanche photodiode (APD) photodetectors. The APD can read out light signals from 32 cells at the same time from its 32 individual pixels and convert them into electrical signals. The 32 cells connecting to the same APD are called one module of the detectors.

The APD is connected to a front-end board (FEB). The FEB has some custom chips to handle the electrical signals from the APDs. For example, the electrical signals are shaped into pulses by an application-specific integrated circuit. Then, an analog-to-digital converter (ADC) is used to convert the shaped analog signals to digital signals. There are also some other chips to suppress the zero readouts or to filter the noise. The FEB also discriminates the electrical signals by giving them time stamps and then sends them to a data concentrator module (DCM), which is a custom built single board computer. Each DCM collects the data streaming from 64 FEBs in a localized region of the detector and sorts the data by the time stamps into 50 μs timing intervals (microslices). Then an event-building algorithm is executed to further pack the microslices into a larger 5 ms "millislice." Once the data streams are packed, the data packets from a specific timing window are transmitted to a computing cluster, called the farm of buffer nodes, which is located at the FD site [11]. The FD is used as an example to illustrate how the components described above work, as shown in Figure 2.6.

When a neutrino strikes an atom in the detector, it releases a burst of charged particles. Scintillation light is produced when charged particles traverse the liquid scintillator and the light bounces in the cell until it is captured by the WLS fiber or absorbed by the scintillator or PVC. As these charged particles slow down in the detector, their energy is estimated from the amount of scintillation light collected

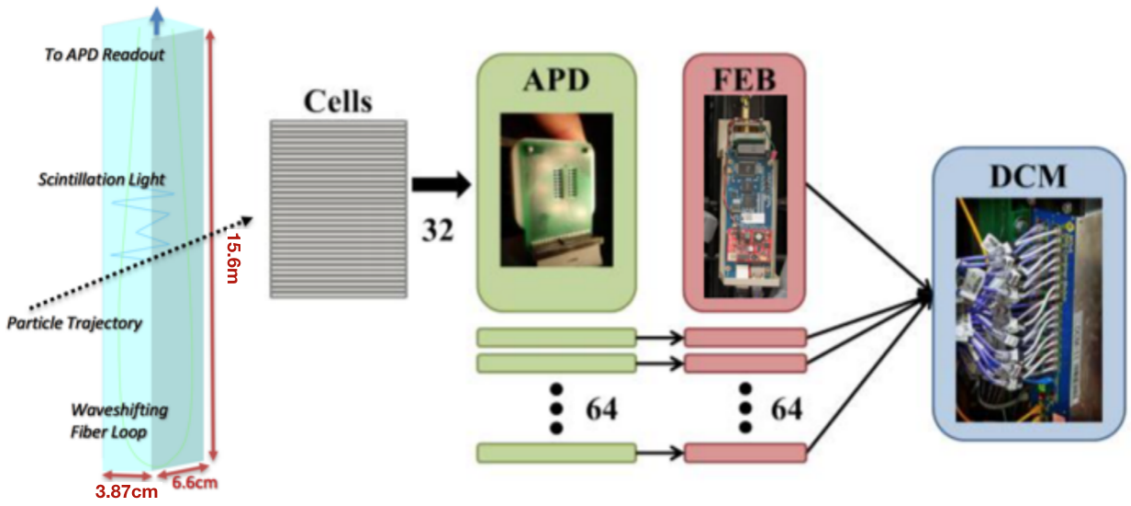

Figure 2.6. Signal-processing chain of NOvA FD

using WLS fiber and read out by APDs. Using the pattern of light seen by the APDs, we can determine what kind of neutrino caused the interaction and approximately what its energy was.

CHAPTER 3

NOVA LIGHT MODEL

NOvA uses a blended scintillator of which 95.8% by mass is mineral oil and 4.1% is primary scintillant (pseudocumene). The primary scintillant is excited by incident charged particles and then decays by emitting photons in the 270–320 nm wavelength range. These short-wavelength photons excite the main wavelength shifters (PPO and MSB), which de-excite by emitting photons of longer wavelengths. PPO de-excites by emitting photons in the 340–380 nm range, with a tail extending to 460 nm. MSB shifts the photons' wavelengths through the same mechanism to 390–440 nm, with a tail extending to 480 nm. Therefore, most of the photons' wavelengths fall into a range that the WLS fiber can capture, which is 400–450 nm. The wavelength shifters in the WLS fiber further shift the captured photons into the range 490–550 nm, which is the preferred wavelength range for APDs to convert into photoelectrons. The efficiency of the APDs for converting incident photons to photoelectron signals is 85% when the photons have wavelengths within 500–550 nm [8].

The NOvA detector simulation employs a specially designed optical model to describe the light transport outlined above, including photon absorption and emission, and APD conversion. The scintillation light produced by charged particles shows characteristics that depend on the incident particle type, the energy of the particle and the properties of the scintillator. Two major effects in the NOvA detector light simulation are molecular scintillation light production, with its quenching effect, and Cherenkov light production. These light components are tuned in Monte Carlo (MC) simulation with the use of cosmic muon data and ND data coming from the NuMI beam.

The light model has a significant impact on the subsequent calibration and reconstruction. An accurate light model is a prerequisite for precise charged parti-

cle energy estimation in the detector. Particle energy is needed for accurate event reconstruction and classification, and is also critical to extraction of neutrino oscillation parameters. The tune of the light model has been one of the larger systematic uncertainties in the NOvA oscillation analysis.

3.1 Scintillation and Cherenkov Models

NOvA employs Birks' law to describe the scintillator light yield. The fluorescence intensity of a given substance is described by the light yield per path length,

$$\frac{dS}{dr} = \frac{A\frac{dE}{dr}}{1 + k_B\frac{dE}{dr}}, \tag{3.1}$$

where S represents the scintillation response; r represents residual track length (the distance from the current position to the end of the particle trajectory); A is the scintillator efficiency; k_B is the Birks' constant, which depends on the scintillator composition and density; and $\frac{dE}{dr}$ is the energy loss rate. For small values of $\frac{dE}{dr}$, Birks' law is close to linear. For example, the typical $\frac{dE}{dr}$ value for muon tracks in the NOvA detectors is approximately 2 MeV/cm. When $\frac{dE}{dr}$ gets larger, Birks' law quickly becomes nonlinear and the light yield saturates. The Birks' constant for the NOvA scintillator is $k_B = (1.155 \pm 0.065) \times 10^{-2}$ g/(MeV cm^2), which has most recently been evaluated by the NOvA collaboration [12].

Cherenkov light is emitted when a charged particle passes through the scintillator at a speed greater than the speed of light in the medium. The NOvA light model includes scintillation light, which is described by the Birks' law (Equation 3.1), and Cherenkov photon production. When the light model is applied in the MC simulation, it is expected that the MC simulation accurately describes the data. The proportions of photons contributed by the Birks' model and Cherenkov photon production are adjusted so that the total number of photons (N_γ) in the MC simulation

matches that observed in data, as

$$N_\gamma = F_{\text{view}}(Y_s E_{\text{Birks}} + \epsilon_C C_\gamma)\,, \tag{3.2}$$

where Y_s is the scintillator brightness per unit energy deposition, also known as scintillation light yield; E_{Birks} represents the energy deposition simulated by the Birks' model; ϵ_C is the scintillator efficiency for Cherenkov photons; C_γ is the number of Cherenkov photons produced by the charged particle in MC simulation; and F_{view} represents four normalization factors, corresponding to the xz and yz views of the two detectors. The normalization factors absorb the differences among detector views in the light model tuning so that photon production in both detectors shares the same set of physics constants described above.

In the ND, the ratio of Cherenkov and scintillation photons is approximately 1:20 for muon tracks produced by ν_μ charged-current quasi-elastic (CCQE) interactions. Approximately 5% (0.5%) of photons produced by a muon (proton) from a ν_μ CC interaction are Cherenkov photons. Since muon and proton tracks have different behaviors in producing Cherenkov photons, they both are used for tuning the Cherenkov photon proportion in the NOvA light model. Cosmic ray events at both detectors are also used in the light model tuning. A least-squares fit[1] between the selected data and MC samples is performed to extract the light model parameters F_{view}, Y_s, and ϵ_C.

3.2 MC Simulations

To extract parameters of the light model, four different sets of data and MC samples are used. These are: ND cosmic rays (ND CRY); FD cosmic rays (FD CRY); and ND muon and proton tracks from ν_μ CCQE-like interactions provided by the

[1]Fit is performed by using a data analysis framework called ROOT [13].

NuMI beam flux.

To generate the MC samples, the NOvA-ART framework is used.[2] For the cosmic simulation, a Cosmic-Ray Shower Library [14] is used to produce cosmic rays at sea level. All simulated cosmic rays are input to the Geometry and Tracking Software [15] (Geant4), which is used to describe the detector geometry and to simulate the physics processes inside the detectors. A NOvA-ART module, called *photon transport*, is applied after Geant4, which parameterizes a template to convert the deposited energy to scintillation light. It manages photon transport in the detectors starting from the light emitted by the scintillator all the way to the APD response. With this template, we can adjust the proportions of scintillation light and Cherenkov photons by tuning the light model. Running *photon transport* is also faster than running Geant4 for each detector cell to simulate all the photons produced and captured. Another NOvA-ART module, called *daq*, is used to simulate the electronic readout. The NuMI beam simulation for the NOvA detectors is done using *g4numi*, which is a Geant4-based simulation tool with a detailed description of the NuMI beamline geometry and fields. It simulates particle interaction and propagation in the NuMI target and beamline [16].

For ND cosmic samples, 3000 files were simulated, each containing 22,000 events. FD cosmic samples consist of 1000 files, each comprising 200 simulated events. There are 3000 ND NuMI beam MC files, with 22,000 events in each. Since the FD is on the surface and the ND is underground, the FD is more sensitive to cosmic rays. Additionally, the ND has a much smaller size than the FD does, so that the ND receives very few cosmic rays. Due to the above reasons, more cosmic events are simulated at the ND in the first place so that the selected ND cosmic samples

[2]Descriptions of the NOvA-ART framework and access to the code repository can be found at `https://cdcvs.fnal.gov/redmine/projects/novaart/wiki`.

have comparable sizes to the FD cosmic samples. All the MC files have time stamps matching to period 3 (12 October, 2015 – 2 May, 2016) of the NOvA run.

3.3 Selections

Every 1.3 seconds, the NuMI beam creates a spill of neutrinos. Each spill lasts for 10 μs, which is known as the beam spill window. Every time the protons from the NuMI beam strike the target, the trigger records a timestamp. The timestamp marks the start of a beam spill window. Both detectors are synchronized to the trigger, so that we know if the data are taken within beam spill windows. For the cosmic samples, a NOvA-ART cosmic filter, called *removebeam*, is applied to keep only cosmic events that are out of the beam spill widows. Besides the cosmic filter, some selections are applied to both detectors to get data and MC samples for the light model tuning.

The cosmic selection is based on detector geometry which is different between the ND and FD. However, the rules for selecting qualified particle tracks are similar. All cosmic tracks start outside the detector. We require them to end inside the detector. The distance of any ending points to all the walls of the detectors should be at least 50 cm. In addition, for the ND, any events involving the muon-catcher are not used.

The beam selections are applied to the ND data and MC files for collecting muon and proton tracks from muon neutrino interactions. The ν_μ CCQE-like interactions in the ND are selected. Then, the high-quality muon and proton tracks are picked out from the selected ν_μ CCQE-like interactions. The details of the selections are as follows:

1. Containment selections are applied to make sure the events and tracks are fully contained within the ND detector. The distance of the starting or ending point

of any track to the ND front, back, top, and side walls is no less than 50 cm;

2. Events in the muon-catcher are not used;

3. All ND DCMs were working during the time of data-taking;

4. Track quality selections are based on the topology and energy of ν_μ interactions:

   (a) Any selected ν_μ interaction event satisfies the following requirements: event has at least 8 hits; any hits of the event is at least 1 cell away from any ND walls; event was taken within NuMI beam spill window;

   (b) Besides the above, some selections are applied to the substructure of the ν_μ interaction to ensure track quality: the event must contain two 3D outgoing particle tracks; each track has energy deposited in at least 4 cells; two outgoing tracks start within a distance of 0 cm $< |\Delta x|, |\Delta y| <$ 12 cm and 0 cm $< |\Delta z| <$ 20 cm, where $|\Delta x|$, $|\Delta y|$, and $|\Delta z|$ are the absolute differences of the coordinates of the two track starting points; the longer track is at least 300 cm in length;

   (c) The longer (shorter) track in event is a muon (proton) track candidate.

3.4 Sample Validations

After applying the various selections to both data and MC files separately, data and MC comparison is performed to make sure that the selections behave consistently between data and MC. This procedure is called sample validation. The distributions of residual track length (see Figure 3.1) and path length (see Figure 3.2), which is the position of the hit along the track, are compared between data and MC samples for the sample validation. There is an overall good data and MC agreement after applying the selections at the ND. Hence, these samples are validated to be used for extracting the light model parameters.

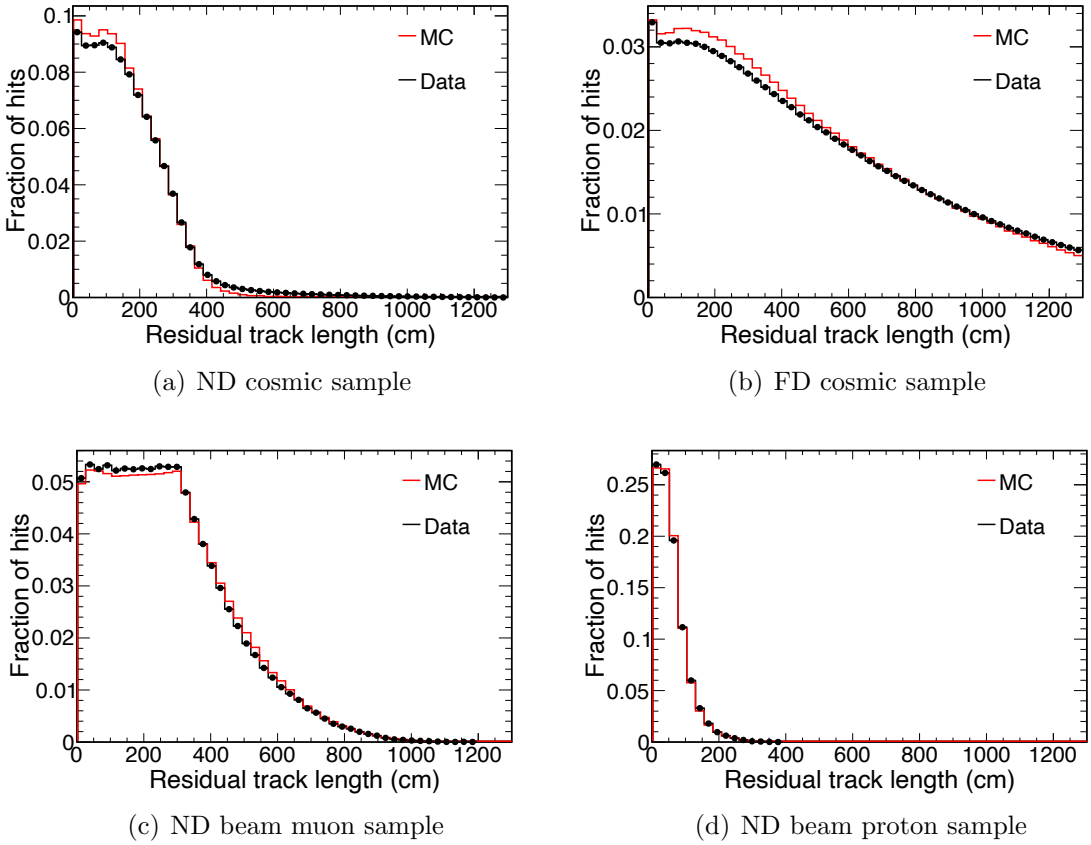

(a) ND cosmic sample

(b) FD cosmic sample

(c) ND beam muon sample

(d) ND beam proton sample

Figure 3.1. Data and MC comparison of residual track length

In NOvA, the detector light model is tuned first, followed by the detector energy calibration. Figure 3.3 shows the distribution of pre-calibrated energy (PE) of hits, which is the energy before the detector calibration techniques are applied. The samples that are used for the current light model tuning are calibrated using the old light model and calibration techniques from the previous analysis. The light model tuning is thus performed iteratively. Light model tuning adjusts the ratio of photons from scintillation and Cherenkov mechanisms, so that a better data and MC overall agreement on PE distributions is achieved after light model tuning.

Aside from data and MC comparison, MC validation is performed as well. The variables of interest are the MC information used in the tuning, i.e., the variables in Equation 3.2. With beam samples, particle identification (PID) and track quality

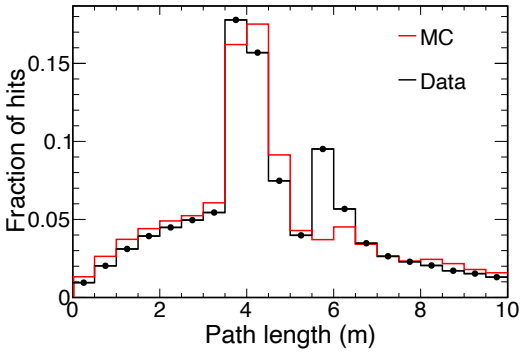

(a) ND cosmic sample

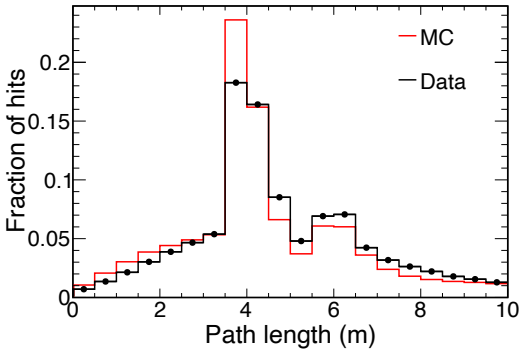

(b) FD cosmic sample

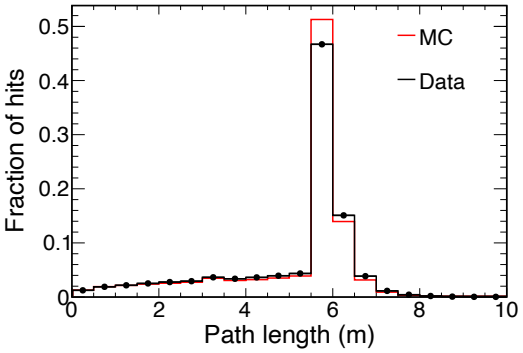

(c) ND beam muon sample

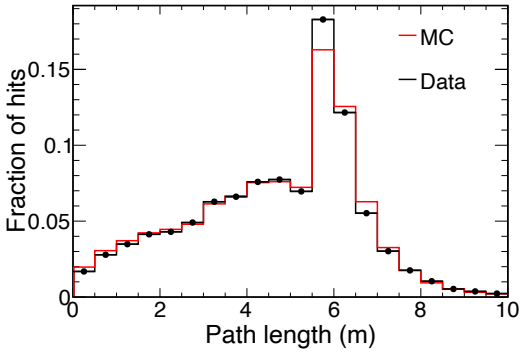

(d) ND beam proton sample

Figure 3.2. Data and MC comparison of path length

Table 3.1. Composition of Selected ND Beam MC Samples

	muon	proton	others
ND muon sample	0.9535	0.0252	0.0213
ND proton sample	0.0593	0.5472	0.3935

selections are applied to get greater purity in selecting muon and proton tracks. Ideally, the majority of the muon (proton) sample should consist of high-purity muon (proton) tracks. The MC composition of the muon and proton samples is shown in Figure 3.4 and Figure 3.5. The composition of beam muon and proton MC samples is summarized in Table 3.1. The muon track sample has a higher purity than the proton track sample. For each selected ND interaction, the longer track is used as the muon track candidate, and the shorter one is used as the proton track candidate. Since the

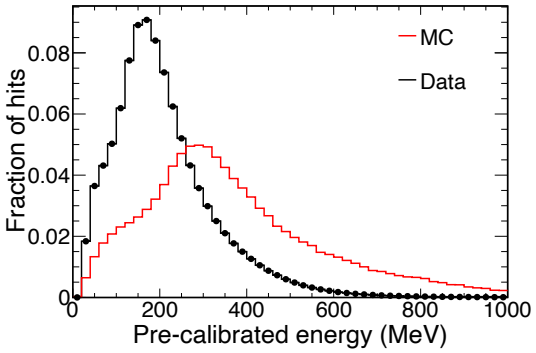

(a) ND cosmic sample

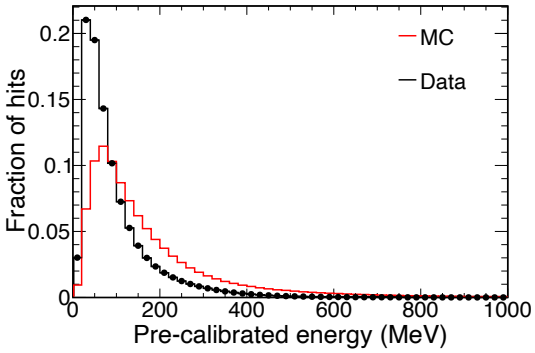

(b) FD cosmic sample

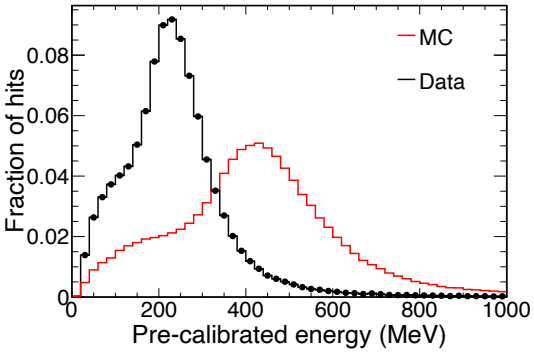

(c) ND beam muon sample

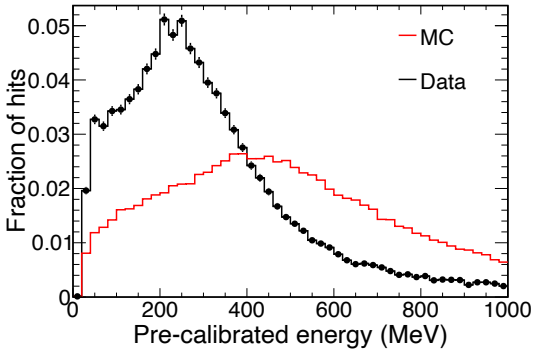

(d) ND beam proton sample

Figure 3.3. Data and MC comparison of pre-calibrated energy of hits

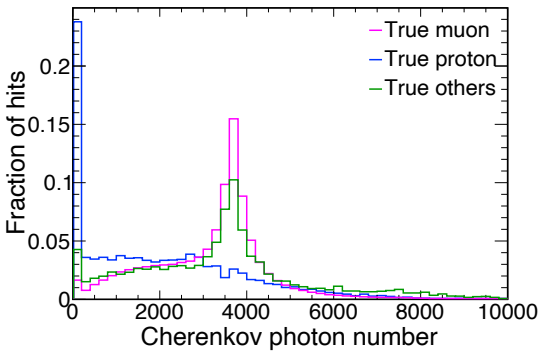

(a) ND muon Sample

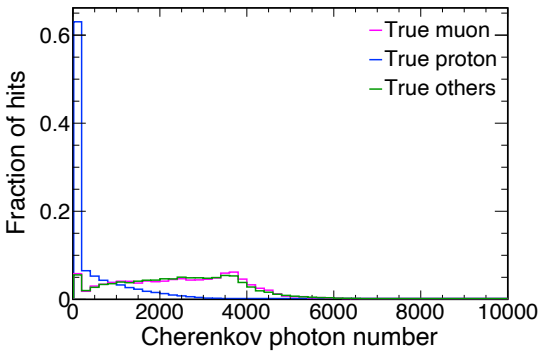

(b) ND proton Sample

Figure 3.4. MC composition of number of Cherenkov photons distributions for selected ND beam samples

primary outgoing muon in most ν_μ interactions is longer than the hadronic tracks, the beam selection performs well in selecting a high purity muon track sample. The

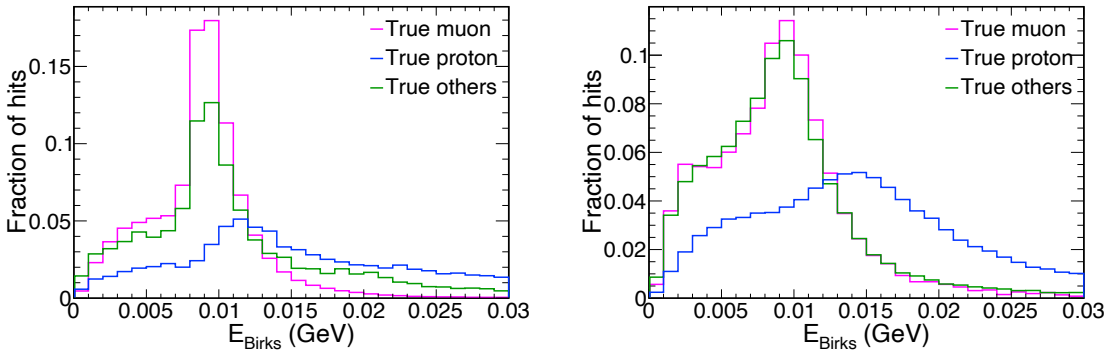

(a) ND muon sample

(b) ND proton sample

Figure 3.5. MC composition of Birks suppressed energy deposition distributions for selected ND beam samples

proton sample contains a big fraction of pions, which is a result of non-QE interactions. There are also some muon tracks mis-selected into the proton sample, which could be a result of two outgoing particles being similar in length. The beam selection could be improved in future by including particle identity selection to provide purer samples for light model tuning studies.

3.5 Fitting Technique

Two dimensional data and MC spectra are used for fitting. The energy deposition of a particle varies along its residual track length. Hence, residual track length is used as the x-axis and pre-calibrated energy per unit path length is used as the y-axis of the spectrum to make sure that the fit learns about the energy deposition variation along the residual track length. Since the distribution of residual track length rapidly falls for large values, the statistics of the hits in the spectra can be low for large values of residual track length. Therefore, we use wider bins for larger residual track length in order to have adequate statistics in each bin. Hence, all the 2D spectra of the MC and data samples that are used as input to the fit are binned with non-constant bin width.

As already mentioned, the NOvA detectors have alternating horizontal and vertical layers. The tuning naturally has the view factors F_{view} tuned separately by splitting the samples into xz view and yz view. The 2D spectra of data samples, as shown in Figure 3.6, are used in both rounds of fitting.

Before fitting MC to data samples, the number of hits in each residual track length bin is normalized to 1 for all the samples. A fit is then performed by minimizing the log-likelihood ratio of data over MC for all the normalized bins in all the samples. The contribution to the log-likelihood in each bin is defined as

$$L = -2N_{\text{data}} \log(N_{\text{MC}}) \,, \tag{3.3}$$

where N_{MC} represents normalized bin content of the MC sample, and N_{data} represents normalized bin content of the data sample. A normal log-likelihood ($\log N_{\text{data}} - \log N_{\text{MC}}$ may end up having tiny L in most bins. Defining the log-likelihood function in this way emphasizes the bin contents of the data samples and gives the fitter a larger log-likelihood value to minimize. Comparing the 2D spectra of MC samples before (Figure 3.7) and after (Figure 3.8) performing the fit to the data distributions (Figure 3.6), we can see that the MC distributions after fitting look more like the data distributions than before.

The light model parameters resulting from the first iteration of fitting are listed in Table 3.2. These new parameter values are incorporated into the corresponding MC simulation NOvA-ART module, i.e., *photon transport*. With the new simulation

Table 3.2. First Round Fitting Results

	$Y_s = 3317.0$ / MeV	$\epsilon_C = 0.471$
ND View Factor	$F_x = 0.55$	$F_y = 0.57$
FD View Factor	$F_x = 0.65$	$F_y = 0.56$

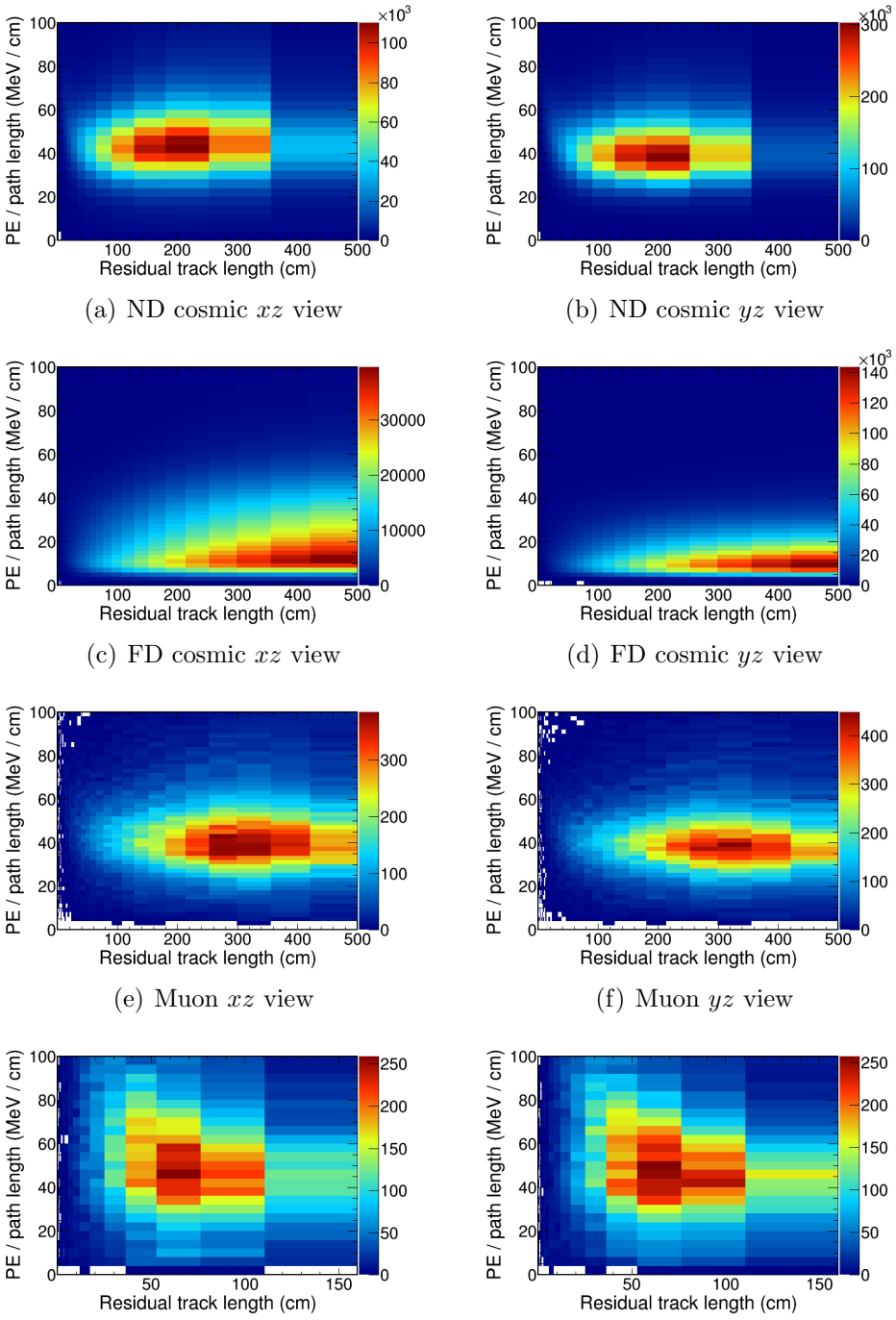

(a) ND cosmic xz view

(b) ND cosmic yz view

(c) FD cosmic xz view

(d) FD cosmic yz view

(e) Muon xz view

(f) Muon yz view

(g) Proton xz view

(h) Proton yz view

Figure 3.6. Spectra of selected data samples that are used as input to the fit in both rounds of light model tuning

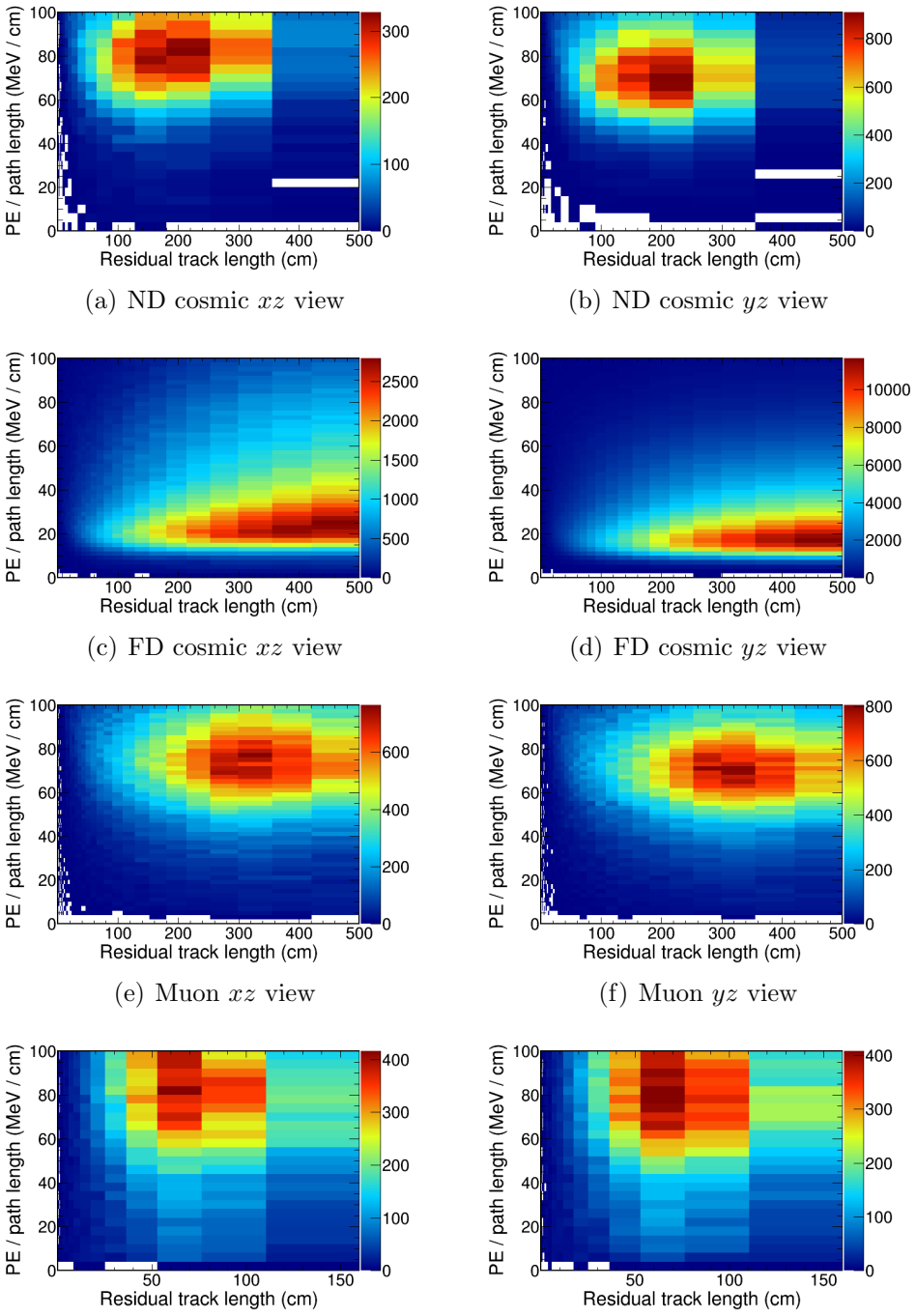

(a) ND cosmic xz view

(b) ND cosmic yz view

(c) FD cosmic xz view

(d) FD cosmic yz view

(e) Muon xz view

(f) Muon yz view

(g) Proton xz view

(h) Proton yz view

Figure 3.7. Spectra of selected MC samples that are used as input to the fit in the first round of light model tuning

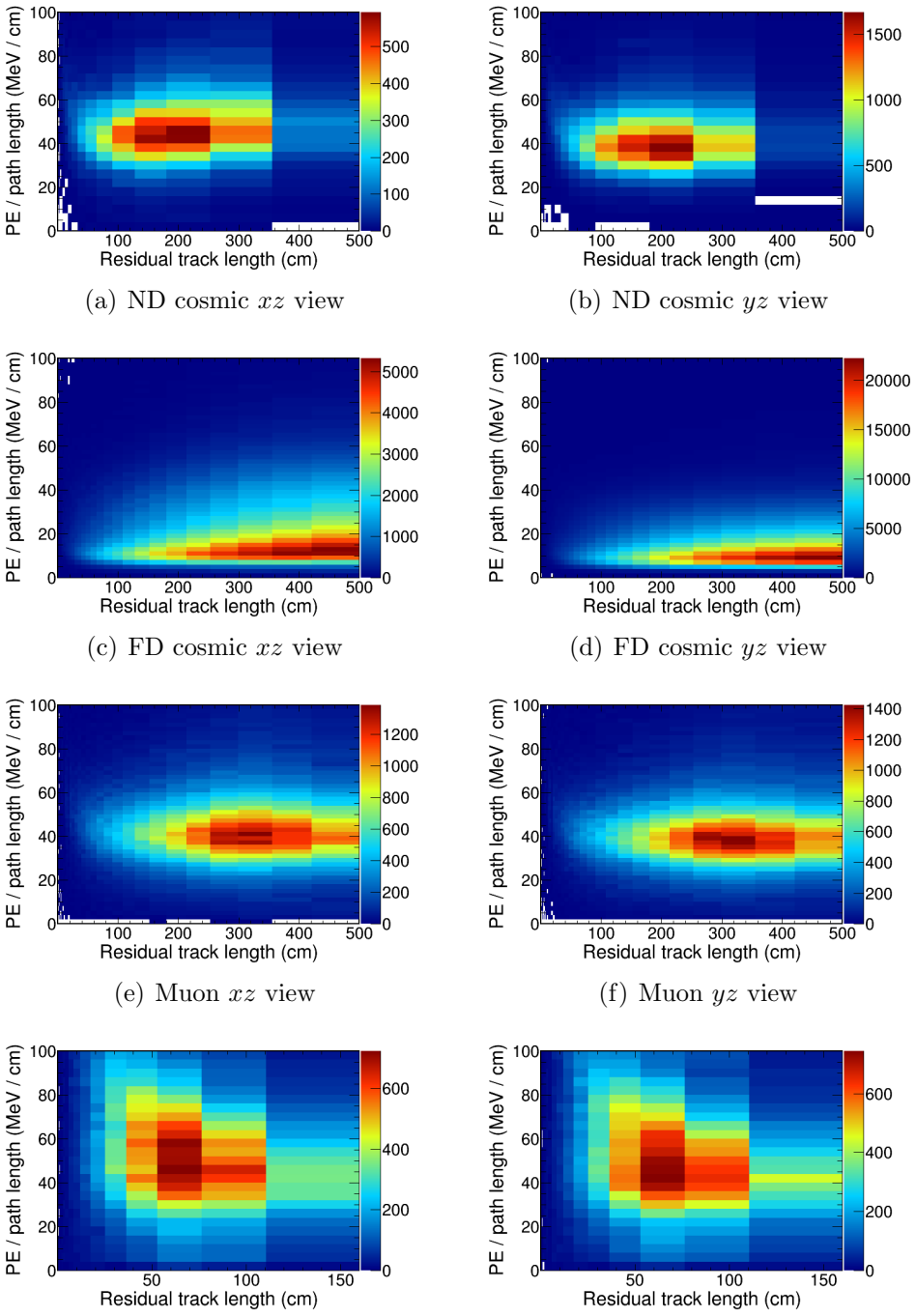

(a) ND cosmic xz view

(b) ND cosmic yz view

(c) FD cosmic xz view

(d) FD cosmic yz view

(e) Muon xz view

(f) Muon yz view

(g) Proton xz view

(h) Proton yz view

Figure 3.8. Spectra of selected MC samples after fitting in the first round of light model tuning

setup, based on the updated light model parameters, new MC samples are processed. An identical fitting procedure is then repeated with the new MC files, to confirm that the derived parameters from the first round of tuning have improved the MC and data agreement. The selected data samples used in the second round of tuning remain the same as have been used in the first round of tuning (see Figure 3.6). The spectra of the new MC samples after performing the fit are shown in Figure 3.9.

The MC samples are compared to the data samples in each round of tuning by looking at the projections on the y-axis, i.e., PE per unit path length. The data and MC distributions agree better with each other and become stable after the first round of tuning in both xz and yz views, as shown in Figure 3.10. The resulting parameters from the second round of fitting are used as the final light model parameters, as listed in Table 3.3.

Table 3.3. Second Round Fitting Results

	$Y_s = 3151.0$ / MeV	$\epsilon_C = 0.471$
ND view factors	$F_x = 0.58$	$F_y = 0.57$
FD view factors	$F_x = 0.53$	$F_y = 0.56$

3.6 Result and Systematic Studies

The light model parameters in Table 3.3 are applied to generate MC files for the NOvA oscillation analysis. Muon neutrino CCQE-like interactions are selected to provide muon and proton tracks for use in validating the new light model. Track quality is ensured by performing the following selections:

- Any event has exactly two reconstructed 3D Kalman tracks [17];
- Both tracks are contained in the detector volume;
- Both tracks have reconstructed muon ID [18] (ReMId) scores. A track is proton-

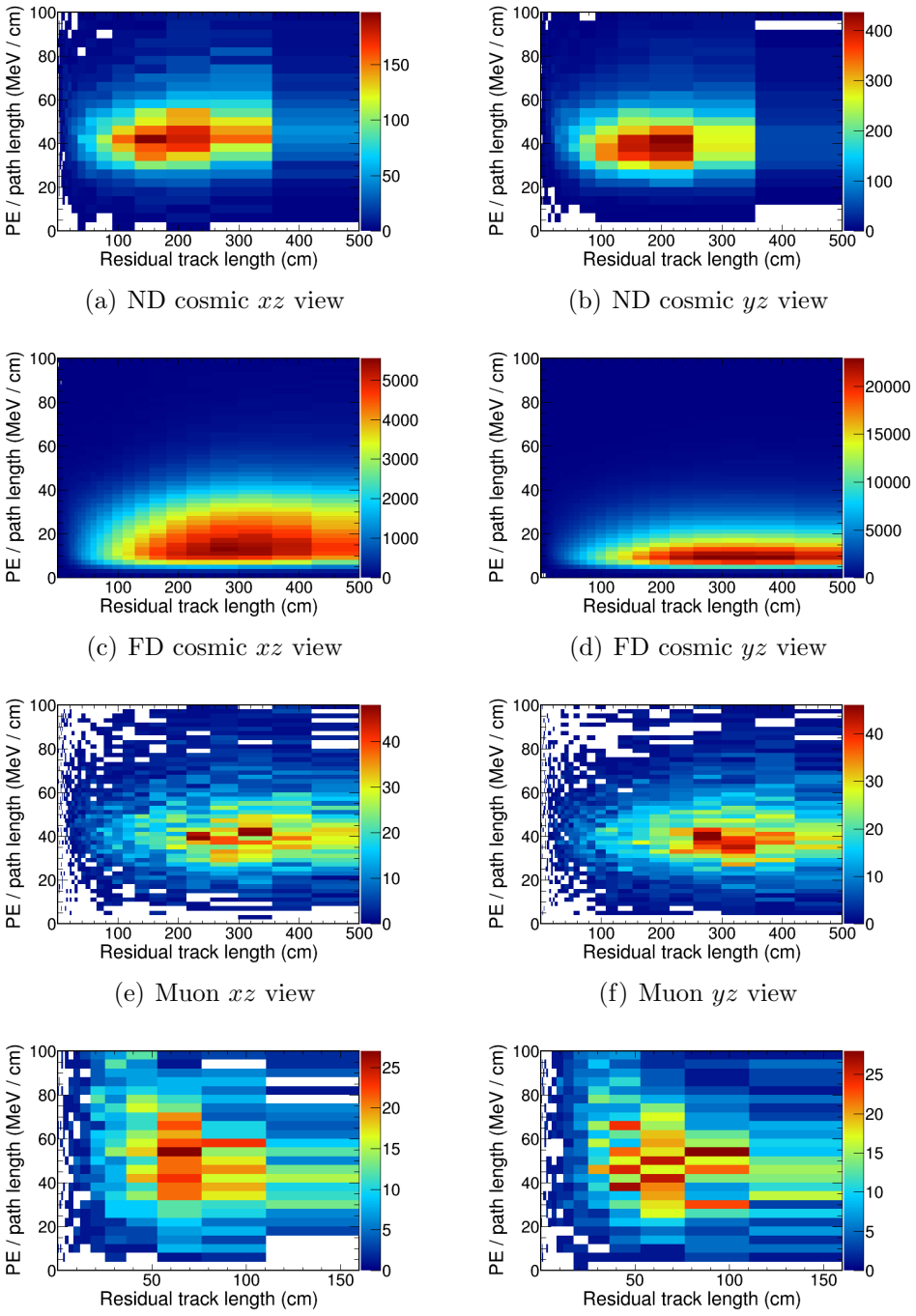

(a) ND cosmic xz view

(b) ND cosmic yz view

(c) FD cosmic xz view

(d) FD cosmic yz view

(e) Muon xz view

(f) Muon yz view

(g) Proton xz view

(h) Proton yz view

Figure 3.9. Spectra of selected new MC samples after fitting in the second round of light model tuning

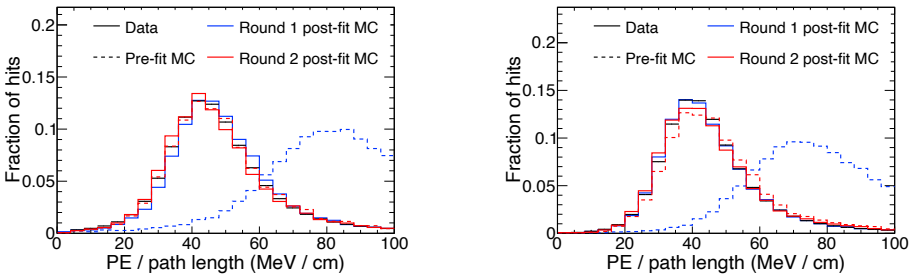

(a) ND cosmic xz view

(b) ND cosmic yz view

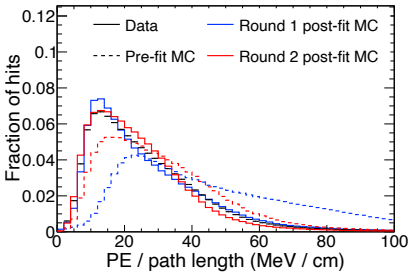

(c) FD cosmic xz view

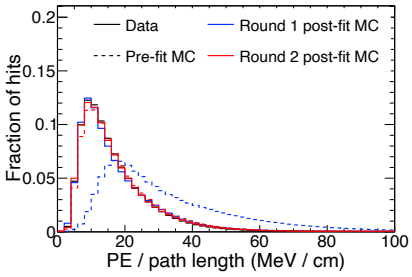

(d) FD cosmic yz view

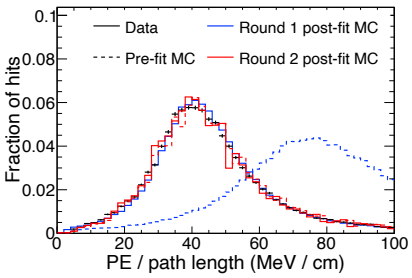

(e) Muon xz view

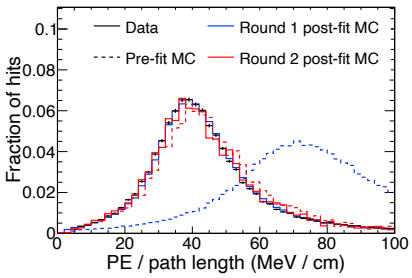

(f) Muon yz view

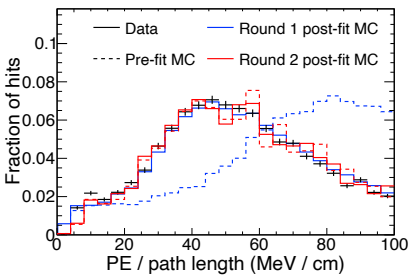

(g) Proton xz view

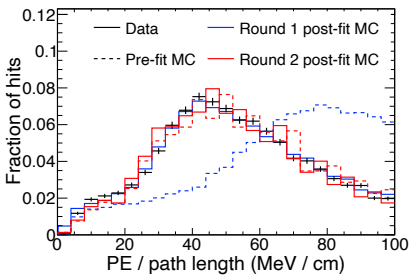

(h) Proton yz view

Figure 3.10. Distributions of PE per unit path length before (dashed) and after (solid) fitting in first (blue) and second (red) rounds of light model tuning

like if its ReMId is less than 0.15;

- The starting points of the two tracks are within a distance of 0 cm $< |\Delta x|, |\Delta y| <$ 6 cm and 0 cm $< |\Delta z| <$ 10 cm, where $|\Delta x|$, $|\Delta y|$, and $|\Delta z|$ are the absolute differences of the coordinates of the two track starting points;
- No more than 3 hits in the event are off the tracks.
- No more than 0.1 GeV of energy in the event is off the tracks.

With these selections applied to both data and MC samples, muon and proton tracks are selected. As shown in Figure 3.11, energy loss per unit track length ($\frac{dE}{dx}$) vs. residual track length is compared between data and MC to validate the light model.

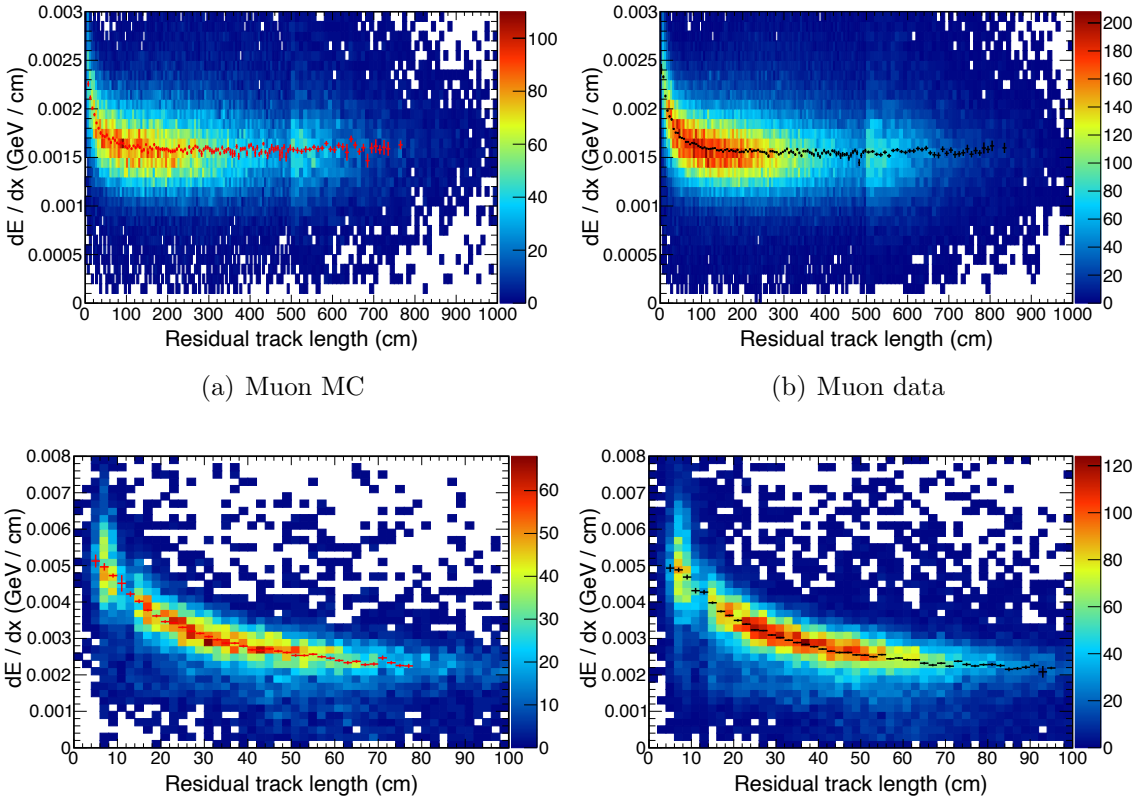

(a) Muon MC

(b) Muon data

(c) Proton MC

(d) Proton data

Figure 3.11. Energy loss per unit track length vs. residual track length distributions with red (black) histogram representing peak profile of MC (data) sample

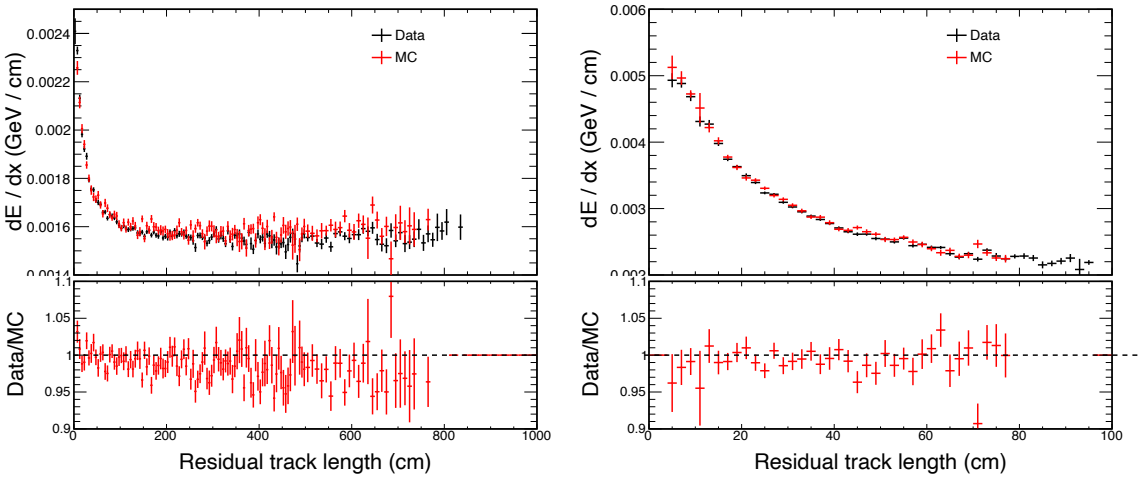

(a) Muon tracks (b) Proton tracks

Figure 3.12. Peak profiles of the $\frac{dE}{dx}$ vs. residual track length distributions from Figure 3.11 with ratio of data to MC shown at the bottom of each plot

The peak profiles of these 2D spectra and the data to MC ratios of the profiles are plotted in Figure 3.12. To quantify the normalization differences between data and MC energy profiles, χ^2 values are calculated over a range of normalization constant "Scale" to get the minimal χ^2 value defined as

$$\chi^2 = \sum_{i=1}^{N} \frac{(\text{data}(i) - \text{Scale} \times \text{MC}(i))^2}{\text{Error}^2_{\text{data}}(i) + \text{Error}^2_{\text{MC}}(i)}, \tag{3.4}$$

where i is the bin index from 1 to N; data(i) is the value of $\frac{dE}{dx}$ in bin i of the data peak profile; MC(i) is the value of $\frac{dE}{dx}$ in bin i of the MC peak profile; $\text{Error}_{\text{data}}(i)$ represents the statistical error of data in bin i; and $\text{Error}_{\text{MC}}(i)$ represents the statistical error of MC in bin i. The normalization constants (Scale) corresponding to the minimal χ^2 values of fitting MC to data samples are extracted from separate muon and proton track samples, and are listed in Table 3.4.

By using Equation 3.2, we can estimate the proportions of Cherenkov photons ($\epsilon_C C_\gamma / N_\gamma$) for the muon and proton track MC samples separately. Approximately 5% of photons produced in the muon sample are Cherenkov photons, and for the

Table 3.4. Normalization Constants for Minimal χ^2 Values

	muon	proton
Scale	0.9899	0.9577

proton sample the fraction of Cherenkov photons is 0.5%. The majority of light production in the NOvA detectors is thus contributed by scintillation light. Based on the normalization constants in Table 3.4, the muon tracks have a smaller discrepancy (1%) between MC and data, and the proton tracks have a larger discrepancy (4.3%). The muon tracks have an overall better data/MC agreement, since the majority of the samples used for light model tuning are muon tracks either from cosmic rays or the NuMI beam. Compared to the previous analysis, the discrepancy for muons (protons) was 3% (4.3%). Since the lepton energy contributes roughly 80% of the neutrino energy, this improvement helps to reduce the uncertainty of neutrino energy reconstruction. In future analyses, an improved beam selection, using particle identification, may give us a purer proton track sample, which may lead to an improvement in the data/MC agreement of the proton tracks as well.

A proper evaluation of the systematic uncertainty of the Cherenkov photon proportion, called Cherenkov systematic uncertainty [19], was designed to cover the uncertainties of splitting detector light response into scintillation and Cherenkov photons. There are two other systematic uncertainties, called "light level up" and "light level down." The "light level up" ("light level down") systematic uncertainty scales up (down) the total number of simulated photons to account for the possible data/MC overall discrepancy caused by the detector light model [19].

NOvA uses cosmic muons to further calibrate the detectors. Two types of calibrations are performed: attenuation calibration and absolute calibration [19]. Attenuation calibration aims at calibrating the effects of detector geometry. Since the

detector cells are very long, the scintillation light captured by the WLS fiber and passed through the cell to the APD is naturally attenuated along the distance. The attenuation calibration is performed to correct the photoelectron signals based on the positions of the interactions within the detectors. Then, during the absolute calibration, the photoelectron signals are used to estimate the energy deposited in the detector cell by the interacting particle. After calibrating the energy depositions, with the subsequent reconstruction techniques (see Chapter 4), neutrino energy can be well reconstructed (see Chapter 5). The neutrino energy is used as an important physics scale in the measurement of the oscillation parameters (see Chapter 6).

CHAPTER 4

NOVA RECONSTRUCTION

As discussed in the previous chapter, the NOvA detectors are made of oriented orthogonal layers, allowing 3D reconstruction by combining the readouts from the xz planes and the yz planes. There are various reconstruction techniques employed in the NOvA experiment. They not only reconstruct different objects, such as a neutrino event, event interaction point, and outgoing particles of a neutrino interaction, but also reconstruct the corresponding physics variables, such as the energy of a neutrino event, position of the interaction point, and directions of outgoing particles. There are also some reconstruction algorithms aiming at identifying the identities of the reconstructed particles and events. NOvA oscillation analyses make use of these reconstructed variables as well as event classification and particle identification techniques. In this chapter, the main reconstruction techniques are discussed, starting with the neutrino interaction event reconstruction, followed by the reconstruction of the sub-structures, such as the interaction point, the outgoing particles, and the particle identifications.

4.1 Basic Reconstruction Techniques

A neutrino interaction event is also called a slice. It is an object that is reconstructed based on the time and space correlation of a group of hits using the information from the two views of each event. The algorithm that reconstructs slices is called *Slicer*. *Slicer* groups together all the hits that come from the same neutrino interaction or cosmic event. Since all the hits in a neutrino interaction event come from the same origin in space, the *Hough Transformation* algorithm [20] and the *Elastic Arms* algorithm [21] are used to search for the origin of the event, which is also called the global 3D vertex. Using the vertex, the *FuzzyK* algorithm [22] is applied to reconstruct final-state particles into objects called 3D prongs. A 3D prong

contains all the information about a final-state particle.

4.2 Final-state Particle Reconstruction

The *FuzzyK* algorithm has two parts, a clustering algorithm and a matching algorithm. The clustering algorithm groups hits into 2D clusters, called 2D prongs, in each detector view so that the total distance from the hits to the associated prongs is minimum. In the electron neutrino analyses, the primary outgoing leptons are electrons, which create showers, i.e., "fuzzy" tracks. The clustering result of a simulated electron neutrino interaction in the FD with two 2D prongs in each view is shown in Figure 4.1.

From the MC truth, we know that the xz prong 1 (2) and yz prong 1 (2) are produced by the outgoing proton (electron). However, with real data events, we never know the truth about the final-state particle identities. To match the two 2D prongs (one from each view) that come from the same outgoing particle, the matching algorithm compares the energy deposition patterns of the candidate 2D prongs from both views. The energy deposition pattern is represented as the energy fraction profile vs. the prong length. It reveals how the energy is deposited in the detector cells along a 2D prong. At the starting point of the 2D prong, the energy fraction is zero; at the ending point, the energy fraction is 1. The matching algorithm compares the energy deposition pattern of each 2D prong in one view to all the energy deposition patterns of the 2D prongs in the other detector view. Two similar patterns indicate that the two 2D prongs (xz view, yz view) are projected from the same final-state particle. These two 2D prongs are then matched and defined as a 3D prong object which describes a final-state particle. Figure 4.2 shows the energy deposition patterns of the 2D prongs from the event in Figure 4.1, which is used as an example to illustrate the matching algorithm.

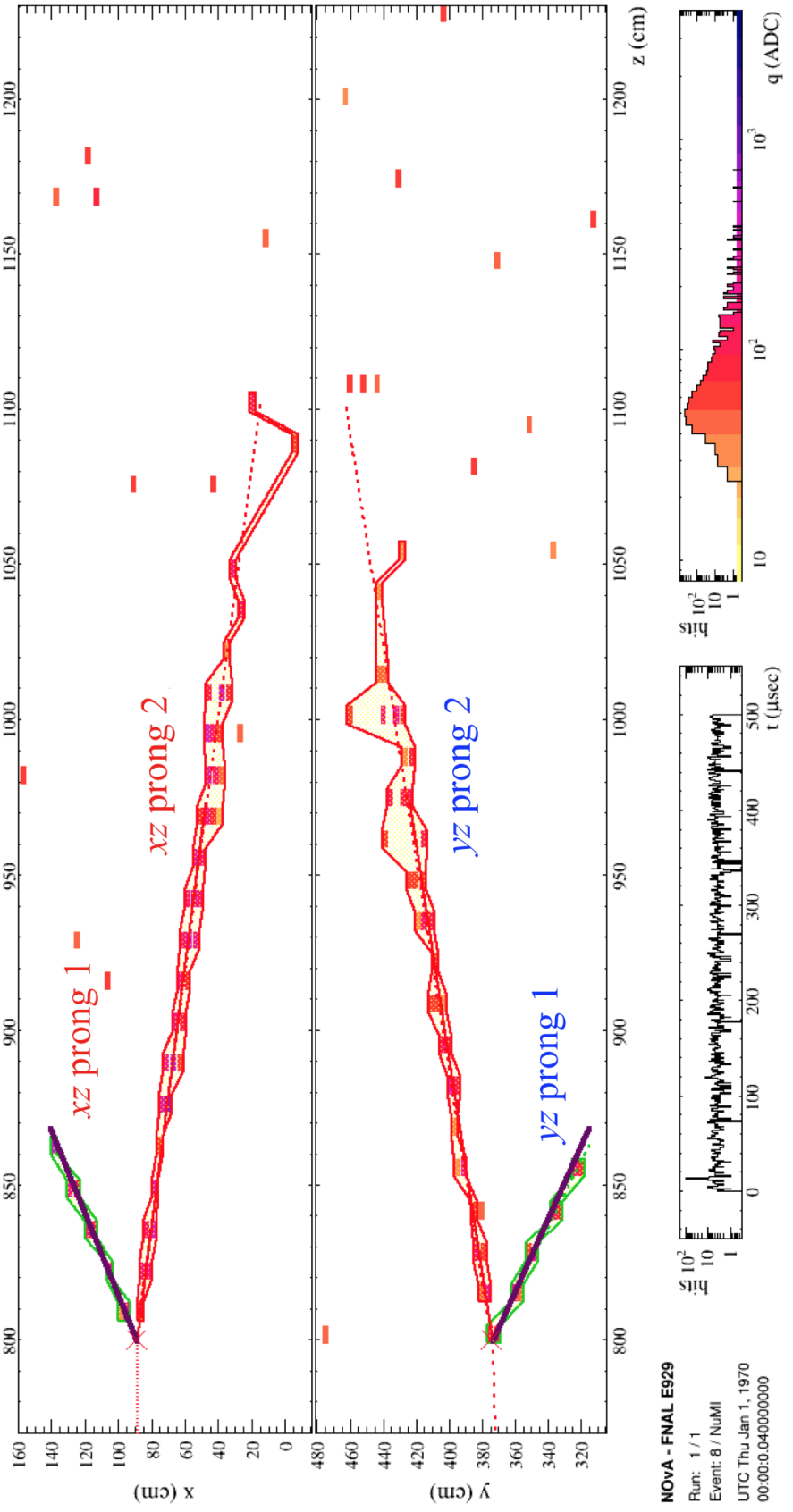

Figure 4.1. Event display of a simulated electron neutrino interaction in the FD with two 2D prongs in each view [23]

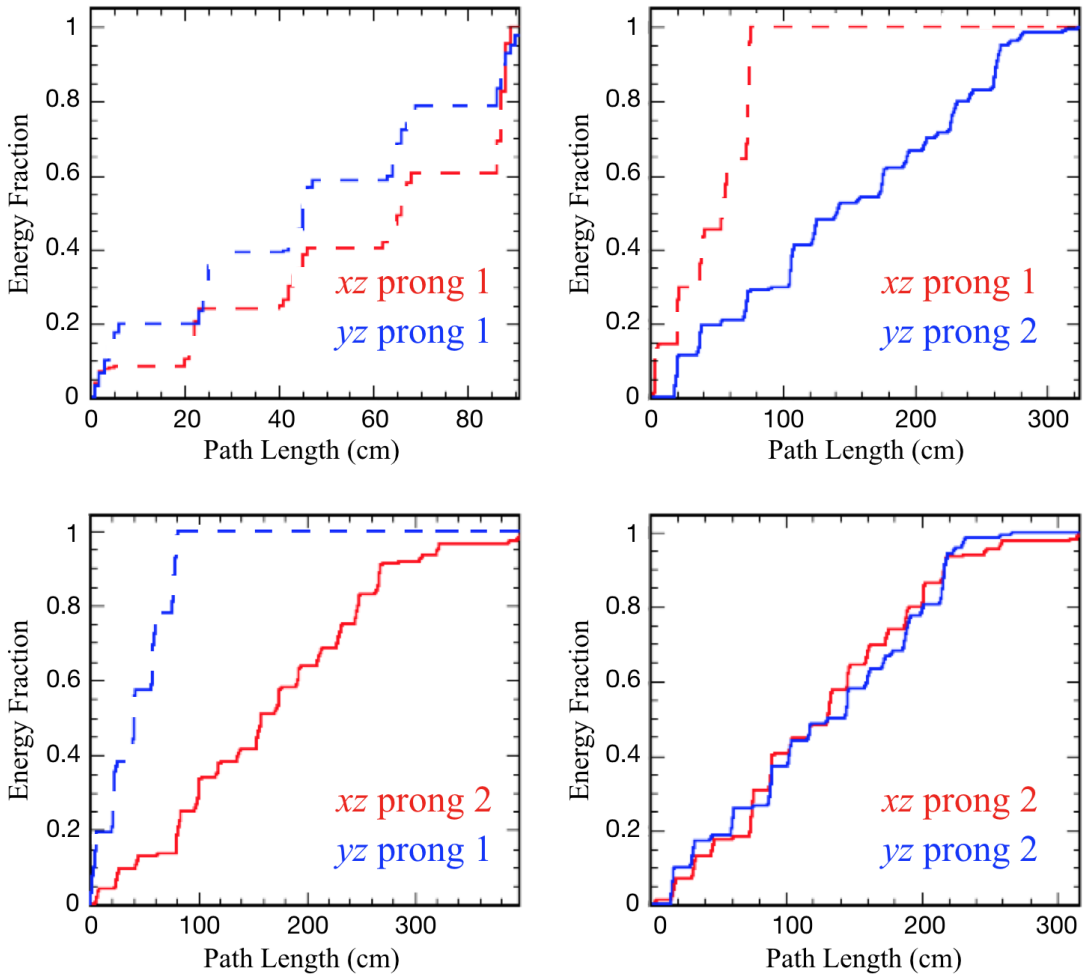

Figure 4.2. Energy deposition patterns of 2D prongs with scales of x-axis varied by 2D prong length [23]

When two 2D prongs are distinguishable by length, they have quite different patterns: the shorter prong approaches and remains 1 first, followed by the longer prong. The xz prong 1 and yz prong 2 in the top right plot of Figure 4.2 are examples of two 2D prongs with different lengths; because xz prong 1 is 90 cm in length while yz prong 2 is 300 cm in length, they are unmatched. The steps in the graphs of xz prong 1 and yz prong 1 are caused by the 2D alternating layer design of the detectors. A 3D particle is projected into the two detector views. When the particle passes through a detector cell in one view and deposits some energy, the energy

fraction increases in that view. Meanwhile, the energy fraction profile in the other view remains unchanged.

Even if two particles are similar in path length, the pattern of energy deposition can be still useful in the matching algorithm. Different types of particle have different patterns of energy deposition. For example, a final-state proton and electron are similar in length. The proton tends to have a linear relationship between energy loss and track length until the end of track, where the peak energy deposition occurs. So at the end of the proton energy pattern there may appear a larger step. The electron has a fuzzier trajectory. The hits generated by an electron are more spread over space instead of remaining in the initial direction of the electron. In this case, the energy fraction accumulates faster in the beginning of the electron path, then increases more slowly, which is not a linear pattern.

Once the final-state particles are reconstructed as 3D prongs by *FuzzyK*, a convolutional neural network (CNN) is applied to identify the particle types (IDs) of the 3D prongs. With the particle IDs reconstructed by the CNN, the 3D prong information can then be used for neutrino energy reconstruction as described in Chapter 5. The 3D prong particle IDs are also used to categorize the neutrino interaction types, which is important in NOvA neutrino cross section measurements.

However, it is not always the case that all the 2D prongs can be matched into 3D prongs. If the two views have unequal numbers of 2D prongs, there are unmatched 2D prongs in the event. Figure 4.3 shows an example of a simulated ν_e having unequal numbers of 2D prongs in the two views. From the MC truth we know that the neutrino interaction is a ν_e CCQE interaction ($\nu_e + n \rightarrow p + e^-$) and the true energy of the ν_e is 2.30 GeV, which is within the typical energy range of the NOvA analysis.

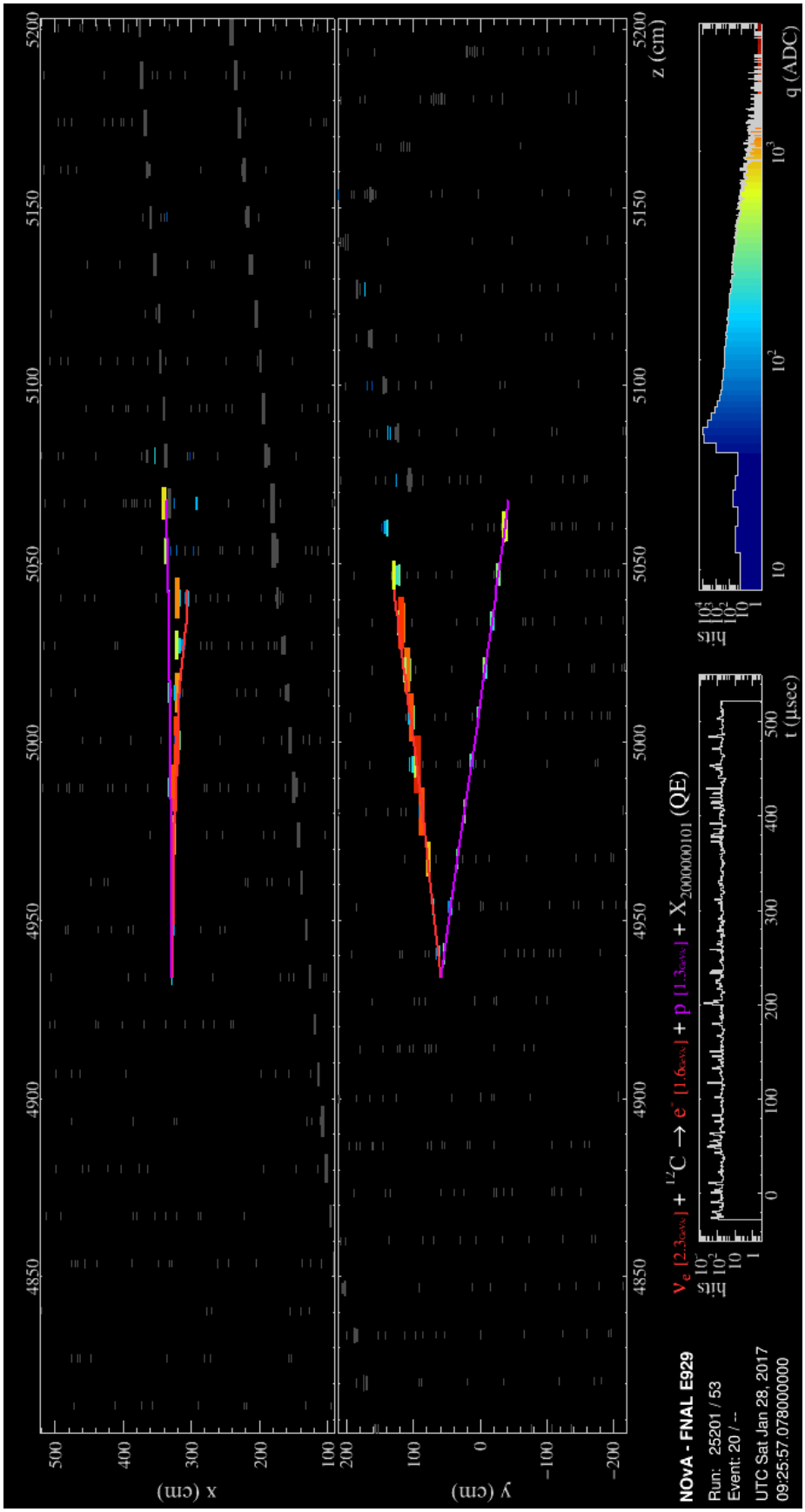

Figure 4.3. Event display of a simulated ν_e event with proton (red) and electron (purple) overlapped in xz view

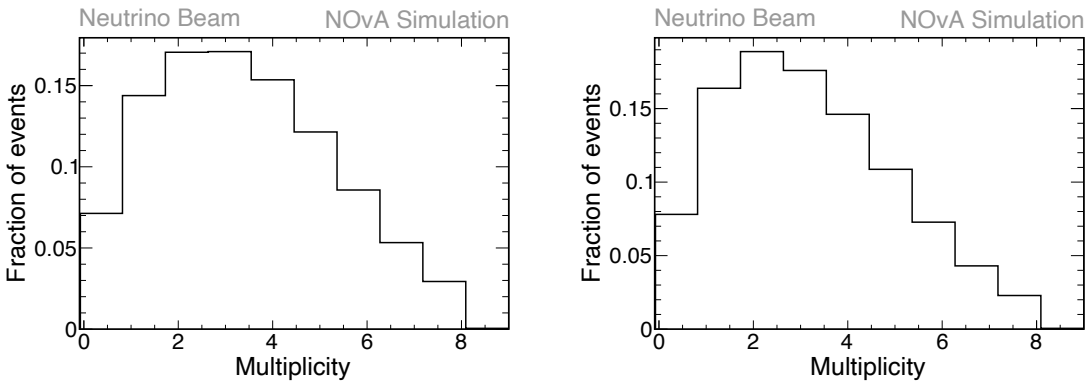

(a) ND MC (b) FD MC

Figure 4.4. Multiplicity distributions of unmatched 2D prongs

In the xz view of this event, the proton and the electron overlap and are hard for the *FuzzyK* clustering algorithm to separate. In the yz view, the proton track and the electron track are well separated. The track in purple is due to the proton moving to the lower right. The red track moving to the top right is made by the electron. Since there is one 2D prong in the xz view and two 2D prongs in the yz view, only one of the 2D prongs from the yz view is matched with the xz 2D prong. From the MC truth of the matched 3D prong, we know that the yz electron prong is matched with an xz 2D prong and the yz proton prong remains unmatched.

Unmatched 2D prongs have not previously been used in NOvA analyses. Figure 4.4 shows the multiplicity distributions of unmatched 2D prongs. There are 92.2% of reconstructed events in the FD containing at least one unmatched 2D prong, and the proportion at the ND is 92.9%. Hence, it would be beneficial to include the 2D prong information in future analyses.

I developed the use of the 2D prong CNN, which is different from the 3D prong CNN, for identifying unmatched 2D prong particle IDs, which has not been done in the past. Besides identifying unmatched 2D prongs, the 2D prong CNN can also identify the particle IDs of the 2D views of a 3D prong. In most cases, the 2D

views of a 3D prong should have the same particle type as the 3D prong. However, an unmatched 2D prong indicates that the reconstruction of the final-state particles in the event is not perfect. In this case, applying the 2D prong CNN on the two views of the matched 3D prong may provide additional information on the 3D prong particle ID to the NOvA analyses. With the additional information provide by the 2D prong CNN, the statistics will be increased for the NOvA analyses.

The 2D prong CNN is discussed later in this chapter, after first using the 3D prong CNN as an example to illustrate the CNN technique.

4.3 Convolutional Neural Network

The convolutional neural network is a well-known machine learning algorithm. It is widely used in many fields as a tool for image identification. Many physics experiments employ the CNN technique to identify particles or events captured by detectors, such as MicroBooNE [31] and ATLAS [32]. The CNN employed by a physics experiment is usually trained on MC files.

In general, a CNN consists of an input layer, hidden layers, and an output layer. The input layer feeds the input images to the CNN. The hidden layers are a group of layers with various functions. Each hidden layer takes the output image, called a feature map, from the previous layer, and performs some operations to produce its own feature map, which is fed to the next layer. The hidden layers are designed to learn the features of the input images by extracting abstract features, such as track-like, point-like, and shower-like structures. Different types of particles or events have different features of topology or energy response which can be used by the CNN for identification purposes. For example, in the NOvA detectors, most electron showers look fuzzier than muon tracks, as shown in Figure 4.5. These features are extracted by the hidden layers and used to identify the input images. The output layer assigns

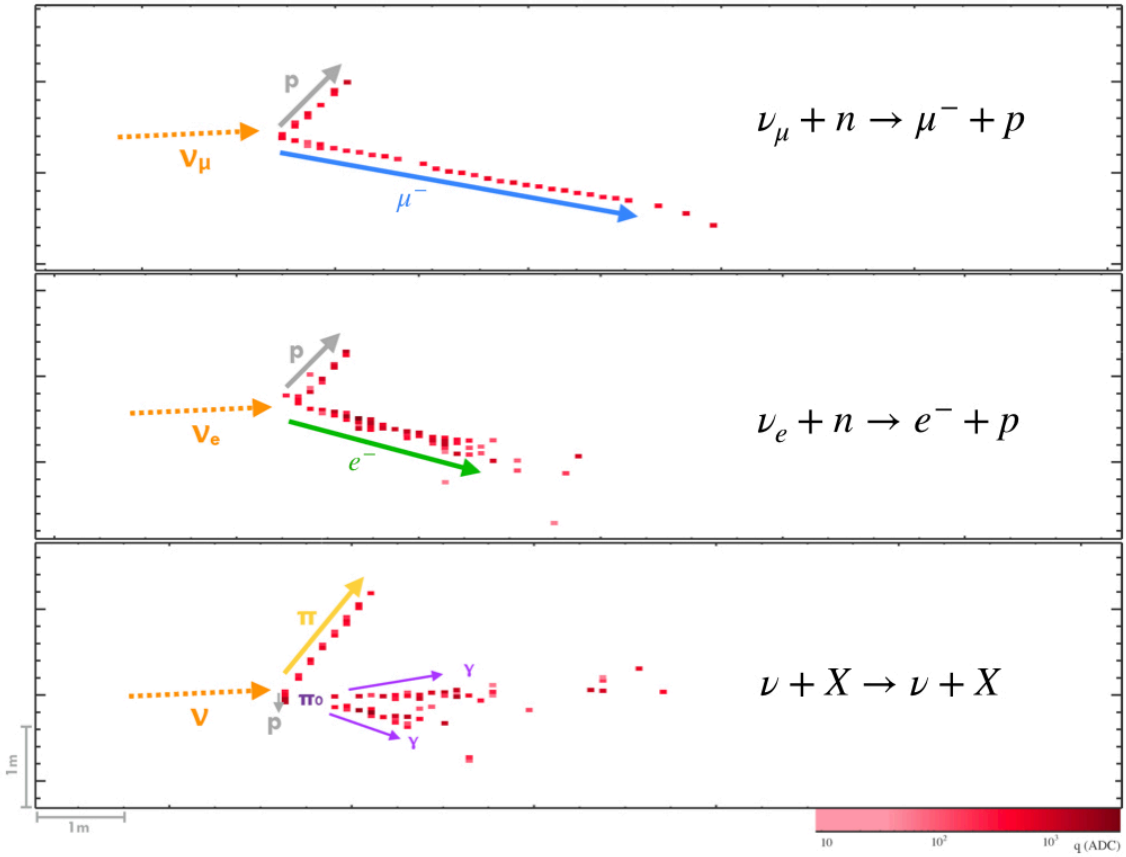

Figure 4.5. Event displays of simulated ν_μ (top), ν_e (middle), and neutral-current (bottom) events with outgoing particles labeled by MC truth

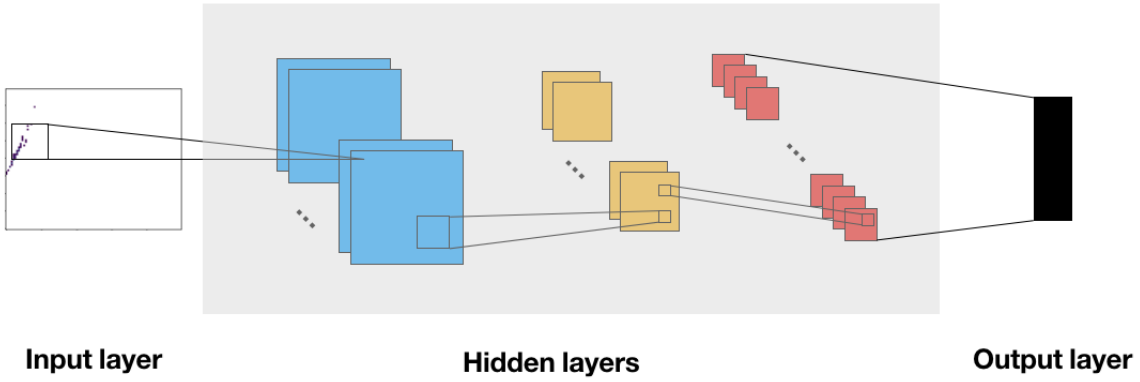

Figure 4.6. Graphical representation of a generic CNN taking a simulated electron as input to hidden layers in gray box

probabilities to the possible types of particles, where the sum of the probabilities must equal one. Figure 4.6 shows an example of a generic CNN diagram. The hidden layers are in the gray box. Three different hidden layers apply three different operations to their input feature maps. The blue, yellow, and red squares represent the output feature maps of the three hidden layers. The output layer in black delivers a vector of probabilities of the possible particle types.

The goal of a CNN is to approximate a function $f : \mathbb{R}^n \rightarrow \mathbb{R}^m$, where n is the dimensionality of the input image, and m is the length of the output vector. In the following subsections, the 3D prong CNN is used as an example to illustrate the details of different CNN layers.

4.3.1 Input Layer. One 3D prong CNN input object contains four images. Along with the images, an MC truth value, called a label, is also input to the input layer. The label provides the 3D prong MC true particle ID to the CNN for training purposes. When the trained CNN is applied to the real data to evaluate the particle IDs of the 3D prongs, the trained CNN needs only the images of the 3D prongs to identify particle types. In this subsection, the input images are discussed first, then the input labels.

The input images consist of pixel maps. Since the detectors have different responses to different types of particles, energy deposition along with event or particle topology is used by the CNN for identification purposes. The size of the pixel map is 80 cells in width (y-axis) and 100 cells in length (x-axis). Each pixel corresponds to one cell of the detector. When the particles pass through the detector cells, some energy is deposited in the cell, which is typically between 0 GeV and 2 GeV. The color, which is considered as the third dimension of the pixel map and is called depth, represents the amount of energy deposited in the cell. In general, if the image size is bigger, the processing time of the CNN is longer. Since the complete images of the NOvA detectors are too big for the CNN to process in reasonable computer time, a smaller pixel map with a size of 80×100 is selected in each view such that the vertex and prongs are fully contained in the image. The pixel maps of the simulated ν_e CCQE interaction in Figure 4.3 are shown in Figure 4.7.

If a prong is longer than 5 m or generates fewer than three hits, the prong is not used by the CNN. Because most tracks longer than 5 m are muons, and processing a large pixel map is computationally expensive, it is neither efficient nor necessary to

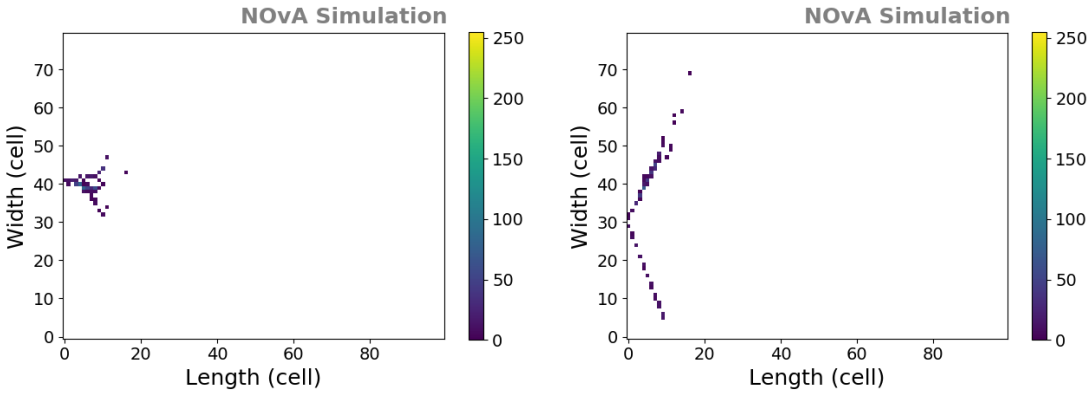

(a) xz view (b) yz view

Figure 4.7. Pixel maps of event view of the ν_e CCQE interaction in Figure 4.3 showing proton (bottom) and electron (top) trajectories well separated in yz view but overlapped in xz view

apply the CNN to these super-long prongs. And for a prong with fewer than three hits, the information contained in the pixel map is not enough for the CNN to make a reliable identification on the prong particle type.

For training purposes, the label of the object is input to the CNN along with its images. A label is the true identity of an object, which depends on the identification goal of the CNN. Taking the 3D prong CNN as an example, it has eight labels corresponding to the eight types of particles. They are *muon*, *electron*, *proton*, $\pi^{\pm}$, *neutron*, π^0, γ, and *other*. Since we use MC files to train the 3D prong CNN, the true particle IDs of the input objects are known from the MC truth and each object always belongs to one of the eight categories.[3]

4.3.2 Hidden Layers. A hidden layer studies and extracts the features of a pixel map by applying a function, which is also called a kernel matrix or feature filter, to the image. The output of a hidden layer is called a feature map and is input to the next layer. Each hidden layer does some operations or calculations on its input feature maps. There are various types of hidden layers, such as a pooling layer, a convolutional layer, or a normalization layer. In Figure 4.8, I fill the input feature map (Figure 4.8(a)) with some arbitrary values and use a 2×2 max pooling layer (Figure 4.8(b)), which covers four pixels at a time, to demonstrate how a max pooling layer picks up the local maximum values from the selected 2×2 regions and fills the output feature map (Figure 4.8(c)).

4.3.3 Output Layer. An output layer delivers a vector of probabilities ($\vec{p}$) for each individual input object. Each element of $\vec{p}$ represents the probability of the input object being identified as the corresponding label. For the 3D prong CNN, the length of the output vector is eight, and the eight probabilities add up to one. All the

[3]The *other* label includes all the other types of particles that do not belong to the first seven types.

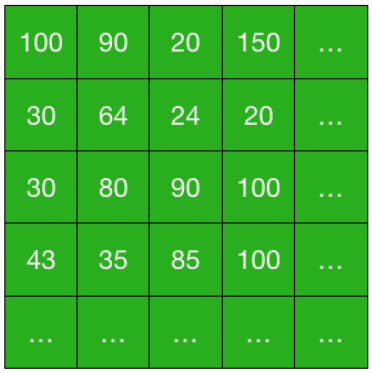

(a) Input feature map

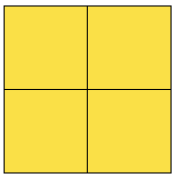

(b) Max pooling layer kernel

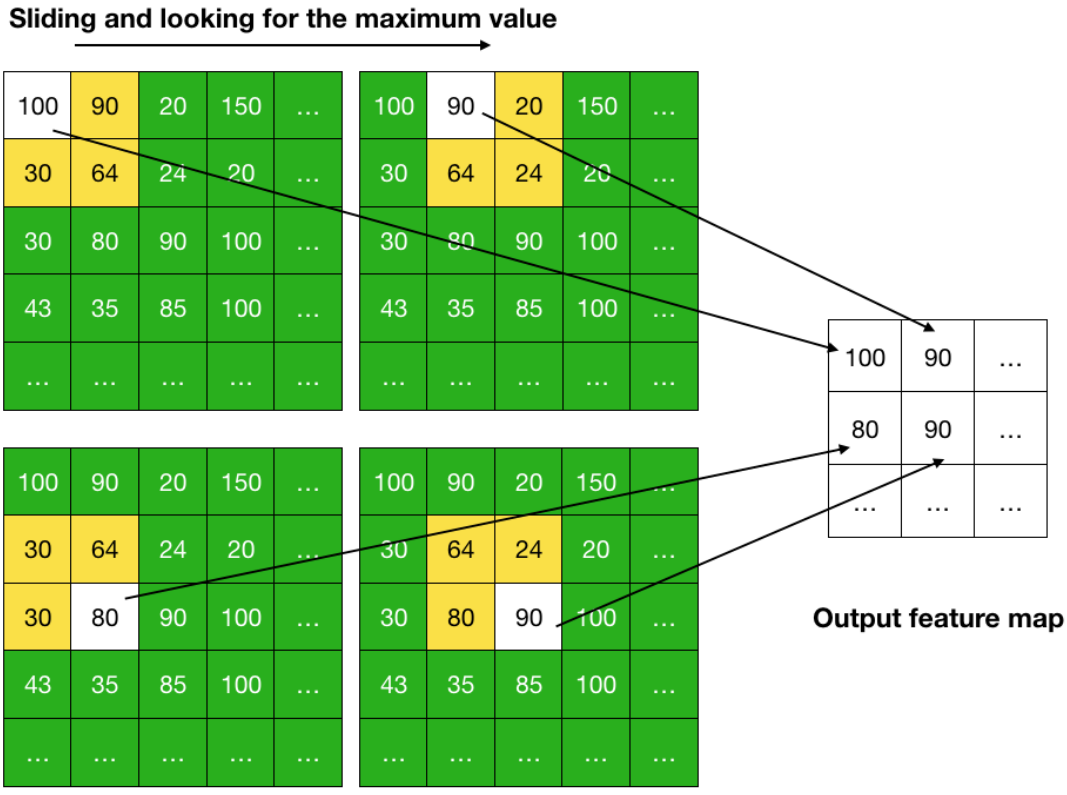

(c) Kernel sliding across the input feature map

Figure 4.8. 2×2 max pooling layer kernel sliding across input feature map to extract local maximum values and fill output feature map

eight probabilities are useful in the analyses, and the one with the highest probability is assigned to the 3D prong as the reconstructed particle ID.

4.4 Prong CNNs

There are several CNNs employed in NOvA, two of which are the 3D particle identifier (3D prong CNN) and 2D particle identifier (2D prong CNN). The reason that two different identifiers are employed separately for 3D prongs and unmatched 2D prongs is that they have different input image requirements.

4.4.1 Input Layer. Figure 4.9 shows the pixel maps of the matched 3D prong, which comes from the ν_e event in Figure 4.7. Figure 4.10 shows the pixel maps of the unmatched proton prong, which comes from the yz view of the same event.

The input layer of the 3D prong CNN takes four pixel maps as one object, including the two (xz and yz) pixel maps of a 3D prong and the two pixel maps of the event. With these four pixel maps, the 3D prong CNN assigns the reconstructed particle ID to the 3D prong. But the 3D prong CNN is not able to identify the unmatched 2D prongs for the following reasons. As shown in Figure 4.10, an unmatched

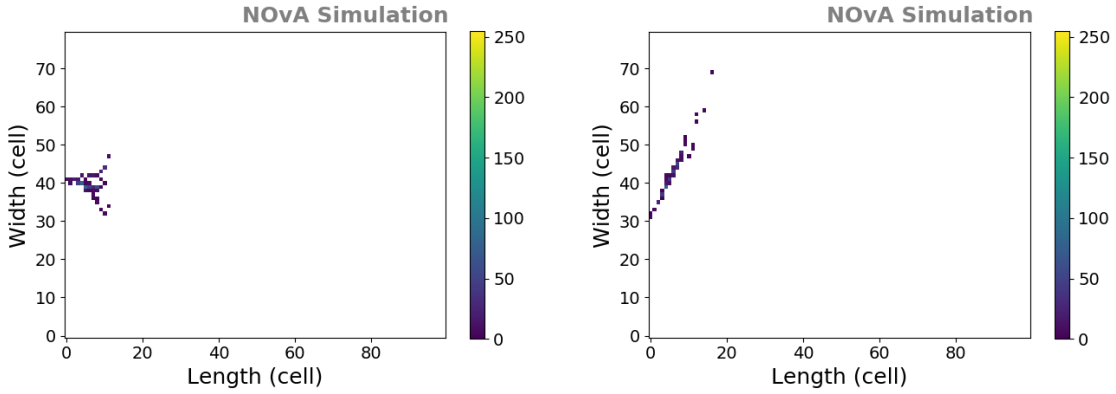

(a) xz view (b) yz view

Figure 4.9. Pixel maps of a matched 3D prong

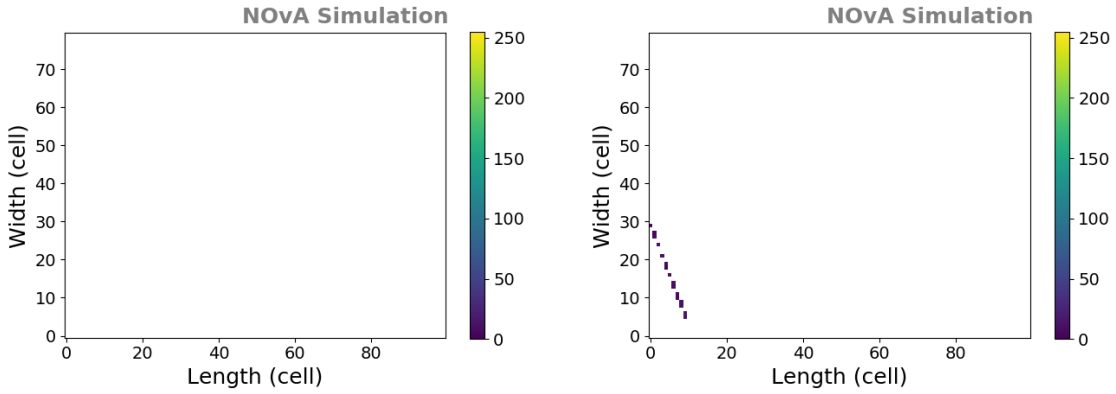

(a) xz view (b) yz view

Figure 4.10. Pixel maps of an unmatched 2D prong with no 2D prong in xz view and one 2D proton prong in yz view

2D prong has only one view that contains a cluster of hits, either the xz view or the yz view, while the other view is empty. The empty view has no information for the CNN to use, hence is not effective as input to the CNN. Therefore, for each unmatched 2D prong, there are at most three pixel maps that can be used as effective inputs, which does not meet the input requirements of the 3D prong CNN.

I invented and trained the 2D prong CNN to identify the 2D prong particle IDs. The structure of the 2D prong CNN is illustrated in Figure 4.11. It has a similar structure as the 3D prong CNN but adjusted for the 2D prong input requirements. Both CNNs are based on MobileNetV2 [24], which was developed by Google.

4.4.2 Structure of 2D Prong CNN. In Figure 4.11, the bottleneck structure consists of a group of hidden layers, which increase the depth of the network by adding more layers. At the same time, the bottleneck structure maintains the size of the output feature map the same as that of the input feature map to avoid an increase in processing time for the following layers. It also feeds the feature map from the previous layer to the downstream layer by skipping some layers in between to make sure the previous features are not ignored [24]. A short muon track with a Michel

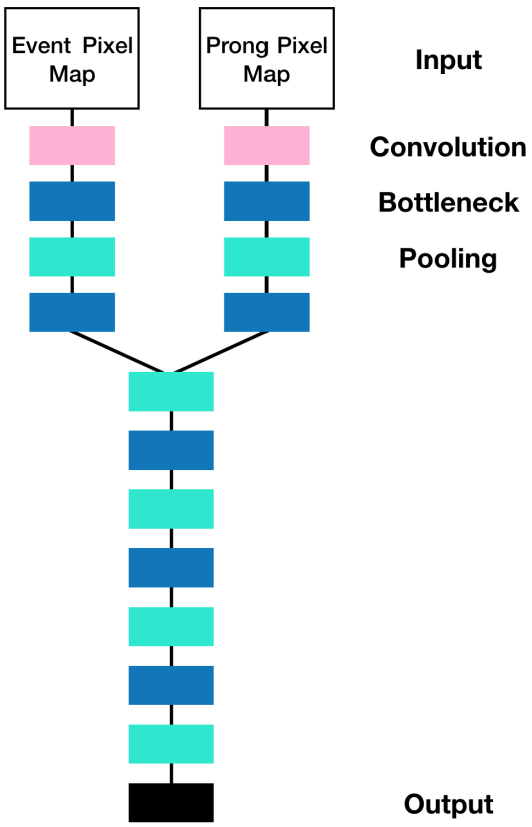

Figure 4.11. Structure of 2D prong CNN

electron at the end is used as an example to illustrate why the additional residual information can be helpful in particle identification. Because the muon's track-like feature is more pronounced than some tiny features close to the end of the track, without the additional information from the upstream feature map, the in-between layers may extract the track-like feature and ignore the tiny Michel electron shower structure, which only consists of a couple of low energy hits close to the end of the muon track. In this case, the CNN may not be able to distinguish well among short muon tracks with Michel electrons and other short-track particles, such as proton and pion tracks.

4.4.3 Training and Test Data Sets. The CNN is trained on the FD MC files in HDF5 [25] format. Both FHC and RHC datasets, including ν_μ, $\bar{\nu}_\mu$, ν_e, and $\bar{\nu}_e$ events,

are used to ensure that the different types of particles and events are sufficiently represented in the training datasets. Because the component composition of the training sample affects the outcome of the training, extra care is taken to make sure that there are similar numbers of all particle types in the training data samples. If one type of particle is more prevalent than the other types, the training can be biased so that the trained CNN is not able to identify the rare particle types and tends to identify all of the input as the majority type. For example, in the FD selected ν_μ or ν_e samples, there are more muons or electrons than charged pions. To avoid this possible problem, we randomly delete some particles of the majority types so that the numbers of the different types are balanced. This procedure is called sample balancing. After the sample balancing, we have similar numbers of each type of particle in the datasets prepared for training and testing.

The files from the FHC and RHC datasets are randomly shuffled and then split into two parts. One part, containing 80% of the dataset, is used for training (the training dataset). The other part is the test dataset, containing the remaining 20%. Randomly shuffling and splitting are generic sample preparation techniques in machine learning and ensure that different types of particles and events have equal opportunities to be used in the training. Because the purity of the unmatched 2D prongs is too poor to be used for training, the 2D views of the 3D prongs are used to train the 2D prong CNN.

The series of selections is as follows. The containment selection is applied to ensure events, 3D prongs, and 2D prongs are fully contained within the detector volume: keeping at least 12 cm away from the bottom and sidewalls of the FD; and keeping 63 cm away from the top of the FD to avoid possible overlaps with cosmic backgrounds incident from the top. The number-of-hits selection requires each input pixel map to contain at least three hits. There is also purity selection,

which is based on the purity of the 3D prongs. The purity of a 3D prong is defined in the following way. The outgoing particles in a neutrino interaction event may have trajectories overlapping each other. Hence, one reconstructed 3D prong can contain hits from more than one particle. Based on the MC truth, the 3D prong's particle ID is assigned as that of the particle with the biggest contribution in energy. The purity of the 3D prong is defined as the ratio of the total energy of the hits from the dominating particle to the 3D prong total energy. The required values of 3D prong purity are listed in Table 4.1.

Table 4.1. Values of 3D Prong Purity Selections

muon	electron	proton	γ	$\pi^{\pm}$
0.5	0.4	0.35	0.5	0.35

Ideally, at least 50% of the prong energy should be contributed from the same particle. But this is not always true for all types of particle. Since the NOvA detectors are segmented in 6×3.87 cm^2 cells, they are better at reconstructing particles with longer tracks. For a long track, such as a muon track, even if the beginning overlaps some other particles, it can still be well reconstructed and have a high purity. When all the outgoing particles are short tracks and close to each other, *Fuzzyk* can easily cluster hits from different particles into the same prong, thus the proportion of energy contributed by each particle can easily drop below 50%.

To get a balanced sample for CNN training, the last "selection" is to randomly delete some entries in all labels except for $\pi^{\pm}$, which already has the lowest statistics in most of the files. Before applying these selections, the proportions of particle types of 3D prongs are as listed in Table 4.2. The other particle types are so rare in the files that they are neglected in the sample balancing and in the table. After applying the selections, the training sample contains 818,700 entries with equal numbers of each label. The training was performed on Cooley, a visualization cluster at Argonne

Table 4.2. Composition of Training Sample Before Selections Applied

muon	electron	proton	γ	$\pi^{\pm}$
0.307	0.510	0.063	0.094	0.026

National Laboratory for scientific data analysis and visualization, and it took 36 hours to converge and become stable.[4]

4.4.4 Training and Test Metrics. The loss metric is used in training and is discussed first, followed by the accuracy metric, which is used in testing.

The loss metric measures the error between the output of the CNN and the MC truth. Its gradient as a function of the parameters in the matrices of the CNN model is calculated using the back-propagation algorithm [28]. Following the Mini-Batch [29] training strategy,[5] in the case of 2D prong CNN training, a batch consists of 128 input 2D prongs, which means 128 input 2D prongs are simultaneously evaluated in a batch; this constitutes one iteration of the training. The parameters in the matrices of the CNN model are revised at the end of each iteration so that the training moves in the direction of reducing the average loss value of the batch.

A loss value is calculated for each 2D prong based on the output probability vector by using the multinomial logistic loss [30] function:

$$\text{loss} = -\sum_{i=\{\text{labels}\}} t_i \ln p_i \,, \tag{4.1}$$

where the output vector ($\vec{p}$) contains eight predicted probabilities corresponding to

[4]The training was performed using *Keras*, an open-source neural-network library written in Python [26]. The scripts are available online [27].

[5]Batches are used because it is inefficient and computationally impractical to input the entire training dataset to the CNN at once.

the eight labels; p_i, an element of $\vec{p}$, is the predicted probability of label i; and t_i is the binary indicator of label i. For an input 2D prong with true label l, the binary indicator is defined as:

$$t_i = \begin{cases} 1 & i = l \\ \\ 0 & \text{otherwise}\,. \end{cases} \tag{4.2}$$

Summing over all the labels, only if i is the same as the true label (l) of the 2D prong does the binary indicator equal one, and the corresponding p_i, which is the probability of the correct identification, contributes to the loss value in Equation 4.1. If the probability of the true label is close to one, then the loss value is close to zero, which means the correct identification made by the CNN has tiny error. But if the probability predicted by the CNN is tiny on the true label, then the loss value is huge, which means the error of the probability of the correct identification is huge. The loss value can even go to infinity if the predicted probability of the true label is zero.

The accuracy metric quantifies how frequently the trained CNN makes the correct prediction by using the test data set. It is defined as

$$\text{accuracy} = \frac{\text{Number of correct predictions}}{\text{Total number of predictions}}\,, \tag{4.3}$$

where the denominator is the batch size of testing (128), and the numerator is the number of correct identifications in a batch, where a correct identification means that the label with the highest probability assigned by the CNN agrees with the true label.

There are 2,500 iterations in one epoch. For each iteration, the loss value per iteration is averaged over 128 2D prongs. After one epoch, the CNN has approximately processed and evaluated the entire training dataset once. However, one epoch

(seeing the entire training dataset once) is not enough to ensure the average loss value has been minimized. More than one epoch are used in the training to ensure that the average loss value is truly minimized and stable before the training is ended. Figure 4.12 shows the accuracy and loss curves versus iteration count. The training loss is a rolling average of 128 training data samples. The test loss (accuracy) is the rolling average loss (accuracy) over 128 test data samples. The similar training and test loss indicates that the network has similar performance on training and test data sets, and is not badly over trained. At the end of training, the test accuracy rises to 0.76 while the loss curves drop to 0.6, and all three curves become stable.

The 0.76 test accuracy means 76% of time, the CNN makes correct predictions

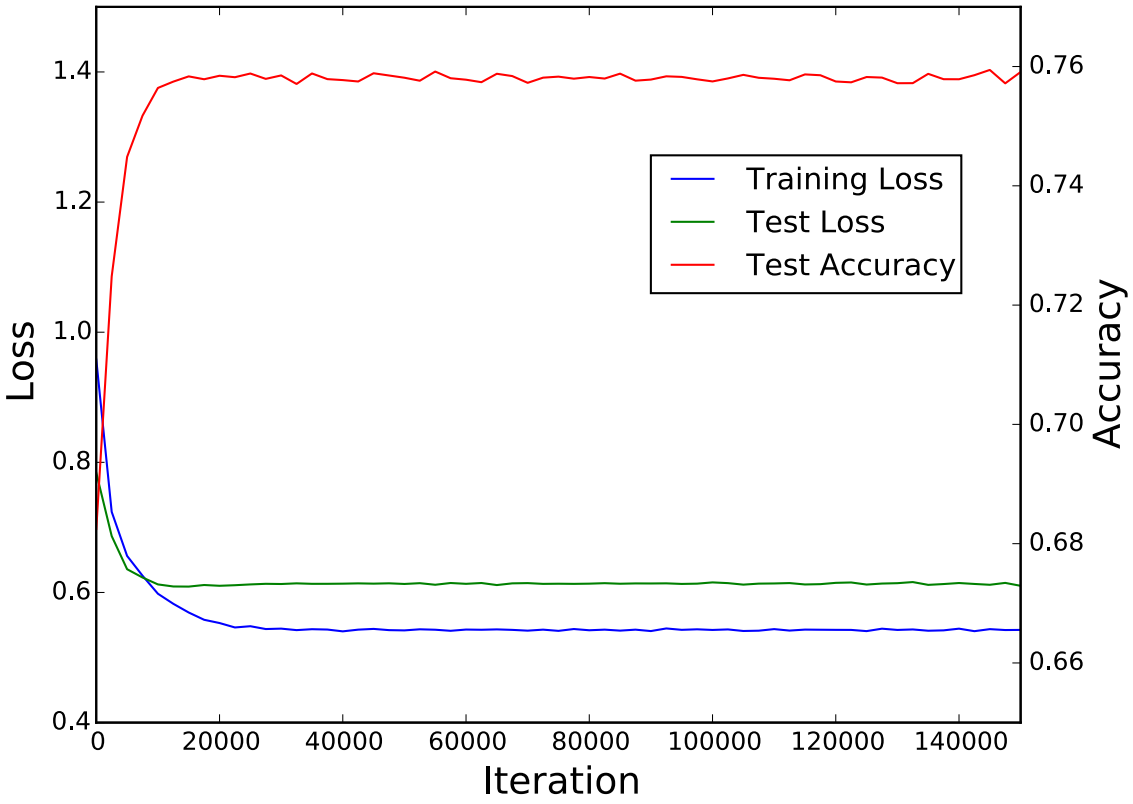

Figure 4.12. Loss calculated on the training data set (blue) and test data set (green), and accuracy calculated on test data set (red) as functions of iteration count

about the particle IDs of 2D prongs. It could be due to the difficulty of distinguishing outgoing electrons from photons, which are both usually in the form of an electromagnetic shower: high-energy photons interact with matter via pair production; and high-energy electrons and positrons emit photons when they decelerate. In the balanced data set, the proportions of electrons and γs are each 20% of the total.

The loss value of 0.6 qualifies the error of the prediction made by the CNN. Using Equation 4.1, the probability p_i of the correct prediction ($i = l$, where l is the true label) is determined by $-\ln p_i = 0.6$, which gives $p_i = 0.55$. Taking the same example of electron, this means when the CNN predicts the 2D prong particle type as electron, the probability of this prediction is 0.55. The averaged loss is 0.6, which means the probabilities of the CNN to distinguish the particles is more than 50%. Since there are eight labels, the probability of randomly picking one label is $\frac{1}{8}$. Compared to this value, a probability of 0.55 is way better, and the loss value of 0.6 is thus reasonably low.

4.4.5 Result. Once the CNN model is trained, we run it with the test data set to evaluate the performance of the CNN. Some generic techniques are used, such as the classification matrix and particle ID distributions.

A classification matrix is shown in Figure 4.13. The elements having their predicted label (x-axis) the same as their true labels (y-axis) represent the correct identifications made by the CNN. They are much darker in color compared to the remaining elements, which indicates that the CNN model has good performance in identifying 2D prong particle IDs. To get a better sense of the performance, we need to normalize the matrix in a special way. The normalization can be applied either by column or by row. Either way tells a similar story about the CNN performance. The column normalized matrix (Figure 4.14) is used as an example. After normalization, the sum of each column in the matrix equals one. The elements in a column

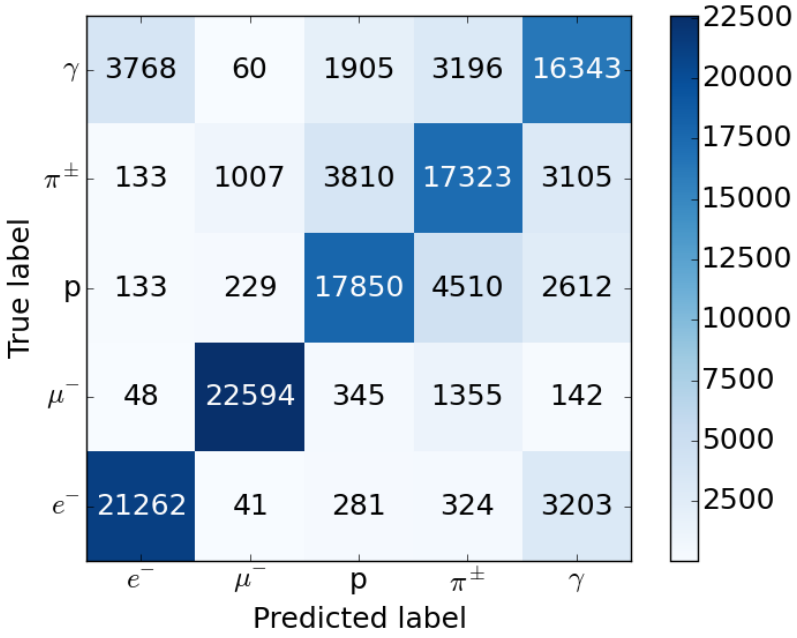

Figure 4.13. Unnormalized classification matrix of true labels (row) vs. predicted labels (column) with color representing number of 2D prongs in each entry

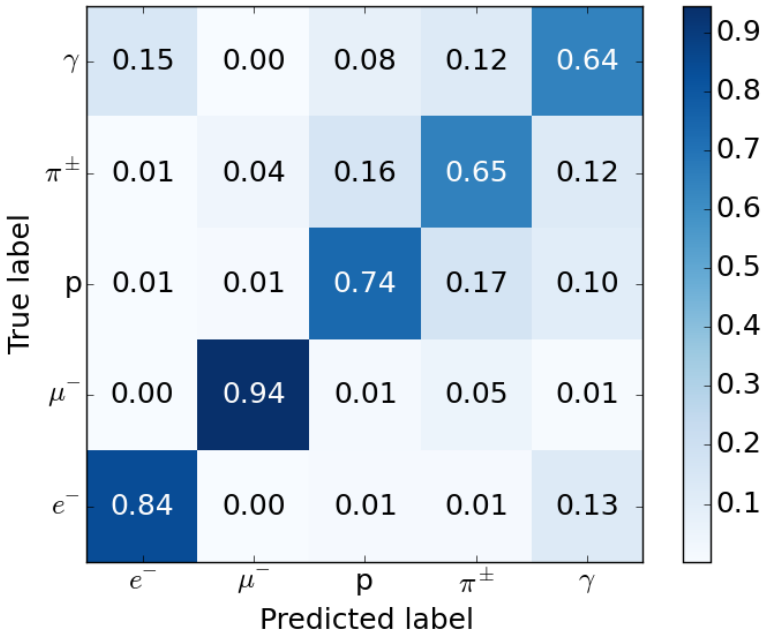

Figure 4.14. Column normalized matrix of true labels (row) vs. predicted labels (column) with color representing fraction of 2D prongs

indicate the proportions of all the true labels. The diagonal of the matrix indicates the proportions of the correct identifications. That means, looking at a column (for example, electron), among all the 2D prongs that are predicted to be electron 2D prongs, the fraction of the 2D prongs that are truly formed by electrons is 0.84. In the same column, 15% of the 2D prongs that are predicted to be electron 2D prongs are formed by a true γ. The proportion of true γs has the second largest value among the predicted electron 2D prongs. This is because electrons and γs are difficult to distinguish from each other in the detector, as described above. For a similar reason, muons (track-like) and electrons (shower-like) are easy to distinguish, and the proportion of true muons is thus 0, meaning that none of the predicted electron 2D prongs is formed by a true muon. The proportion, i.e., column normalized matrix element, is defined as:

$$M_{i,j} = \frac{C_{i,j}}{\sum_{i=\text{labels}} C_{i,j}}\,, \tag{4.4}$$

where i and j are row and column indexes, $C_{i,j}$ is the classification matrix element at row i, column j, and $M_{i,j}$ are the normalized matrix elements.

Figure 4.15 shows the CNN-identified particle ID distributions of the 2D prongs. Most true particles are correctly identified, having their probabilities close to one, while the background events in each plot have small probabilities, meaning that these events are identified to be background to the corresponding particle type. These particle ID plots show that the performance of the trained CNN is good enough to separate the true particles from the backgrounds for each presenting particle type. Hence, the trained CNN is good enough for identifying the 2D prong particles.[6]

[6]There are barely any particles in the "other" category for the CNN to train on or to evaluate, so its particle ID distribution is different from those of the other categories due to lack of statistics.

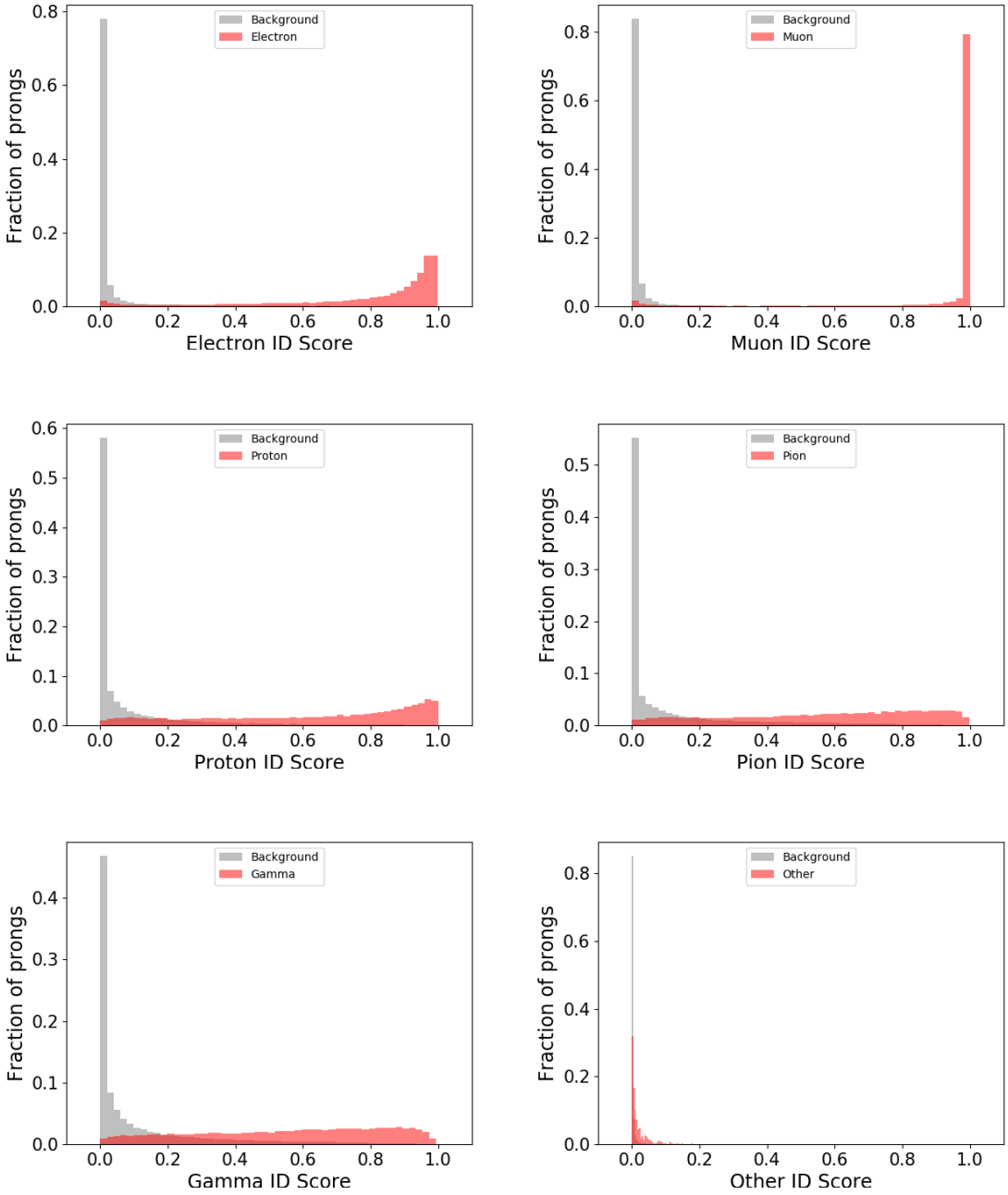

Figure 4.15. Distributions of 2D prong CNN predicted particle ID with red histograms representing true particles and gray histograms representing all the other types of particles (background)

The 2D prong CNN provides additional information for unmatched 2D prongs, which have not previously been used in NOvA analyses. With this information, we can improve both the event identification and energy estimation. These two

improvements may lead to improving the sensitivity of NOvA results by reducing systematic and statistical uncertainties. The 2D prong CNN is used in ongoing cross section measurement studies to identify unmatched 2D prongs and further identify the events. It is also used in the electron (anti)neutrino reconstruction [33] studies, providing an alternative method to that used in the NOvA 2020 analysis. The 2D prong CNN has been added to the official production chain of NOvA and its results will be used in future analyses.

CHAPTER 5

ELECTRON (ANTI)NEUTRINO ENERGY RECONSTRUCTION

The approach to the energy reconstruction of the ν_e signal events is based on the assumption that the energy response of the detectors is inherently different for leptonic and hadronic components, which are both present in our signal events. The energy reconstruction of electron (anti)neutrino events makes use of the 3D prong information, including the 3D prong CNN classified particle IDs. The reconstructed ν_e ($\bar{\nu}_e$) energy is defined as a function of the leptonic and hadronic components.

In the study of electron (anti)neutrino energy reconstruction, two energy estimators are trained. One is trained on the FHC MC files for the neutrino signal events ($\nu_\mu \rightarrow \nu_e$) and the other on the RHC MC files for the antineutrino signal events ($\bar{\nu}_\mu \rightarrow \bar{\nu}_e$). The methodology and procedures of energy reconstruction for ν_e and $\bar{\nu}_e$ are similar. In this chapter, the FHC energy estimator is used to demonstrate how to reconstruct the energy of ν_e signal events. Then, the results of both ν_e and $\bar{\nu}_e$ energy estimators are shown and discussed.

5.1 Selection

In this section, I describe the selections that are applied to the FD MC files to remove background events and to ensure the quality of the ν_e signal events. The selections, which are based on the ν_e appearance analysis (Chapter 6) selections, consist of basic quality selection, detector containment selection, loose event identification (ID) selection, loose analysis selection, and MC truth selection. The basic quality selection and the detector containment selection are the same as the ones applied in the ν_e appearance analysis. The loose event ID and loose analysis selections are based on the corresponding ν_e analysis selections. The details of the selections are as follows:

1. The basic quality selection makes sure that events are well reconstructed with all the necessary reconstruction objects: one slice, one vertex, and at least one 3D prong. It also makes sure that events are in the beam time window, i.e., detected while there is a beam pulse delivered by the NuMI beam.

2. The containment selection requires the minimum distance of all the 3D prongs in an event to be at least 12 cm from the sidewalls and the bottom wall of the FD; at least 18 cm from the front and back walls of the FD; at least 63 cm from the top of the FD. With the containment selection applied, the majority of ν_e signal candidates are kept for analysis while incident cosmic rays and partially contained events are removed.

3. The loose event ID selection requires the probability of the event CNN to classify an event as a ν_e interaction candidate to be at least 0.75.

4. The loose analysis selection requires that the length of the longest 3D prong in an event is between 1 and 5 m; an event consists of 30–150 hits; and true energy of any ν_e event is in the range 0.5–4.5 GeV.

5. The MC truth selection ensures all the events are truly $\nu_\mu \rightarrow \nu_e$ events.

The MC samples used in the energy reconstruction studies consist of the full MC dataset, generated by the NOvA production group within the production-5 campaign for the 2020 analysis. The MC files are evenly split into two parts. Half of the MC files are used to fit for the estimator, the other half are used to validate the performance. The number of events for fitting (validating) after all the necessary selections is 1,145,610. Flux weights, which are generated by the PPFX generator [16], are applied to the MC events. These weights account for beam-dependent corrections which include the beam focusing and the hadron production of the NuMI beam.

Given that electromagnetic (EM) and hadronic (HAD) depositions have different response in the detector, a fit to true neutrino energy as a function of the reconstructed EM and HAD energy components is performed to reconstruct the energy of ν_e signal events. All the 3D prongs are first classified as either EM-like or HAD-like. This is done by using the output predictions of the 3D prong CNN. The score to classify prongs as EM-like is given by:

$$\mathrm{CNN}_{\mathrm{EM\ ID}} = \mathrm{CNN}_{\mathrm{electron\ ID}} + \mathrm{CNN}_{\gamma\ \mathrm{ID}}\,. \tag{5.1}$$

If a prong satisfies $\mathrm{CNN}_{\mathrm{EM\ ID}} > 0.5$, then it is classified as an EM-like prong, also called an EM shower. Otherwise, it is a HAD-like prong. The electron neutrino energy estimator (E_{reco}) is defined based on the 3D prong information. EM shower energy (E_{EM}) is calculated by summing over all the EM-like prong energies in an event. Then, the corresponding HAD energy is defined as the energy of the event hits minus the EM shower energy.

5.2 Philosophy of Energy Estimator

A function is needed to map the two observable variables (E_{EM} and E_{HAD}) to an estimator (E_{reco}) of the true energy. The function is in the form of $E_{reco} = aE_{EM} + bE_{HAD} + cE_{EM}^2 + dE_{HAD}^2$, where a, b, c, and d are the parameters. To get the fitted parameters, a chi-square fit is performed on the reweighted MC sample, which is reweighted by the "flattening weight" (described below.) With the flattening weight applied, the reweighted MC sample has a flat distribution in true energy. Thus, the chi-square fitting result is not biased anymore by the high statistics at the energy peak, as it was in the previous analyses. In this section, the details of the flattening weight and chi-square fit for the energy estimator are discussed.

Based on the original true energy distribution (Figure 5.1), which has a peak

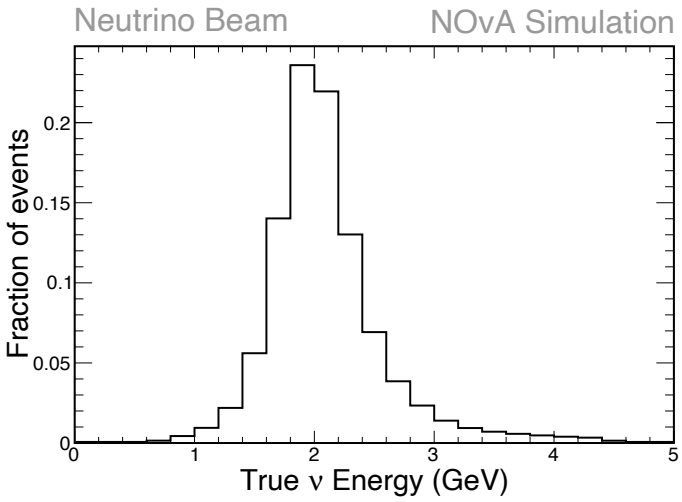

Figure 5.1. True neutrino energy distribution of selected FD MC events

around 2 GeV and small tails with very few events in the high and low energy ranges, the flattening weight is defined as $w_i = \frac{1}{n_i}$, where n_i represents the number of events in bin i; w_i represents the flattening weight for events in the energy range of bin i. There are 25 bins evenly distributed in the range 0–5 GeV. The bin width is 0.2 GeV. The energy range of the i^{th} bin is $(0.2(i-1),\, 0.2i)$ GeV. All the events in the energy range of bin i share the same weight w_i.

The chi-square fit is performed based on a 2D plot as shown in Figure 5.2. Each bin of the 2D plot is filled by the weighted average true energy value, which is defined by

$$\bar{E}_{\text{true}}(x, y) = \sum_{i=1}^{n} w_i E^i_{\text{true}}\,, \tag{5.2}$$

where n represents the number of events whose EM energy (x) and HAD energy (y) are within the energy range of bin (x, y); w_i is the flattening weight of event i; E^i_{true} is the true neutrino energy of event i. The empty bins in the 2D plot are excluded

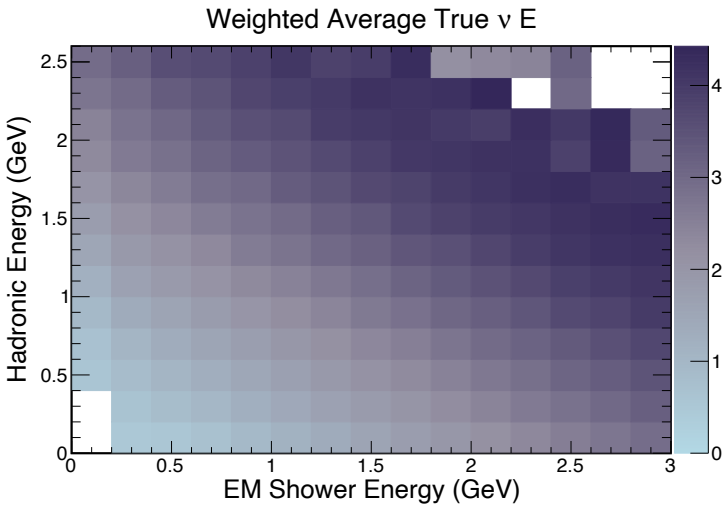

Figure 5.2. Hadronic energy vs. reconstructed electromagnetic energy distribution with color representing weighted average true neutrino energy in GeV

from the fit.[7] The chi-square (χ^2) is defined by

$$\chi^2 = \sum_{(x,y)}^{\text{bins}} \frac{(\bar{E}_{\text{true}}(x,y) - E_{reco}(x,y|a,b,c,d))^2}{\sigma^2(x,y)}\,, \tag{5.3}$$

where the summation acts on all the bins that are used in the fit; $\bar{E}_{\text{true}}(x,y)$ is the weighted average true energy of bin (x,y); E_{reco} is the fitting function of the energy estimator ($E_{reco} = aE_{EM} + bE_{HAD} + cE_{EM}^2 + dE_{HAD}^2$) where a, b, c, and d are fitting parameters optimized by minimizing the total chi-square value; and $\sigma^2(x,y)$ represents the error of bin (x,y), which is defined as

$$\sigma^2(x,y) = \frac{\sum_{j=1}^{n}(w_j E_{\text{true}}^j(x,y))^2}{\sum_{j=1}^{n} w_j}\,. \tag{5.4}$$

The summation acts on all the n events whose EM energy and HAD energy fall into bin (x,y) of the 2D plot. The $E_{\text{true}}^j(x,y)$ is the true neutrino energy of event j, and

[7]Some bins with abnormal color compared to the adjacent bins are also excluded in the fit. Only the area with smooth gradient color along both x and y directions is used for the fit: $x \in (0.4, 2.4)$ GeV and $y \in (0, 1.4)$ GeV.

w_j is the corresponding flattening weight.

Without the flattening weight applied, the default error used by ROOT in a chi-square fit is defined by

$$\sigma^2(x,y) = \frac{1}{n}\sum_{j=1}^{n}(E^j_{\text{true}}(x,y))^2\,, \tag{5.5}$$

which is very small for large n at the energy peak. A small $\sigma^2(x,y)$ value in the denominator of Equation 5.3 leads to a large weight in the chi-square fit, which means the energy bins with higher statistics are more influential in the fitting. Ideally, the energy estimator should not be biased towards the expected beam energy peak. Before I invented this correction using the flattening weight, the estimator was able to get only the events at the peak estimated correctly. Now, the MC sample is reweighted and the bias and energy dependence from the spectral shape of the true energy are removed.

5.3 Result and Discussion

In the $\bar{\nu}_e$ analysis, a similar technique is used to reconstruct the electron antineutrino energy for the $\bar{\nu}_\mu \rightarrow \bar{\nu}_e$ signal events in the FD. Both ν_e and $\bar{\nu}_e$ energy estimators have the form: $E_{reco} = s(aE_{EM} + bE_{HAD} + cE^2_{EM} + dE^2_{HAD})$, where s is the scaling factor. The scaling factor makes sure that the fractional energy reconstruction error, which is defined by

$$\text{Frac. Error} = \frac{E_{reco} - E_{\text{true}}}{E_{\text{true}}}, \tag{5.6}$$

has a distribution with a mean of zero, as shown in Figure 5.3. The root mean square (RMS) value represents the standard deviation (σ) and is used as the energy resolution of the energy estimator. The result parameters (a, b, c, d, and s) and the

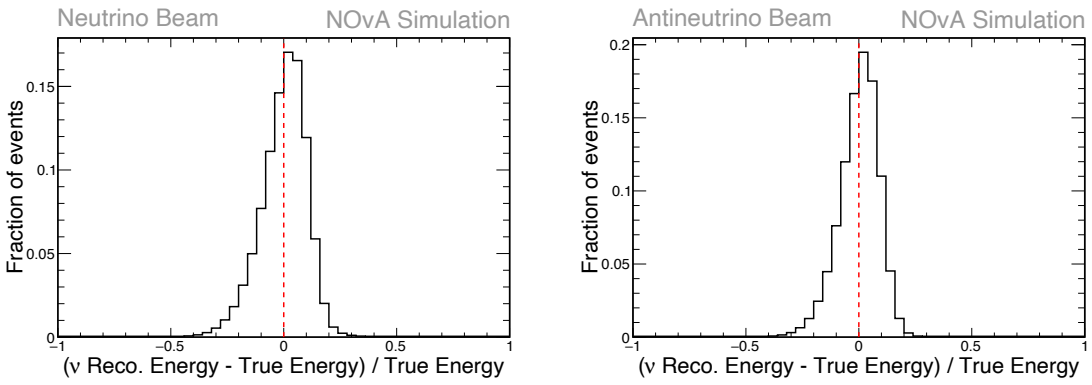

(a) FHC energy estimator

(b) RHC energy estimator

Figure 5.3. Distributions of fractional energy reconstruction error with mean value of 0 and RMS value of 0.103 (0.091) for FHC (RHC) energy estimator

Table 5.1. Chi-square Fit Results

	a	b	c	d	s
FHC	1.02($\pm$3.24)	1.11($\pm$3.79)	1.44×10^{-3}($\pm$1.90)	1.10×10^{-1}($\pm$2.63)	$\frac{1}{1.036}$
RHC	0.99($\pm$0.22)	1.20($\pm$0.40)	1.93×10^{-7}($\pm$7.64)	1.21×10^{-7}($\pm$7.33)	$\frac{1}{1.011}$

corresponding uncertainties for the ν_e and $\bar{\nu}_e$ energy estimators are listed in Table 5.1.

The fractional energy reconstruction error vs. true neutrino energy distribution is used to demonstrate the performance of the energy estimators. To better understand the bias, independent from the spectral shape of the true neutrino energy, the flattening weight is applied. An even, straight, and smooth distribution without pronounced deviations along the x-axis is preferred. In Figure 5.4, our energy estimators mostly have uniformly distributed biases along true energy as expected. There is some bias, especially at low energy. Taking the FHC energy estimator as an example, the bias in the low energy range is positive, which means the reconstructed neutrino energy is overestimated. To understand where the biases come from, studies of the energy estimator in the different neutrino interaction modes are performed.

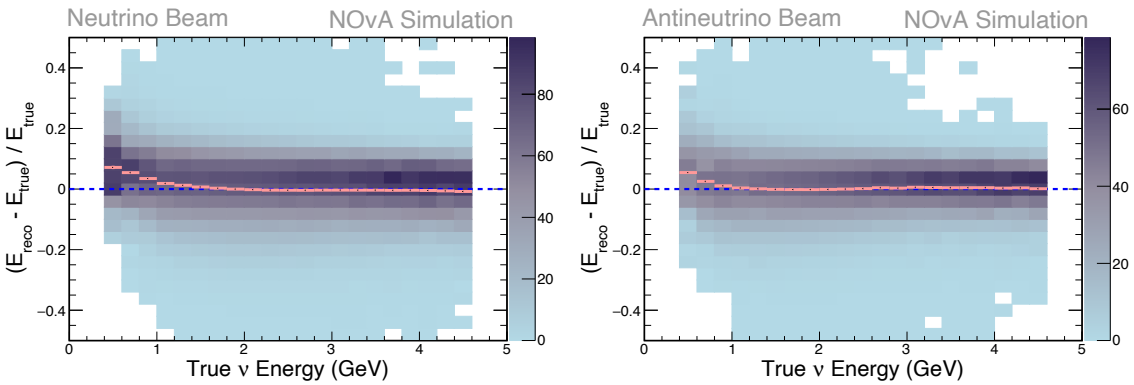

(a) FHC energy estimator (b) RHC energy estimator

Figure 5.4. Fractional energy reconstruction error along true neutrino energy distributions with flattening weight applied and pink dashes showing the bias along true energy

5.4 Interaction Modes

There are five major neutrino interaction modes considered in the NOvA neutrino cross-section model: quasi-elastic (QE), resonant (RES), deep inelastic scattering (DIS), coherent (COH), and meson-exchange current (MEC). The outgoing particles in these interaction modes are different, and the reconstructed variables, such as prong particle IDs and prong energies, are affected by the interaction modes. These differences in reconstruction lead to differences in the reconstructed electromagnetic shower and hadronic energies, which are the input variables of neutrino energy. To have a better understanding of how the neutrino energy is affected, the MC sample is broken down by interaction mode. The proportions of each type of interaction are listed in Table 5.2, and the corresponding fractional energy reconstruction error distributions are plotted in Figure 5.5. The ν_e energy estimator is used to illustrate the correlation between the bias and the interaction modes in the following discussion.

In Figure 5.5, it is obvious that the QE and MEC components have positive mean values, which mean overall overestimates. The DIS component is centered at zero, but it still affects the fit. The remaining components have negative mean

Table 5.2. Composition of FD ν_e Signal Sample by Interaction Mode

	QE	RES	DIS	MEC	COH
FHC	30.1%	45.2%	15.4%	8.6%	0.71%
RHC	40.6%	35.4%	11.1%	11.3%	1.54%

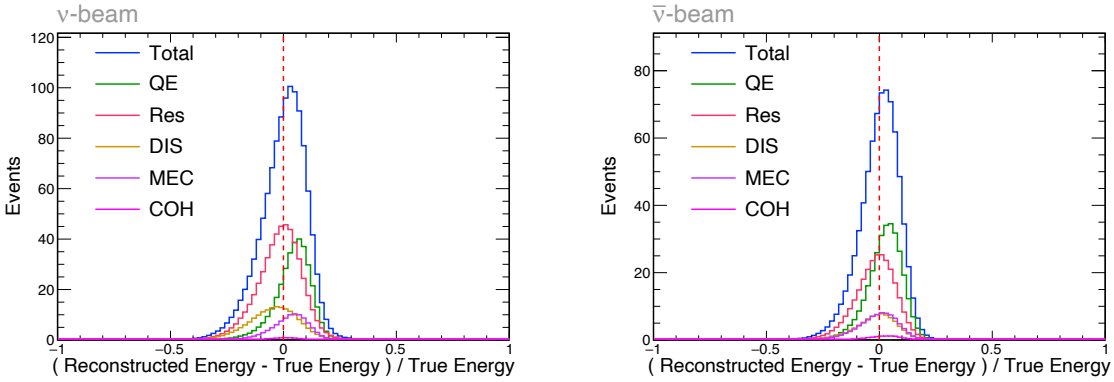

(a) FHC energy estimator

(b) RHC energy estimator

Figure 5.5. Fractional energy reconstruction error distributions broken down by interaction mode

values, corresponding to overall underestimates. The fit is made with the energy-reconstruction plot with the flattening weight applied (Figure 5.2), where the color represents the weighted average true energy in each bin. Figure 5.6 shows the 2D event distributions of EM shower energy vs. hadronic energy by interaction mode. These plots also have the flattening weight applied. The color represents the number of events. Comparing these 2D event distribution plots for different interaction modes can give us a hint to the reason for the over- and underestimates.

In Figure 5.2, the lower left corner corresponds to a low weighted average true neutrino energy. Comparing to the 2D plots in Figure 5.6, we see that the lower left corner is dominated by QE and MEC interactions while RES and DIS interactions dominate the region with high weighted average true neutrino energy. The contribution of COH interaction is small due to the low statistics, even if it is in the high energy region. In Table 5.2, we see that the top two components of the

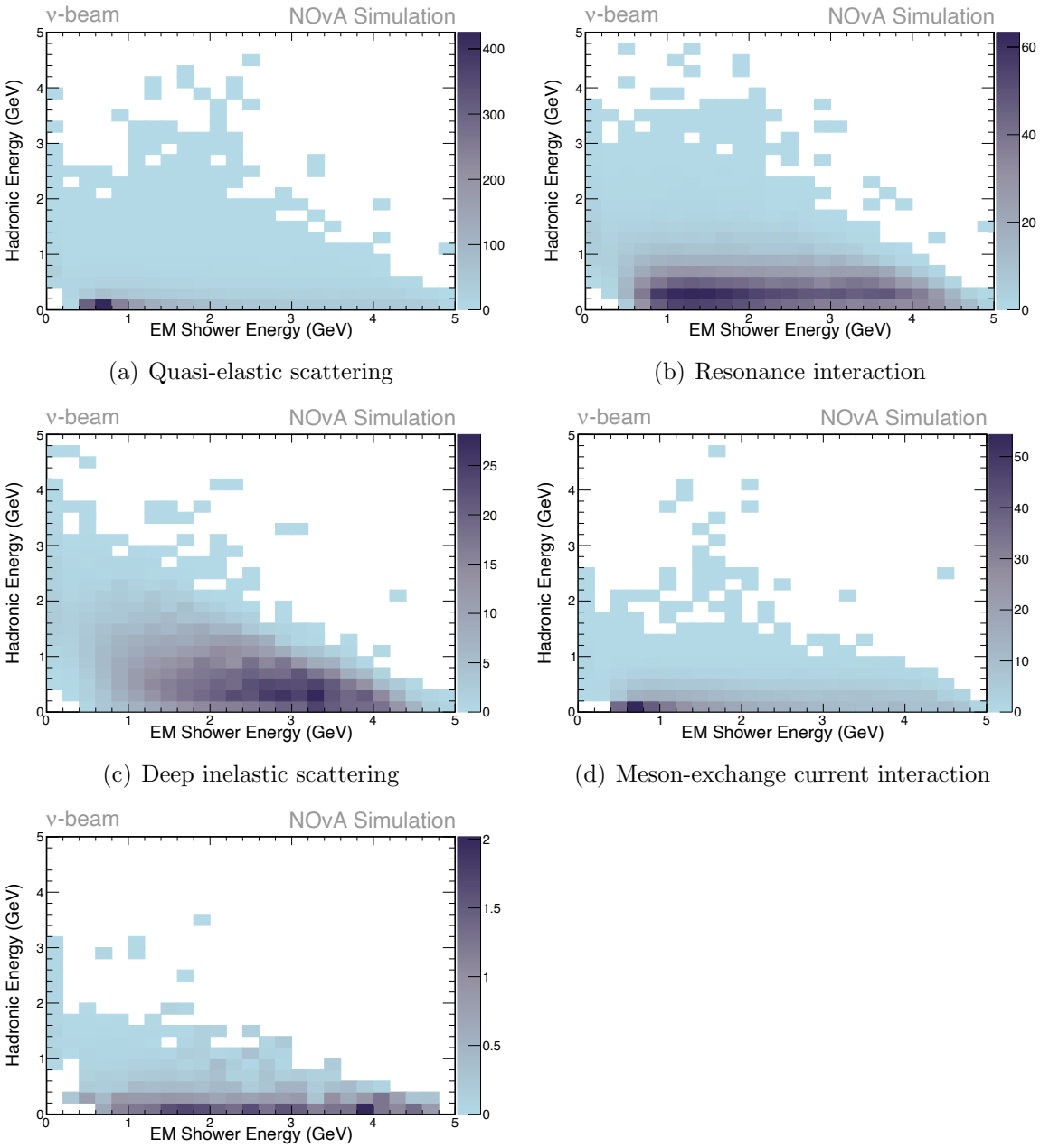

(a) Quasi-elastic scattering

(b) Resonance interaction

(c) Deep inelastic scattering

(d) Meson-exchange current interaction

(e) Coherent scattering

Figure 5.6. Distributions of hadronic energy vs. EM shower energy broken down by interaction mode with flattening weight applied and color representing number of events

selected FD signal sample are the QE and RES interactions. Based on the results in Figure 5.5, the mean energy of QE events is overestimated. In contrast, the RES events have an underestimated mean energy. Hence, there is a tension between these

two components in energy reconstruction. When the fit is performed, the regions dominated by QE and RES interactions impose different effects on the coefficients of the fitting function. In a QE scattering process, a neutrino interacts with a nucleon via a QE collision with total kinetic energy conserved. The outgoing particles usually can be well reconstructed and classified as EM showers or hadronic particles. However, in a RES interaction, the situation is more complicated. The target nucleon is struck by the neutrino, producing a baryonic resonance whose identity depends on the incident neutrino's energy. The baryonic resonance decays back to a nucleon accompanied by some other particles—most often a single-pion. The detector cell is 6 cm by 3.87 cm, only great for long track measurement. A typical pion in the NOvA detectors has a track approximately 5 cells in length and may decay into a muon and a neutrino, or interact in the detectors. So it is hard to reconstruct pions and their decay products as final-state particles in the first place. The more numerous the final-state particles are, the harder it is to reconstruct them. One possible reason for the underestimate of the neutrino energy in inelastic scattering events is that some particles with very short track lengths are not successfully reconstructed. In this case, the total energy of the outgoing particles is underestimated.

As shown in Figure 5.6, resonance and deep inelastic interactions dominate the high energy regions. When performing the fit over all the events, the fitting parameters are more affected by the dominating events in the high true-neutrino-energy region, where, as just explained, the outgoing particle energy is underestimated. To compensate for the underestimated input variables, the fit prefers large parameter values. Consequently, in the low true-neutrino-energy region, the energy of the QE and MEC events are overestimated when the same set of parameters is applied. In Figure 5.7, the fractional energy reconstruction error vs. true neutrino energy distribution of the ν_e estimator is broken down by interaction mode. The flattening weight is applied in each plot. The over- and underestimates are clear in these plots, and we

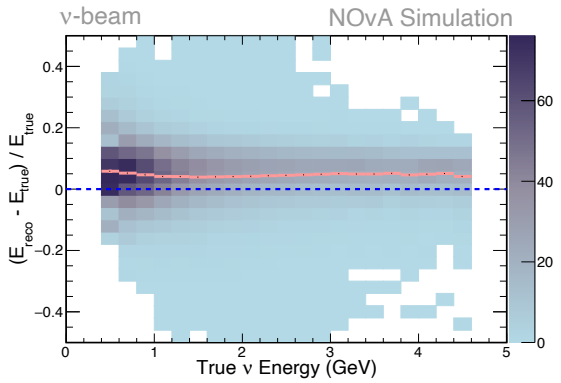

(a) Quasi-elastic scattering.

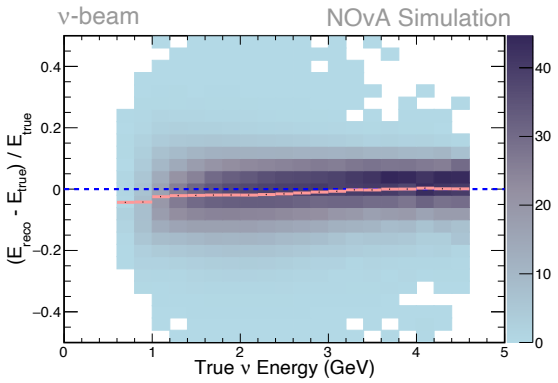

(b) Resonance interaction.

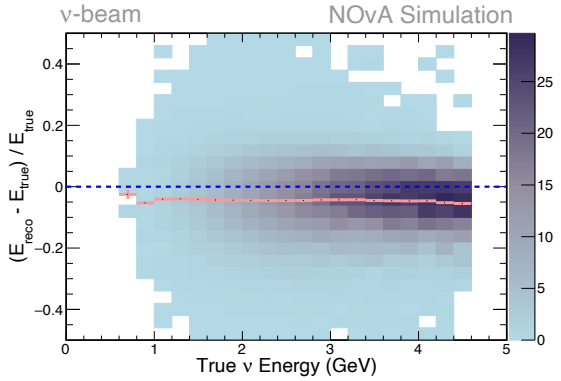

(c) Deep inelastic scattering.

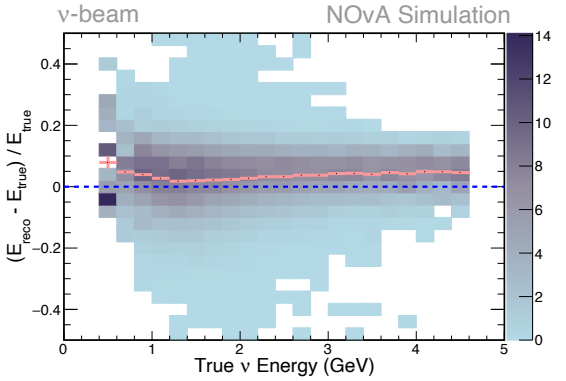

(d) Meson exchange current interaction.

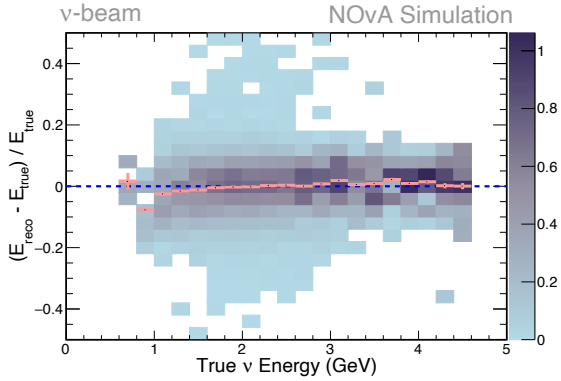

(e) Coherent scattering.

Figure 5.7. Fractional energy reconstruction error along true neutrino energy distributions broken down by interaction mode with flattening weight applied and pink dashes showing the bias along true energy

see an almost flat bias along true neutrino energy in each interaction mode.

The energy estimators for both ν_e and $\bar{\nu}_e$ analyses are improved by removing the dependence on the true energy spectral shape. The final-state particle classifica-

tion CNN is here employed in the energy reconstruction, which has never been done before. With these improvements, the electron (anti)neutrino energy is better reconstructed so that the systematic uncertainties are reduced in the oscillation analysis, which is discussed in the next chapter.

CHAPTER 6

OSCILLATION ANALYSIS

The primary goal of the NOvA experiment is to measure the oscillation probabilities. The oscillation analysis makes use of most studies described in the previous chapters to investigate neutrino oscillations via four channels: the ν_μ disappearance ($\nu_\mu \to \nu_\mu$) and ν_e appearance ($\nu_\mu \to \nu_e$) channels, and their corresponding antineutrino oscillation channels. The antineutrino oscillation analyses are based on analysis techniques similar to those developed in the neutrino analyses. Hence, the neutrino analyses are used as examples to illustrate the techniques.

Selection methods and binning rules applied in the ν_μ and ν_e analyses are different from each other. Both binning methods are optimized to separate the better-reconstructed signal events from the rest and let them occupy more bins, which correspond to more weight in the final bin-by-bin likelihood oscillation fit. Both the ND and FD data samples are used to extract information on neutrino properties and neutrino fluxes. In the ν_μ analysis, the ND data are used to study the ν_μ flux before significant oscillation, and the FD data are used to study the ν_μ disappearance signal, which is dominated by ν_μ events and has negligible background events. In the ν_e analysis, the FD data are used to study the ν_e appearance signal, and the ND data are used for two purposes. One is to study the ν_μ flux before significant oscillation, which is the same as that of the ν_μ analysis. The other is to study the background to the ν_e appearance signal. Since ν_e appearance is less likely to occur than ν_μ disappearance, the ν_e appearance samples are low-statistics compared to the ν_μ disappearance samples. With a well-understood oscillation background, we can be more confident in the oscillation signal measurement. Hence, the oscillation background estimation is critical to the ν_e analysis.

The background is due to the inefficiency of selection and imperfection of

the MC simulation, and can be constrained by using the two functionally identical detectors. Similarly to what is done at the FD, ν_e selections and binning methods are applied at the ND to study the discrepancy between data and MC. If we are able to understand the discrepancy and correct the MC at the ND, then we can apply the same correction to the FD MC. Decomposition, a data-driven technique, is applied for a better agreement between the selected MC and data samples. It adjusts the proportions of the MC components (ν_μ CC, ν_e CC, and NC interactions) in the selected ND ν_e background sample. It also corrects the selected ND ν_μ MC sample. The corrections applied to reweight the ND MC samples are also applied to the FD selected MC samples. The correction of each MC component is propagated independently from the ND to the FD. The propagation is handled by a technique called near-to-far extrapolation. The near-to-far extrapolation cancels out some types of systematic uncertainties by taking advantage of the functionally identical detector designs.

All these techniques contribute to the oscillation parameter extraction and analysis systematic uncertainty estimation. The decomposition techniques, near-to-far extrapolation, oscillation parameter extraction and systematic uncertainty estimation are discussed in detail later in this chapter. The ν_μ and $\bar{\nu}_\mu$ disappearance analyses are introduced first, followed by the ν_e and $\bar{\nu}_e$ appearance analyses. At the end of the chapter, the joint analysis of the oscillation parameters, θ_{23}, Δm^2_{32}, and δ_{CP}, combining all four channels, is discussed.

6.1 Disappearance Analysis

The $\overset{(-)}{\nu}_\mu$ disappearance analysis provides strong constraints on the atmospheric parameters $\sin^2\theta_{23}$ and Δm^2_{32}. Figure 6.1 [9] shows an example of a selected ν_μ candidate in the FD. The analysis techniques are shared between the ν_μ and $\bar{\nu}_\mu$ analyses. The ν_μ analysis is used to illustrate the analysis techniques. Where the $\bar{\nu}_\mu$

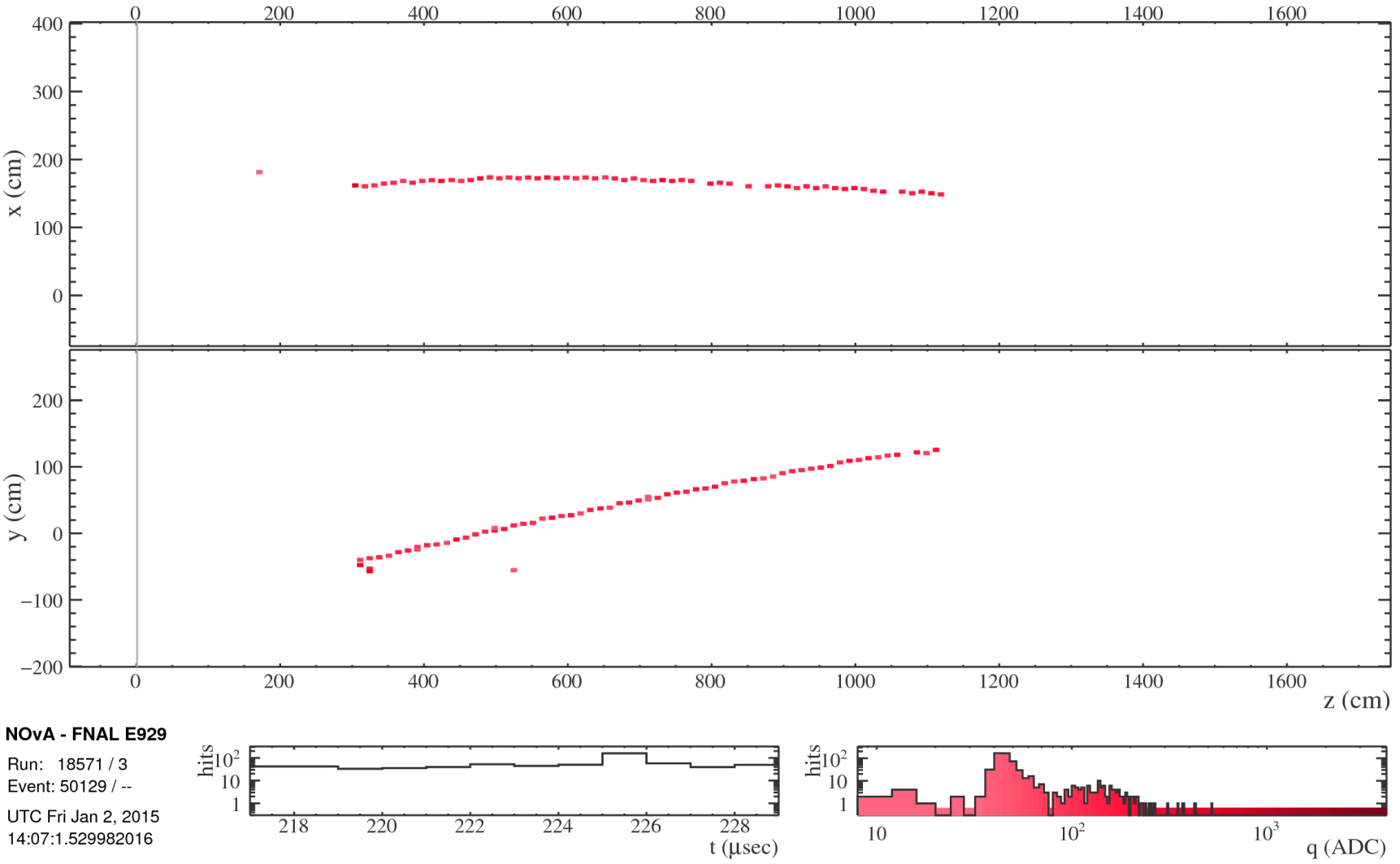

Figure 6.1. Event display of a real data ν_μ candidate in the FD

analysis employs some different techniques, the differences are pointed out.

6.1.1 Analysis Selection. The ν_μ analysis selection includes three major components: basic quality, detector containment, and incident particle identification (PID).

The basic quality selection ensures that the basic reconstructed objects are present so that the reconstructed variables can be used in the analysis. The basic quality selection has the following requirements: an interaction vertex is reconstructed in the event; at least 20 hits are observed in the event; at least one 3D Kalman track, along with the ReMId value, is found in the event; and activity is present in four contiguous detector planes so that the event is not fully vertical.

The containment selection requires that neutrinos interact and have their energies deposited entirely within the detector. Events that pass the containment selection always maintain a distance from the detector walls: at least 60 cm to the top; 12 cm to the bottom or west wall; 16 cm to the east wall; and 18 cm to the front or back wall. An event is rejected if any of its track end points is too close (fewer than 6 cells) to the detector walls or if any of its hits is too close to the walls: fewer than 2 cells from the front wall or 3 cells from the back wall.

The PID selection is based on two components: the event CNN, which is designed for neutrino interaction classification [36], and the ReMId score. The event CNN predicts three probabilities, which add up to 1, for an incident particle to be ν_e, ν_μ, or ν_τ. The ν_μ PID selection requires the predicted probability of an event being a ν_μ interaction to be greater than 0.8 (CNN ν_μ ID > 0.8). It also requires the highest ReMId score among those of all the tracks in the event to be greater than 0.3 to ensure a clear muon track is present.

In addition to the selections listed above, a cosmic rejecting selection is trained and applied to the FD samples. It employs the cosmic-rejection Boosted Decision Tree

(BDT) technique [37] to classify events. The result of the cosmic-rejection BDT is the probability of an event being oscillation signal-like. The ν_μ and $\bar{\nu}_\mu$ analyses have their cosmic-rejection BDTs trained separately and they both require a cosmic-rejection BDT score greater than 0.53.

At the ND, the basic quality selection and the PID selection are identical to the ones applied at the FD. The ND containment selection is slightly different because of the volume and geometry differences of the detectors. Other than requiring the events to be fully contained in the ND, it also requires: any showers in the ND to have the x and y coordinates of their starting and ending points within -180–$+180$ cm, and the z coordinates within 40–1525 cm. Only the primary muon track in an event is allowed to extend into the muon-catcher ($z > 1275$ cm). All vertices of the events must be located within the ND excluding the muon-catcher ($z < 1100$ cm).

6.1.2 Energy Reconstruction and Binning Methods. The oscillation parameter extraction, so-called oscillation fit, is performed based on the binned distributions of the FD selected samples. The binning methods directly affect the measurement sensitivity of the oscillation parameters. The ν_μ analysis binning method consists of two parts, which are both based on the reconstructed ν_μ energy.

The ν_μ samples are binned in reconstructed ν_μ energy with non-constant bin width, and divided into four subsamples, each having different energy resolution. With these two methods, the high energy resolution events occupy more bins, and thus have more weight in the oscillation fit, which is a bin-by-bin fit. The resolution of the ν_μ energy estimator is critical to the sensitivity of the oscillation analysis and is discussed first, followed by the two binning methods.

In the NOvA detectors, a typical ν_μ CC interaction consists of a long clear muon track and a hadronic shower (see, for example, Figure 6.1). The ν_μ energy

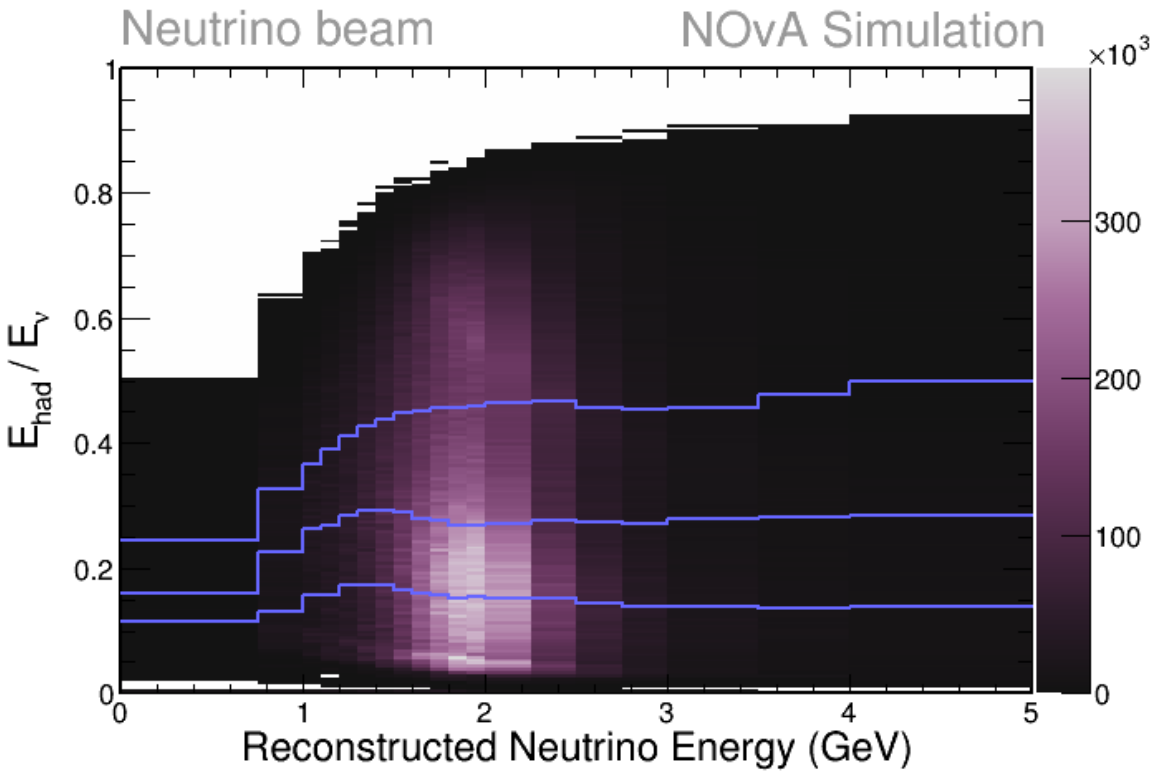

Figure 6.2. Hadronic fraction vs. reconstructed neutrino energy spectrum of unoscillated FD selected ν_μ MC sample divided by blue curves into four quartiles with color representing number of events

is reconstructed as the sum of the outgoing muon energy and the hadronic shower energy [38]. The muon energy is estimated from the muon track length. In a ν_μ CC event, most of the energy goes to the muon. The hadronic showers may consist of various types of low energy hadrons and are more difficult to reconstruct compared to the long clear muon track. The ability to reconstruct the hadronic showers of ν_μ candidates limits the performance of the ν_μ energy estimator. Hence, we bin the ν_μ candidates by their energy resolutions. In this way, the events are divided into four subsamples, called quartiles, by hadronic energy fraction, which is the ratio of hadronic energy to ν_μ energy. Each quartile consists of 25% of the events in the sample. The energy resolution bins are based on a 2D spectrum, as in Figure 6.2 [9]. The mean and resolution values of the reconstructed energy for the four quartiles are

Table 6.1. Fractional Mean and Resolution Values

Quartile	Mean	Resolution
1	0.016	0.078
2	-0.004	0.092
3	-0.014	0.104
4	-0.054	0.115

listed in Table 6.1 [19], and the sample in the fourth quartile has the worst energy resolution.

In addition to energy resolution quartiles, non-constant bin widths are employed for the reconstructed energy spectra. So the energy bins around the oscillation maximum (around 1.8 GeV) are narrower, while the bins in the vicinity of the low and high energy tails are wider. There are 19 bins in each quartile, with their edges located at: 0, 0.75, 1, 1.1, 1.2, 1.3, 1.4, 1.5, 1.6, 1.7, 1.8, 1.9, 2, 2.25, 2.5, 2.75, 3, 3.5, 4, and 5 GeV. The energy bins are optimized for the sensitivity of the oscillation parameter extraction [39]. Figure 6.3 [9] shows the ND selected data and MC samples in ν_μ analysis bins.

6.1.3 Corrections with ND Data. In the NOvA cross section tuning studies [40], the neutrino interaction rates are adjusted such that the reweighted MC simulation better matches the data. However, the MC simulation is still not perfect in describing the observed data. In addition, the ν_μ PID selection, which aims to select ν_μ CC-like events, is trained and optimized using simulated samples. Its performance on real data is also not perfect and unknown, since there is no way to know the truth about real data. We assume that the discrepancy between the selected data and MC samples is because of the imperfections of the simulation and selection. Decomposition and extrapolation techniques are employed to improve the predicted MC sample at the FD. We use the ND selected data and MC samples to correct the ND MC components

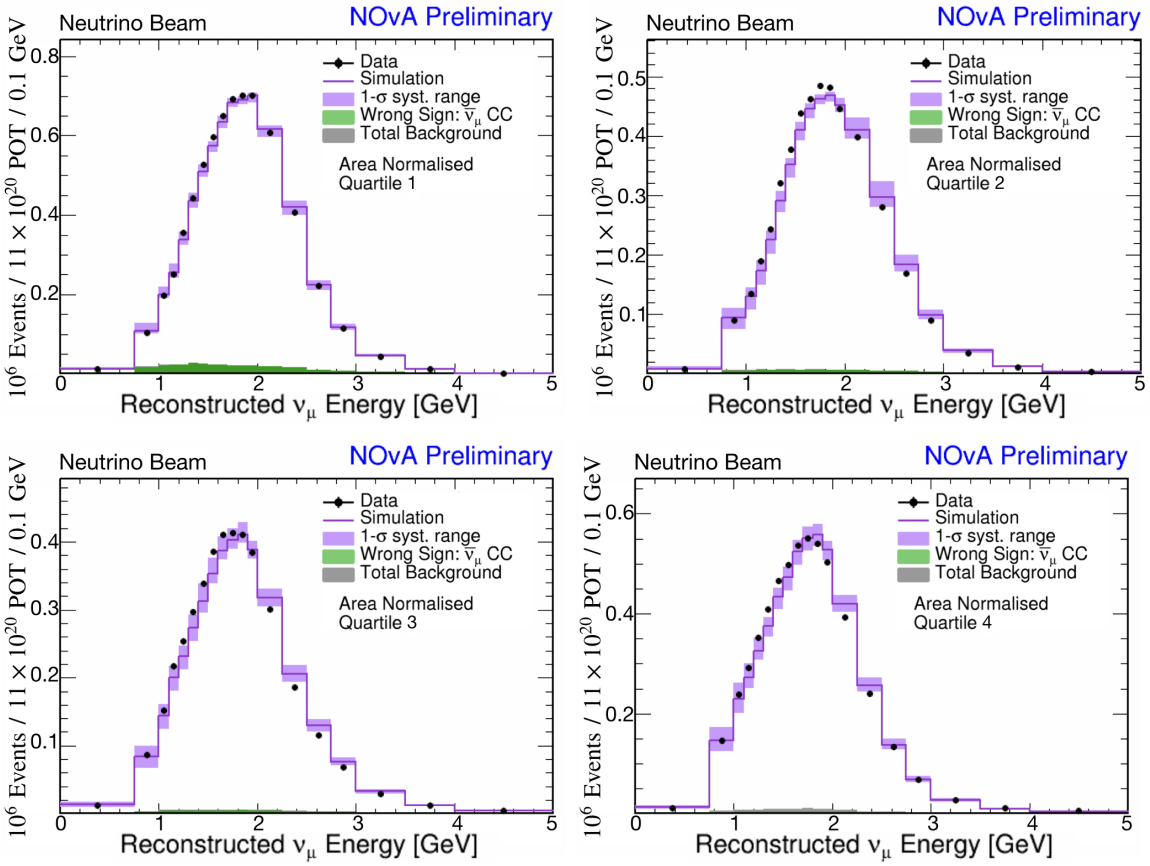

Figure 6.3. Distributions of the ND selected ν_μ data and MC samples in ν_μ analysis bins with MC normalized to the areas of data distributions to show their shapes

(decomposition). The correction is made by reweighting the MC components in the ND selected MC samples to match the data samples. Then, the weights are propagated component-by-component to the corresponding FD MC components in the FD predicted MC sample (extrapolation). There is a different weight in each neutrino energy bin.

In both ν_μ and $\bar{\nu}_\mu$ analyses, only the ν_μ and $\bar{\nu}_\mu$ components are corrected by decomposition and extrapolation. The reasons for not correcting the remaining MC components in the selected ν_μ MC samples are as follows: the proportions of ν_μ CC-like ν_e and NC background events, that are misidentified by the PID as ν_μ signal candidates, are tiny in the selected ν_μ samples at both detectors; and the ν_μ

disappearance oscillation fit counts the difference of the ν_μ signal between the FD and ND, where the background events misidentified by the same PID have similar features, thus cancel and do not contribute to the fit. The reasons that we do not ignore the $\bar{\nu}_\mu$ background component, but do correct it along with the ν_μ signal to match the data, are as follows: the wrong-sign component ($\bar{\nu}_\mu$) is the largest background, as shown in Figure 6.3; and it also "disappears," so we cannot ignore it as we do the other backgrounds. Besides, to the PID classifiers, $\bar{\nu}_\mu$ is more ν_μ-like than the other backgrounds.

6.1.3.1 Decomposition. In the decomposition stage, the corrections are calculated using the ND selected data and MC samples, where the applied PID selection is the same as that at the FD. The bin-by-bin corrections are based on the ν_μ analysis bins, including four quartiles and reconstructed ν_μ energy non-constant bin widths. By assuming that any data/MC discrepancy is due to the ν_μ and $\bar{\nu}_\mu$ components, in each quartile, the discrepancy is split according to the ratio of the ν_μ and $\bar{\nu}_\mu$ components in the selected ND MC sample to correct the number of ν MC events by

$$\mathrm{MC}_\nu^{\mathrm{corr.}}(i) = (\mathrm{data}(i) - MC_{\mathrm{others}}(i)) \times \frac{MC_\nu(i)}{MC_{\bar{\nu}_\mu}(i) + MC_{\nu_\mu}(i)}\,, \tag{6.1}$$

where $\nu = \{\nu_\mu, \bar{\nu}_\mu\}$; $\mathrm{MC}_\nu^{\mathrm{corr.}}(i)$ represents the number of corrected $\overset{(-)}{\nu}_\mu$ MC events in bin i; $\mathrm{data}(i)$ is the number of selected data candidates in bin i; $\mathrm{MC}_\nu(i)$ represents the number of original selected $\overset{(-)}{\nu}_\mu$ MC events in bin i; and $\mathrm{MC}_{\mathrm{others}}(i)$ is the number of original selected MC events in bin i, including all the MC components except for ν_μ and $\bar{\nu}_\mu$. With Equation 6.1, we get the corrected ND MC components in ν_μ analysis bins. The decomposition weights are 1D ratios in bins of ν_μ energy, where the ratios of corrected and original $\bar{\nu}_\mu$ number of events are defined by

$$w_\nu(i) = \frac{\mathrm{MC}_\nu^{\mathrm{corr.}}(i)}{\mathrm{MC}_\nu(i)}\,, \tag{6.2}$$

where $\nu = \{\nu_\mu, \bar{\nu}_\mu\}$, and $w_\nu(i)$ represents the ratio of corrected ($\mathrm{MC}_\nu^{\mathrm{corr.}}(i)$) and uncorrected ($\mathrm{MC}_\nu(i)$) ν MC event numbers in bin i.

6.1.3.2 Extrapolation. The corrections are then propagated to the FD ν_μ and $\bar{\nu}_\mu$ components. This propagation is called near-to-far extrapolation. There are two ways to extrapolate. One way is to save and propagate the decomposition weights as a function of true neutrino energy. This is called true-extrapolation. Another way, called reco-extrapolation, is to save and propagate the correction weights as a function of the reconstructed neutrino energy. When the ND and FD MC oscillation signal events are different in flavor, energy reconstruction, or binning method, we have to use the true-extrapolation, such as for ν_e and $\bar{\nu}_e$ appearance signal events. In addition, the true-extrapolation is used when the oscillation parameters are sensitive to the resolution of reconstructed neutrino energy and bins, such as for ν_μ and $\bar{\nu}_\mu$ disappearance signal events. The reco-extrapolation is used only in the ν_e analysis to extrapolate the oscillation backgrounds, which is discussed below in Section 6.2.

The cartoon in Figure 6.4 shows the fourth quartile of the ND selected ν_μ samples. It is used as an example to illustrate how the decomposition weights of the MC ν_μ components are propagated to the FD. The $\nu_\mu \to \nu_\mu$ events are used in the cartoon, and the oscillation probability,[8] which is a function of the true ν_μ energy, is applied to the FD MC to predict the oscillated ν_μ signal.

In Figure 6.4, the top left plot shows the original reconstructed ν_μ energy distributions of the ND selected data and MC samples. The ND reco-to-true and FD true-to-reco matrices are both 2D spectra of reconstructed (x-axis) vs. true (y-axis) ν_μ energy, and the different names reveal the different usages. At the ND, the decomposition weights calculated from Equation 6.2 are used to reweight the

[8]The oscillation parameters are from the NOvA 2018 analysis results [35].

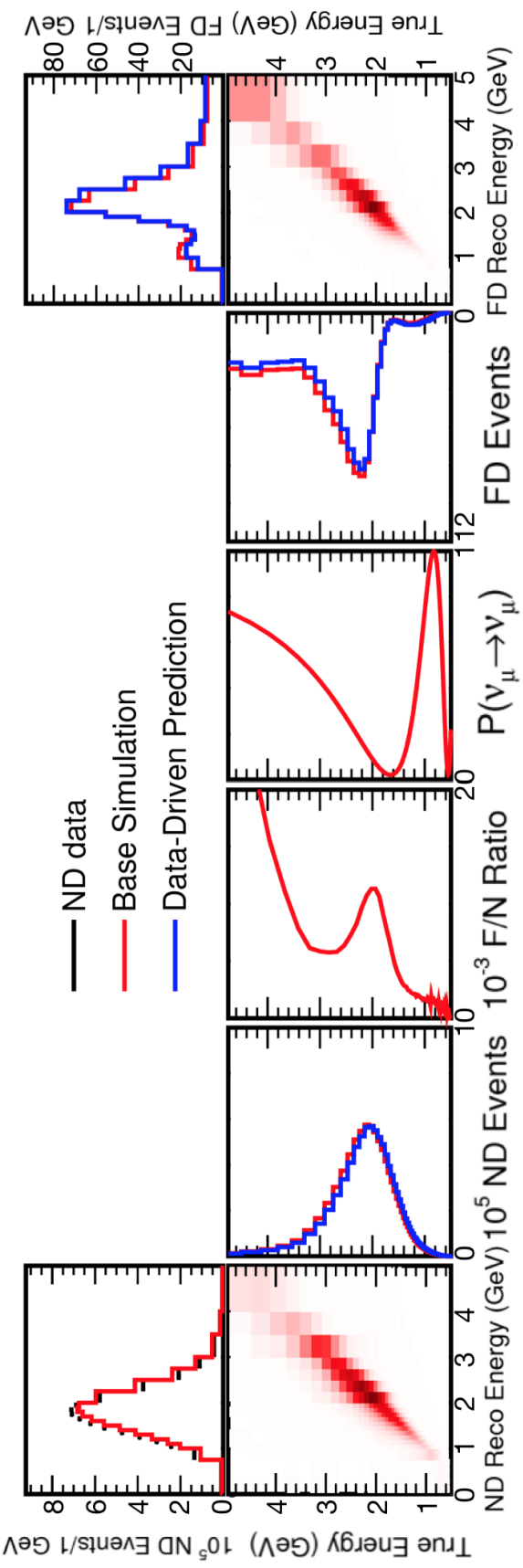

Figure 6.4. Near-to-far extrapolation cartoon for the ν_μ analysis with red (blue) curves representing the original (decomposition-corrected) MC samples; top left plot showing the reconstructed ν_μ energy distributions of the ND selected data (black) and MC samples; top right plot showing the FD predicted MC samples; and bottom plots from left to right showing ND reco-to-true matrix, ND true ν_μ energy, ratio of true ν_μ energies at FD and ND, ν_μ disappearance probability curve, FD true ν_μ energy, and FD true-to-reco matrix

ν_μ events by their reconstructed energy values in the ND reco-to-true matrix. The reweighted and original ND reco-to-true matrices are projected onto the y-axis for the 1D true ν_μ energy distributions (bottom second plot in Figure 6.4). The 1D ratio of the reweighted and original true ν_μ energy distributions, in true ν_μ energy bins, is then used to reweight the true ν_μ events in the FD true-to-reco matrix by using their true ν_μ energy values. Until this point, the near-to-far true-extrapolation is applied. In the FD true-to-reco matrix, the oscillation probabilities are calculated using the true ν_μ energies of the events and applied to reweight the events. Finally, the y-projection of the reweighted FD true-to-reco matrix gives us the predicted ν_μ disappearance distribution in bins of reconstructed ν_μ energy.

Another extrapolation technique is employed to correct for the selection efficiency and acceptance differences of the two detectors. The ND is closer to the target, while the FD is farther away. Both detectors are off-axis. Hence, the neutrino beam source (the target) is point-like to the FD but not to the ND. The FD sees a narrower flux, and the ND sees a wider and more spread neutrino flux, in energy, due to its being closer to the target. The neutrinos detected in the two detectors are thus different in kinematics in the first place. Besides, the PID selections applied at both detectors are trained on the FD MC files, which makes them tend to select events that look more FD-like in their kinematics. These kinematic differences lead to sensitivities to systematic uncertainties in the oscillation analysis.

An additional binning method in the near-to-far extrapolation is employed, called p_t extrapolation [41]. To correct for the kinematic differences of neutrinos at the two detectors, additional quantiles ($\vec{p}_t$-quantiles) in each energy resolution quartile are used based on a kinematic variable: the transverse momentum ($|\vec{p}_t|$) of the outgoing lepton in the selected neutrino interactions, which is sensitive to the kinematic differences between the two detectors due to selection efficiency and

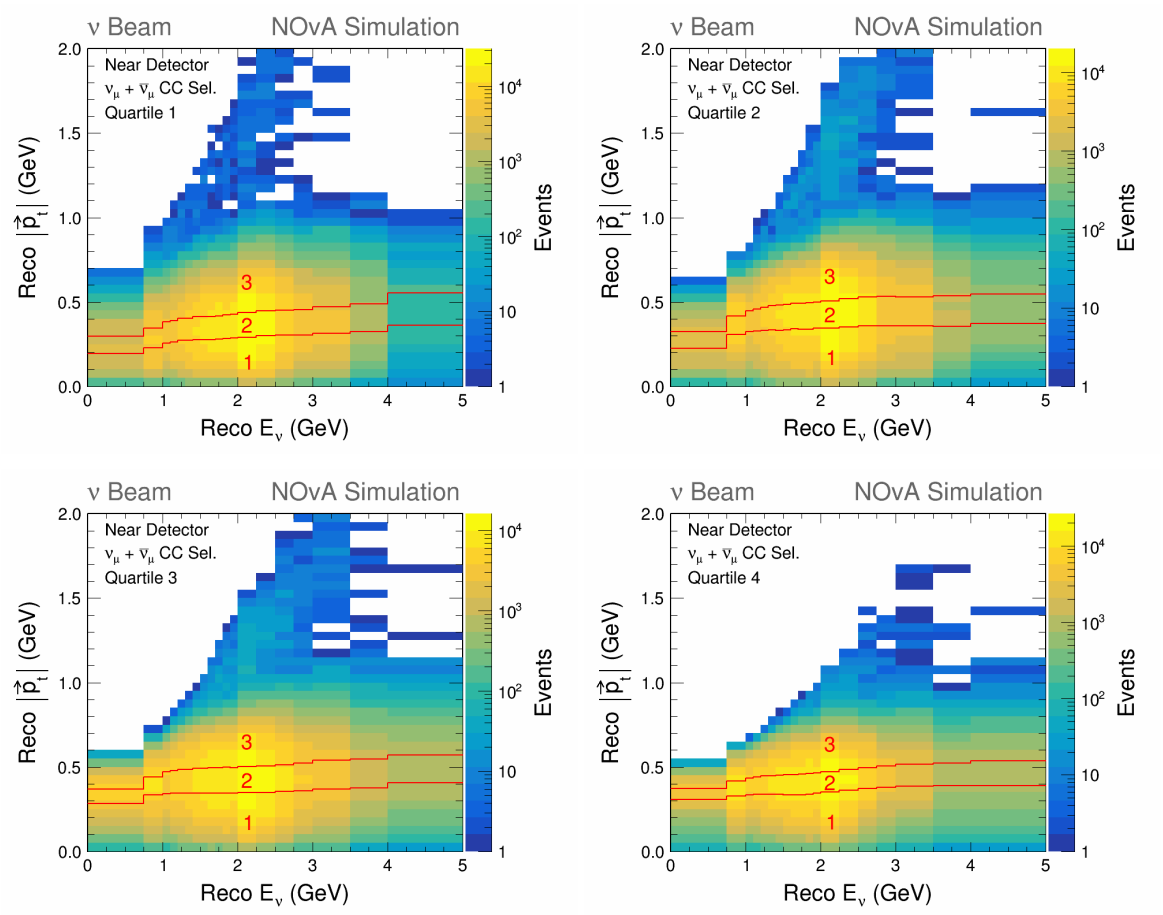

Figure 6.5. MC sample distributions of reconstructed transverse momentum vs. reconstructed ν_μ energy of outgoing lepton in four quartiles with each divided into three p_t-quantiles by red curves

acceptance. Binning the existing near-to-far extrapolation by $\vec{p}_t$-quantiles helps to cancel the kinematic differences between the ND and FD selected samples and thus reduce the systematic uncertainties.

Figure 6.5 [9] shows the boundaries of the p_t-quantiles in all four quartiles at the ND. Each quartile is extrapolated in three p_t-quantiles. At the FD after the extrapolation, the three p_t-quantiles are summed and merged back into one energy resolution quartile so that the p_t-quantiles are not "visible" to the final oscillation fit.

6.1.4 Predictions at FD. With the corrections applied to the FD MC, the pre-

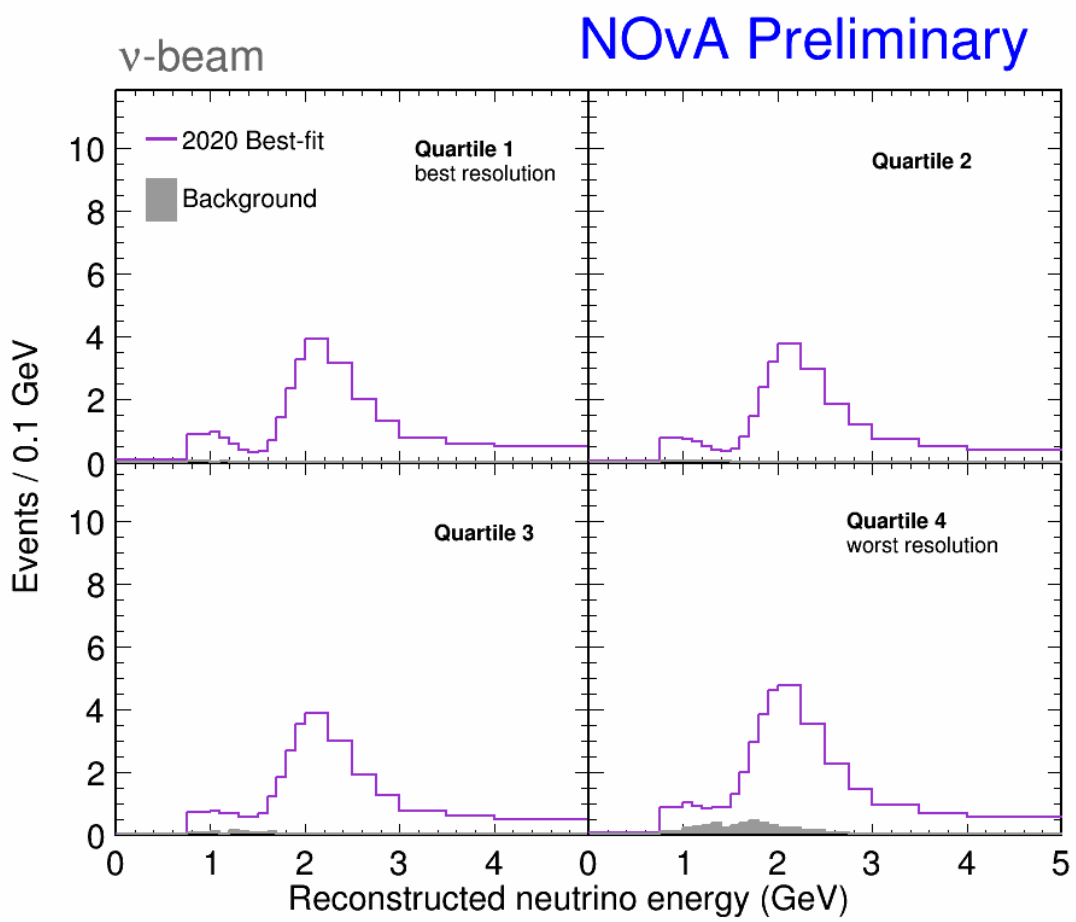

Figure 6.6. Predicted FD ν_μ MC samples in four quartiles with background (gray) consisting of predicted cosmic ray background and MC background components

dicted FD ν_μ MC samples in the four quartiles, with the oscillation parameters from the NOvA 2020 analysis results applied, are shown in Figure 6.6 [9].

6.2 Appearance Analysis

In the $\overset{(-)}{\nu}_e$ appearance analysis, the primary oscillation channel is $\nu_\mu \rightarrow \nu_e$ ($\bar{\nu}_\mu \rightarrow \bar{\nu}_e$). The ND ν_μ ($\bar{\nu}_\mu$) and FD ν_e ($\bar{\nu}_e$) selected data and MC samples are selected and binned for the ν_e ($\bar{\nu}_e$) analysis. The ν_e analysis is used to illustrate the appearance analysis techniques, and the differences in analysis techniques of the $\bar{\nu}_e$ analysis are pointed out.

When we apply the PID selection to the FD to select the $\nu_\mu \rightarrow \nu_e$ signal candidates, intrinsic ν_e events, called beam ν_e, coming from the NuMI flux instead of oscillated from ν_μ can be misidentified as ν_e signal candidates, since beam ν_e and ν_e signal in the FD make no difference to the event CNN classifier. The other two major background components are ν_e-like ν_μ CC and NC. These oscillation background components need to be estimated and corrected properly. We apply the FD ν_e PID selection to the ND data and MC files, and use some data-driven techniques to estimate and correct for the oscillation background misidentified by the PID selection. The corrections are then applied to reweight the FD selected MC samples to constrain the oscillation background. The analysis techniques, similarly to those that are employed in the ν_μ analysis, such as binning, decomposition, and extrapolation techniques, are discussed in this subsection.

6.2.1 Analysis Selection and Binning Methods. We apply the ν_μ ND selection, which is described in the previous section, to get the ND ν_μ candidates. At the FD, the ν_e selection is applied to get the ν_e appearance signal-like candidates. A binning method that combines the ν_e PID and energy bins, called PID/energy, is employed in the ν_e analyses. The selections and bins are optimized using MC samples for maximum figure of merit, which is defined as $\sum_{i=1}^{N} \frac{S_i^2}{S_i+B_i}$ [19], where S_i represents the number of ν_e signal events in bin i, B_i represents number of background events in bin i, and N is the number of bins. The selections are described first, followed by the binning method.

The ν_e selection includes the basic quality and containment selections which are already described in Section 5.1. The ν_e appearance samples are smaller in size compared to the disappearance ν_μ samples. Hence, besides the regular sample (core sample), an additional sample, called the peripheral sample, is used to increase the statistics of the appearance analysis. The core sample, which is larger in size, consists

Table 6.2. Cosmic-rejection BDT and PID Selections for Core Samples

	Cosmic-rejection BDT	PID
ν_e analysis	[0.49,1]	[0.84,1]
$\bar{\nu}_e$ analysis	[0.47,1]	[0.85,1]

of the events passing the "core preselection," ν_e PID selection, and cosmic-rejection core selection, where the ν_e PID selection is based on the event CNN ν_e ID. The peripheral sample, which is smaller in size and used only at the FD, brings more statistics into the analysis by picking out and making use of some events rejected by the core selections.

To gain statistical power in the oscillation fit, the binning method divides the core sample candidates into two bins based on their PIDs. The high (low) PID bin consists of more (less) ν_e signal-like candidates, which comprise a purer (less pure) ν_e appearance signal sample. In each PID bin, the core sample is further binned by the ν_e reconstructed energy. The selection flow is illustrated by the chart shown in Figure 6.7.

The core preselection requires reconstructed ν_e energy between 1 and 4 GeV; number of hits within 30–150; and the longest 3D prong between 1 and 5 m. There are four cosmic-rejection BDTs, each of which is trained independently for the $\overset{(-)}{\nu}_e$ core (peripheral) samples [19], to distinguish $\overset{(-)}{\nu}_e$ signal events from cosmic ray background events. The core FHC (RHC) sample requires a minimum value of 0.49 (0.47) on the cosmic-rejection core BDT and a minimum value of 0.84 (0.85) on the PID. The selection intervals are listed in Table 6.2.

To pick out ν_e signal-like candidates among the events rejected by the three core selections (core preselection, cosmic-rejection core BDT selection, and PID selection), the peripheral preselection loosens the required ν_e energy range to 0–4.5 GeV.

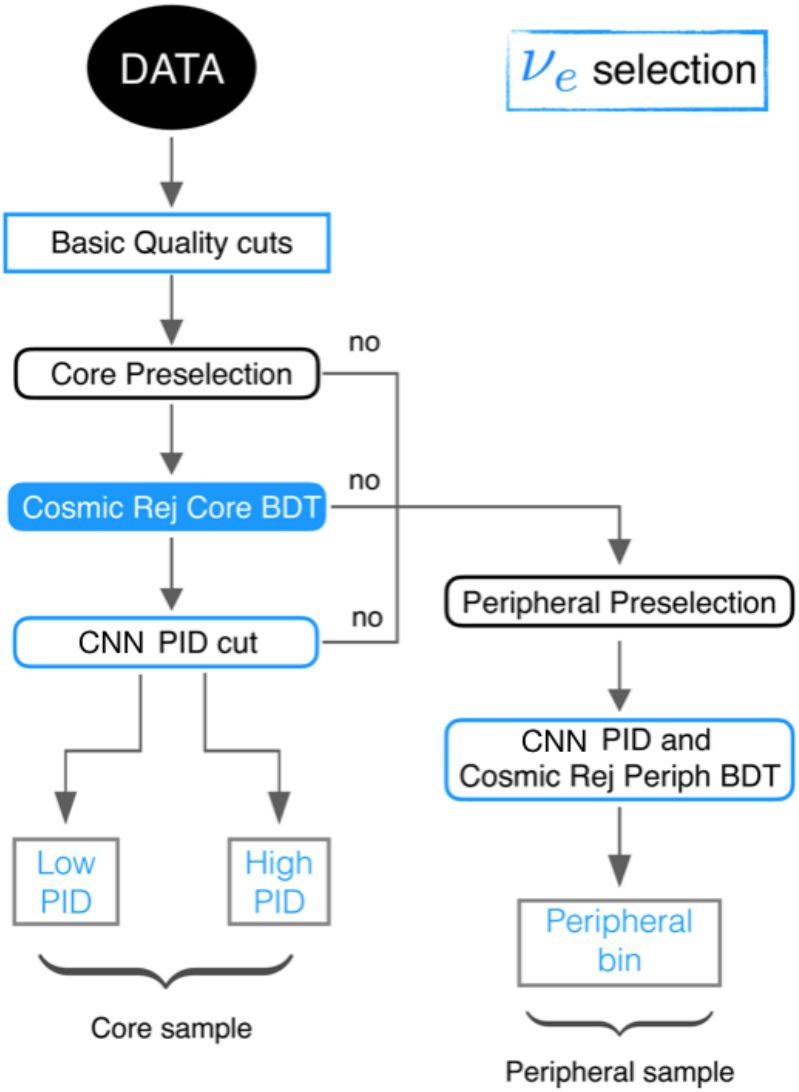

Figure 6.7. Flow chart of ν_e selection.

The PID and cosmic-rejection peripheral BDT are combined such that, as long as one of them decides that the candidate is highly ν_e signal-like, we keep the event in the peripheral sample. The combined selection is defined as a union of two 2D intervals, which are listed in Table 6.3 for both ν_e and $\bar{\nu}_e$ samples. "Interval 1" prefers a higher BDT score; "interval 2" prefers a higher PID score; and the interval boundaries for the ν_e and $\bar{\nu}_e$ analyses are slightly different. As long as a candidate falls into one of the intervals, it qualifies as a peripheral candidate.

Table 6.3. Cosmic-rejection BDT and PID Selections for ν_e ($\bar{\nu}_e$) Peripheral Sample

	Cosmic-rejection BDT	PID
Interval 1	(0.61(0.6),1]	[0.97, 0.995)
Interval 2	(0.57(0.56),1]	[0.995, 1]

Table 6.4. PID Bin Intervals of Core Samples

	Low PID	High PID
ν_e analysis	[0.84,0.97)	[0.97,1]
$\bar{\nu}_e$ analysis	[0.85,0.97)	[0.97,1]

The ν_e ($\bar{\nu}_e$) core samples are divided into low and high PID bins by the candidate PID values. In each PID bin, the core samples are further binned by the ν_e ($\bar{\nu}_e$) reconstructed energy. The bin intervals are listed in Table 6.4. The ν_e selected data and MC samples are used to illustrate what the core and peripheral samples look like, with all the cut and PID bin boundaries plotted, in the 2D spectra of cosmic-rejection BDT vs. PID values shown in Figure 6.8 [9]. The peripheral sample is low in statistics, so it occupies only one of the analysis bins: the peripheral bin. The peripheral sample is not further binned by energy. Both ν_e and $\bar{\nu}_e$ FD predicted sample distributions in bins of PID/energy are plotted in Figure 6.9 [9] with the oscillation parameters from the NOvA 2020 analysis results applied. The wrong-sign MC component in the ν_e ($\bar{\nu}_e$) sample is $\bar{\nu}_e$ (ν_e) appearance.

6.2.2 Background Estimation. In the ν_e appearance analysis we apply a ν_e PID selection at the FD to select ν_e signal candidates. The major background comes from intrinsic beam ν_e events. To get a more precise beam ν_e background estimate at the FD, we make use of our ND data and MC samples. There are two data-driven techniques applied in the ν_e analysis for background estimation: one corrects the beam ν_e background (BEN-Decomp); the other adjusts the ratio of ν_μ CC and

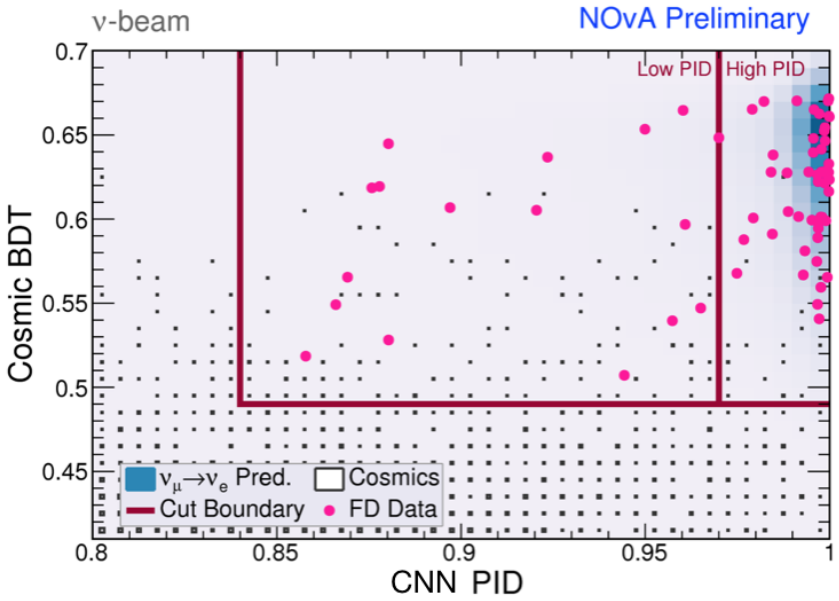

(a) Core Samples

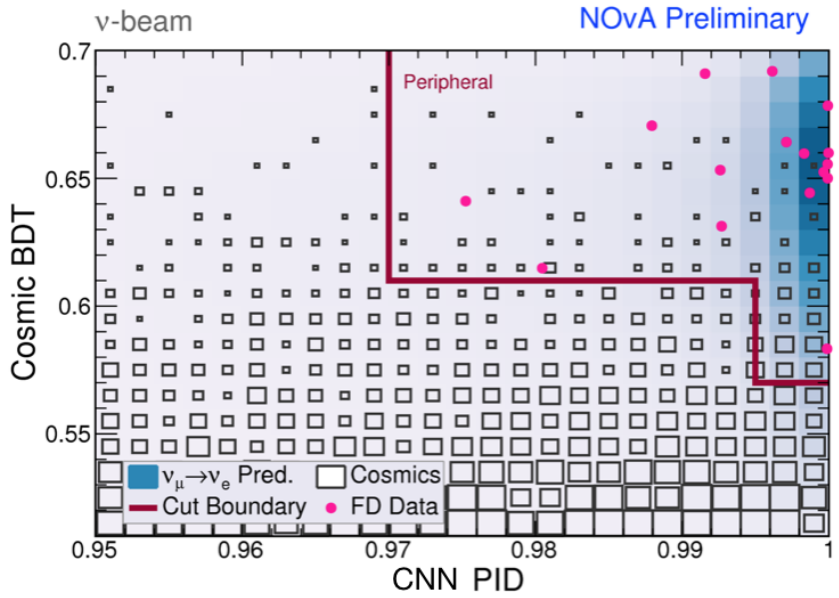

(b) Peripheral Samples

Figure 6.8. Distributions of cosmic-rejection BDT vs. PID values for FD ν_e selected data (pink circles) and MC signal (blue) samples with boxes representing cosmic ray background and red lines indicating the cut boundaries

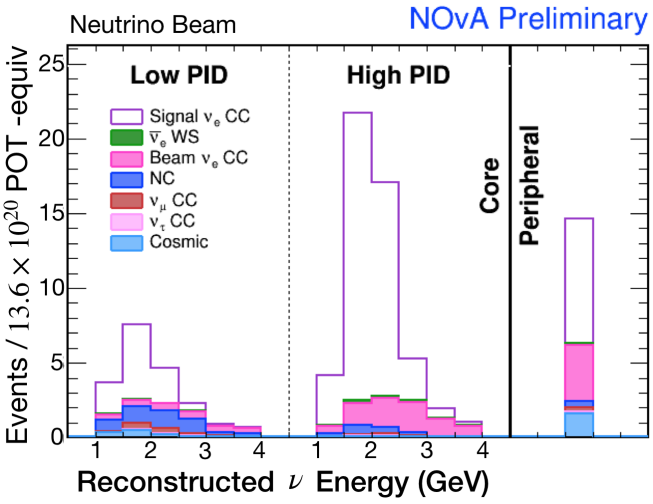

(a) ν_e FD MC

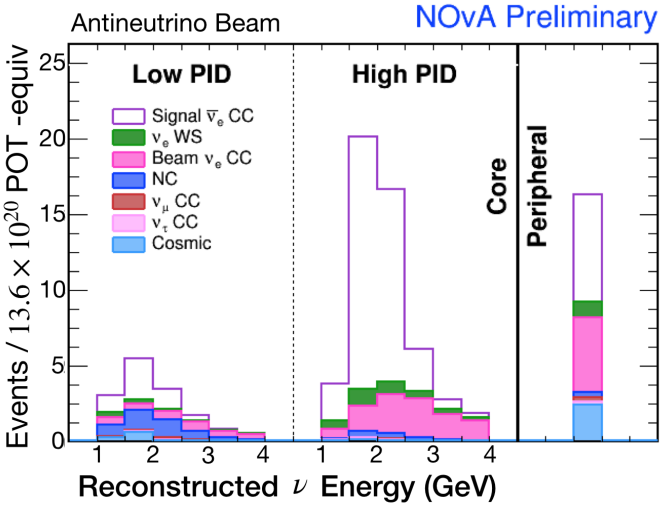

(b) $\bar{\nu}_e$ FD MC

Figure 6.9. Distributions of predicted ν_e and $\bar{\nu}_e$ samples in bins of PID/energy with signal (unfilled purple), cosmic ray background (light blue), and MC simulated beam background components stacked

NC events (Michel-Decomp). The $\bar{\nu}_e$ analysis has only one data-driven technique, called proportional decomposition, which corrects the overall MC to match data. The background estimation techniques in the ν_e analysis are discussed first, followed by the proportional decomposition in the $\bar{\nu}_e$ analysis.

6.2.2.1 Introduction to BEN-Decomp. Beam electron neutrino decomposition (BEN-Decomp) is a technique for estimating the ν_e component of the background. As described in Chapter 2, the NuMI beamline directs the protons onto the target, and outgoing particles, such as pions, kaons, and muons, are focused or defocused by the magnetic horns, then decay to provide neutrino fluxes. These outgoing particles are the ancestors of the neutrinos. At the ND, without significant ν_e appearance, most of the beam ν_e events around 2 GeV come from the ancestor π^+ flux, which decays via

$$\pi^+ \rightarrow \nu_\mu + \mu^+ \,, \tag{6.3}$$

followed by subsequent decay

$$\mu^+ \rightarrow \bar{\nu}_\mu + e^+ + \nu_e \,. \tag{6.4}$$

Details of these decays are well understood [42]. BEN-Decomp estimates the proportion of $\pi^+ \rightarrow \nu_\mu$ in the ND selected ν_μ data and MC samples[9] and reweights the beam ν_e MC events from the subsequent decay of $\mu^+ \rightarrow \nu_e$ in the ND ν_e selected sample. The reweighting information is stored in and applied via the ancestor π^+ true momentum space, which is shared by the child ν_μ and descendent beam ν_e. After correcting the beam ν_e from ancestor π^+ flux, BEN-Decomp incorporates the ν_e

[9]The ancestor π^+s decaying via other channels are negligible in our selected ν_μ samples.

events decayed from K^+ and K^0_L, and corrects them by an overall normalization. The normalizing factor is calculated using the ND ν_μ data and MC samples dominated by kaon flux. There are a couple of reasons that we reweight the kaon flux by an overall normalization instead of a bin-by-bin correction as we do to the pion flux. Firstly, the major kaon flux does not have a decay chain as the pion flux does. Secondly, the kaon flux dominated samples are too low in statistics to support a bin-by-bin correction. In addition, the kaon flux dominates the high energy range in the selected samples, while the neutrino energy estimators are designed for the low energy (0–5 GeV) analysis samples and have poor performance in the high energy range. Therefore, they are not useful for energy based corrections. To the remaining beam ν_e backgrounds that come from the remaining flux, we do not make any corrections due to their low statistics. As a short summary, the BEN-Decomp technique adjusts the ratio of beam ν_e events from π^+ and kaon flux by using the high statistics ND ν_μ samples to reweight the flux components. In the plot of ν_μ (ν_e) CC flux shown in Figure 6.10 (6.11) [9], the π^+, K^+, and K^0_L fluxes are defined as above. The

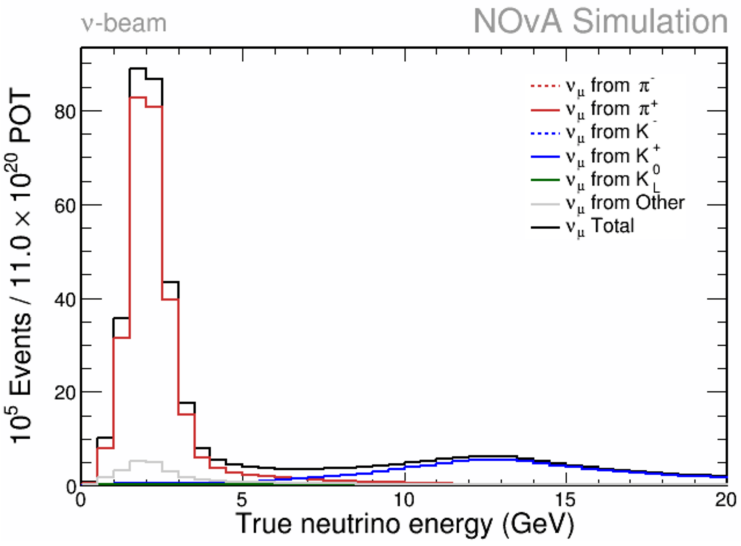

Figure 6.10. Stacked true neutrino energy distributions of ND ν_μ CC flux broken down by ancestor flux type

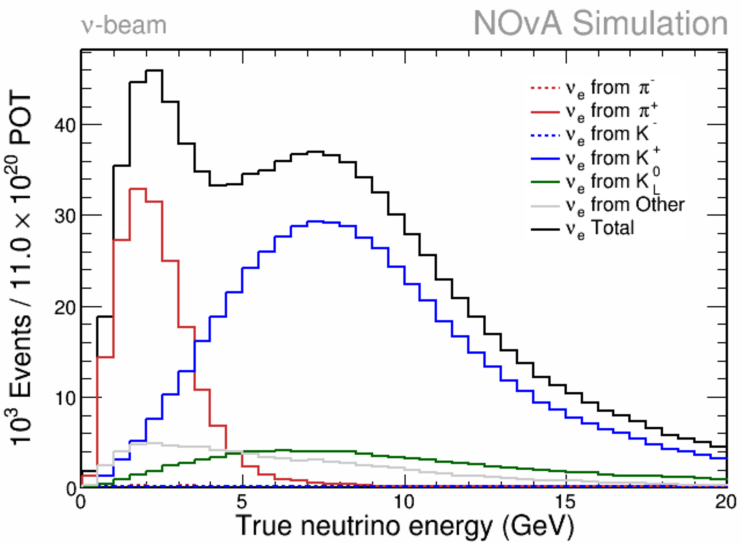

Figure 6.11. Stacked true neutrino energy distributions of ND beam ν_e flux broken down by ancestor flux type

remaining minor decays not listed in the legend but leading to ν_μ (ν_e) interactions are categorized as "Other." The "Background" category consists of antineutrino, ν_e (ν_μ), and ν_τ interactions. As shown in the ν_μ CC plot, the low energy region has large statistics and is dominated by the ancestor π^+ flux. The high energy region, which is lower in statistics, is essentially from ancestor kaon flux. The majority of low energy beam ν_e are from ancestor pion flux. In the high energy range (above 5 GeV), most ν_e events originate from charged and neutral kaons. The ND selected ν_μ contained (Figure 6.12) and uncontained (Figure 6.13) data and MC samples are used to constrain first the ancestor pion flux, then the kaon flux.

Two different selections are applied to get the two sets of samples for the decomposition corrections. The ND ν_μ oscillation selection, which has been described earlier in Subsection 6.1.1, is applied to get the low energy data and MC samples, called the contained samples, for constraining the pion flux. The high energy ν_μ events, rejected by the ND ν_μ selection, but selected by the enhanced kaon selection [43], have a wider energy range and are dominated by the kaon flux. The 0–5 GeV

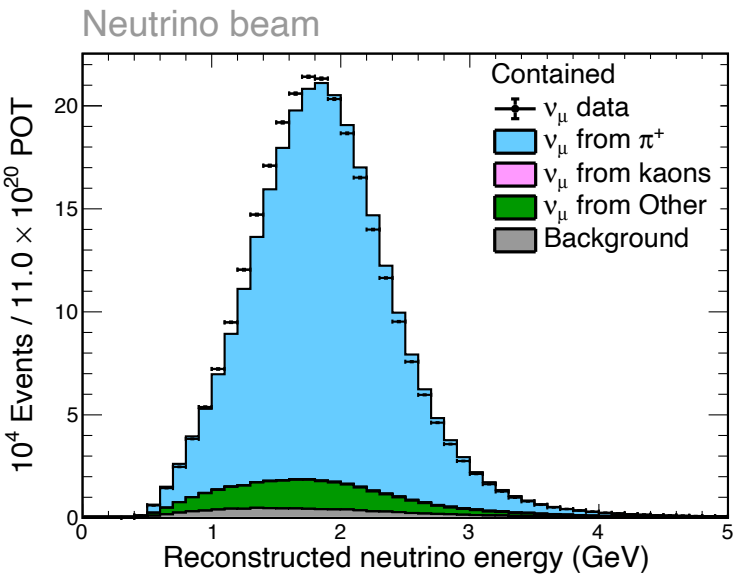

Figure 6.12. Reconstructed ν_μ energy distributions of ND selected ν_μ contained data (black circles) and MC (color-filled and stacked) samples

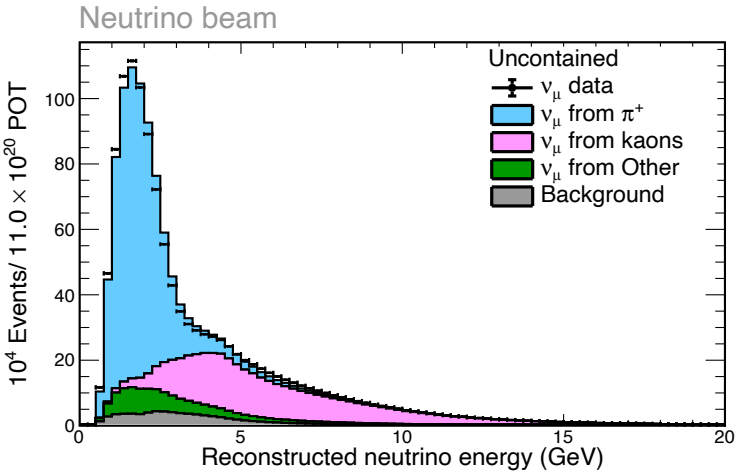

Figure 6.13. Reconstructed ν_μ energy distributions of ND selected ν_μ uncontained data (black circles) and MC (color-filled and stacked) samples

contained events are used to constrain the pion flux. The 4.5–10 GeV uncontained events are used to constrain the kaon flux. The uncontained selection includes the ν_μ basic quality selection (see Subsection 6.1.1) and also requires: the interaction vertex coordinates to satisfy $x, y \in (-170, +170)$ cm, $z \in (30, 1150)$ cm; the longest Kalman track to start within $x, y \in (-170, +170)$ cm, $z \in (30, 1150)$ cm and end outside the

volume of $x, y \in (-185, +185)$ cm, $z \in (19, 1275)$ cm; and the largest ReMID value among all the Kalman tracks in the event to be greater than 0.75.

6.2.2.2 Constraining the π^+ Flux.

The ν_μ contained sample (Figure 6.12) shows relatively good data and MC agreement. To constrain the pion flux, we split the discrepancy between data and MC between π^+ and kaon flux according to the ratio of their descendent ν_μ MC events. However, the kaon component in the contained samples is negligible, so the effect on π^+ flux correction from kaon is considered to be negligible. The ν_μ contained samples constrain the ancestor pion flux by reweighting the pion true momentum space, which is shared by the descendent ν_μ and beam ν_e events.

The ν_μ weights (w_{ν_μ}) calculated using the ν_μ contained sample are defined, in each ν_μ reconstructed energy bin i, as

$$w_{\nu_\mu}(i) = \frac{\text{data}(i) - \text{MC}^{\text{Background}}(i) - \text{MC}^{\text{Other}}(i)}{\text{MC}^{\pi^+}(i) + \text{MC}^{\text{kaons}}(i)}\,, \tag{6.5}$$

where data(i) is the number of data events in bin i, and $\text{MC}^{\text{component}}(i)$s with various superscripts (component=$\{\pi^+$, kaons, Background, Other$\}$) represent the true ν_μ CC number of events in bin i of the various MC components in the contained ν_μ sample.

Once we have the ν_μ weights, we propagate them to the pion true momentum space, which is represented by forward momentum (p_z) and transverse momentum (p_t). This is done by reweighting a 3D spectrum of (p_z, p_t) as a function of reconstructed ν_μ energy (z-axis), of which the 2D projection on (p_z, p_t) is shown in Figure 6.14. Each (p_z, p_t) bin has a different reconstructed ν_μ energy distribution. The ν_μ weights w_{ν_μ} are applied to the z-axis. Looping over all the (p_z, p_t) bins in the ν_μ 3D spectrum, we calculate and save the π^+ weights ($w(p_z, p_t)$) in (p_z, p_t) bins.

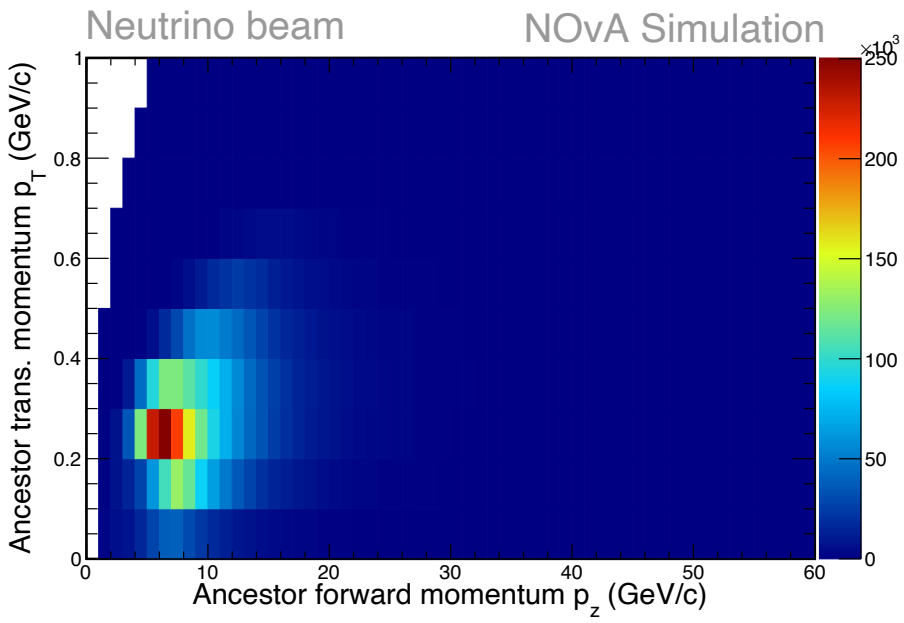

Figure 6.14. Original 2D spectrum of ancestor π^+ true momentum space (p_z, p_t) for selected contained ν_μ CC MC events from ancestor π^+ flux

The details of how to reweight via π^+ true momentum space are described as follows. In each (p_z, p_t) bin, the ν_μ weight ($w_{\nu_\mu}(i)$) is applied to reweight the number of ν_μ MC events in the reconstructed ν_μ energy bin (i). After reweighting all the (p_z, p_t) bins, the π^+ weight in bin (p_z, p_t) is defined as the ratio of the bin contents before and after the reweighting:

$$w(p_z, p_t) = \frac{\sum_{i=1}^{N} w_{\nu_\mu}(i)) \times n_{\nu_\mu}(i|(p_z, p_t))}{\sum_{i=1}^{N} n_{\nu_\mu}(i|(p_z, p_t))}\,, \tag{6.6}$$

where $w(p_z, p_t)$ represents the calculated π^+ weight in bin (p_z, p_t); N is the number of reconstructed ν_μ energy (z-axis) bins, which is the same as that of the contained sample (Figure 6.12); and $n_{\nu_\mu}(i|(p_z, p_t))$ is the number of ν_μ CC events in bin i. The π^+ weights are then applied to reweight the true momentum bins in the 3D spectrum (p_z, p_t, PID/energy) to constrain the beam ν_e samples from the pion flux. The original beam ν_e (p_z, p_t) projected distribution before reweighting is shown in Figure 6.15. The z-projection of the reweighted 3D beam ν_e spectrum is thus the beam ν_e MC

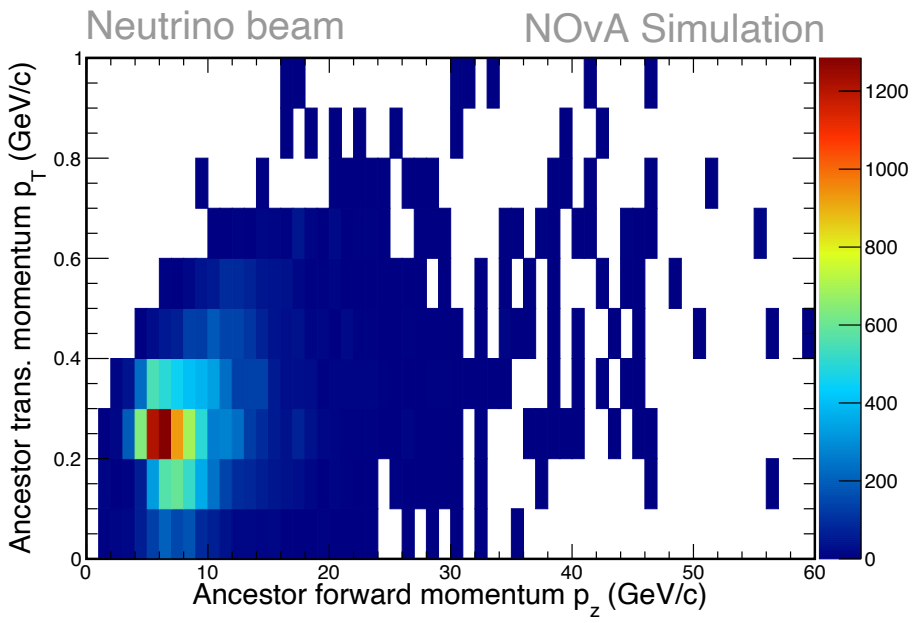

Figure 6.15. Original 2D spectrum of ancestor π^+ true momentum space (p_z, p_t) for beam ν_e MC events from ancestor π^+ flux

spectrum constrained by the contained ν_μ samples.

6.2.2.3 Constraining the Kaon Flux.

In the second part of the BEN-Decomp technique, we use the high energy ν_μ selected uncontained samples, dominated by ancestor kaon flux, to rescale beam ν_e MC events from kaon ancestors; the overall scaling factor is called the kaon scale.

BEN-Decomp uses the high energy (4.5–10 GeV) ν_μ uncontained sample, which is dominated by kaon flux but still has some ν_μ events from pion flux, to calculate the kaon scale iteratively. We do not use the pion weights extracted from the contained ν_μ samples directly, such that the constraint on kaon flux does not fully depend on the result of the pion flux constraints. Hence, it is necessary to have an additional sample to constrain the small portion of uncontained ν_μ events from pion flux and also to make sure the final kaon scale performs well on both samples. A subsample (0.75–3 GeV) from the contained ν_μ is used to constrain the scaling factor of π^+ flux

in the iterations of calculating the kaon scale.

The scaling factor of the π^+ flux ($\text{scale}_{\pi^+}^{(i+1)}$) on iteration $i+1$ is defined based on that of the kaon flux ($\text{scale}_{\text{kaons}}^{i}$) from iteration i:

$$\text{scale}_{\pi^+}^{(i+1)} = \frac{\text{data} - \text{scale}_{\text{kaons}}^{(i)} \times \text{MC}_{\text{kaons}} - \text{MC}_{\text{Background}} - \text{MC}_{\text{Other}}}{\text{MC}_{\pi^+}}, \tag{6.7}$$

which is calculated on the 0.75–3 GeV contained ν_μ sample (Figure 6.12); and the kaon scale on iteration $i+1$ is defined by:

$$\text{scale}_{\text{kaons}}^{(i+1)} = \frac{\text{data} - \text{scale}_{\pi}^{(i+1)}\text{MC}_{\pi^+} - \text{MC}_{\text{Background}} - \text{MC}_{\text{Other}}}{\text{MC}_{\text{kaons}}}, \tag{6.8}$$

which is calculated on the 4.5–10 GeV ν_μ uncontained samples (Figure 6.13). In both equations, data and $\text{MC}_{\text{component}}$ (component=$\{\pi^+$, kaons, Background, Other$\}$) represent the number of events in the range 4.5–10 GeV of the data and corresponding MC components in the uncontained samples. To start iterating, the $\text{scale}_{\text{kaons}}^{0}$ is initialized as 1 and used to calculate the $\text{scale}_{\pi^+}^{1}$ using Equation 6.7. Then, the $\text{scale}_{\pi^+}^{1}$ updates the $\text{scale}_{\text{kaons}}^{1}$ by using Equation 6.8. After a couple of iterations, when the change of $\text{scale}_{\text{kaons}}$ drops below $10^{-4}\%$, the iteration stops and the last $\text{scale}_{\text{kaons}}$ is used as the overall normalization constant. It is used to rescale the ν_e MC component from kaon flux in the ND ν_e selected MC sample.

6.2.2.4 Results of BEN-Decomp.

Figure 6.16 shows the beam ν_e events in the ND ν_e selected MC sample after BEN-Decomp. The results are listed in Table 6.5.

6.2.2.5 Michel-Decomp and Proportional Decomposition.

After the beam ν_e MC component in the ND ν_e selected sample is corrected by the BEN-Decomp technique, the ratio of the remaining ν_μ CC and NC background

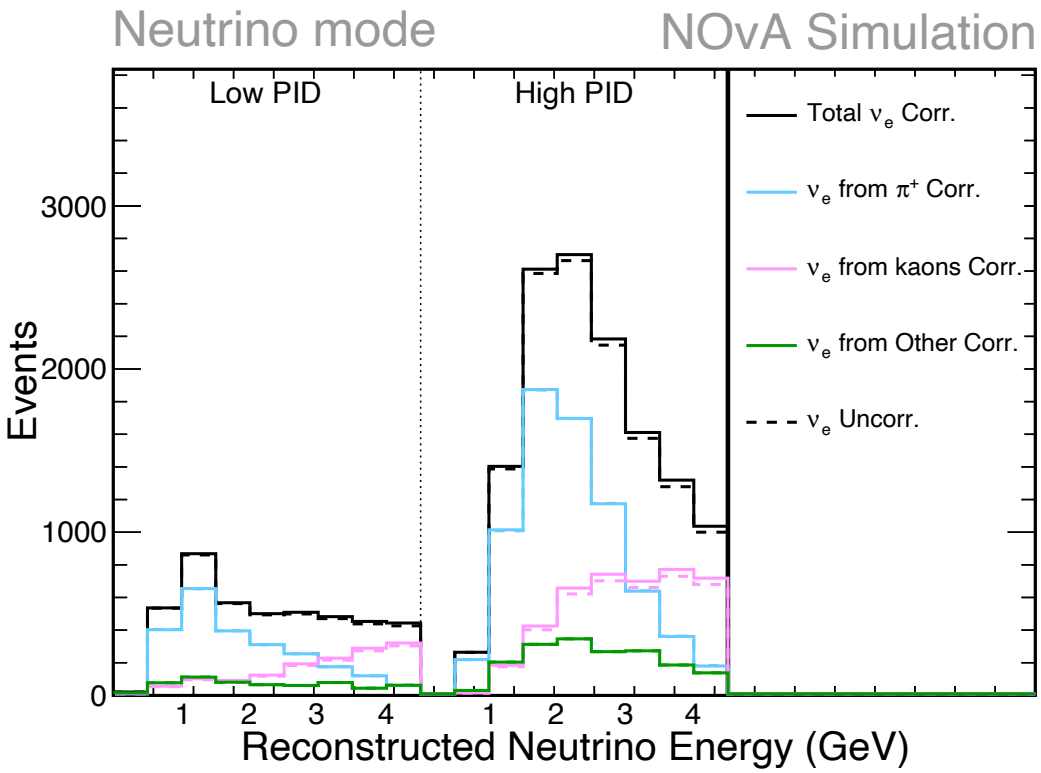

Figure 6.16. Distributions of ND selected beam ν_e MC events in bins of PID/energy broken down by ancestor flux type (colored histograms), before (dash) and after (solid) BEN-Decomp

Table 6.5. Changes of Beam ν_e from Ancestor Fluxes in PID Bins

0–4.5 GeV	Low PID	High PID	Total
ν_e from π^+	0.007%	0.011%	0.010%
ν_e from kaons	5.751%	5.751%	5.751%

components is adjusted by another data-driven technique called Michel-Decomp [19]. With both decomposition techniques applied, the ND ν_e selected data and MC samples agree well with each other as plotted in Figure 6.17 [9]. The changes of the three MC components in the ND ν_e selected MC sample caused by the decomposition techniques are listed in Table 6.6.

The background estimation for the $\bar{\nu}_e$ analysis is simpler than the ν_e decom-

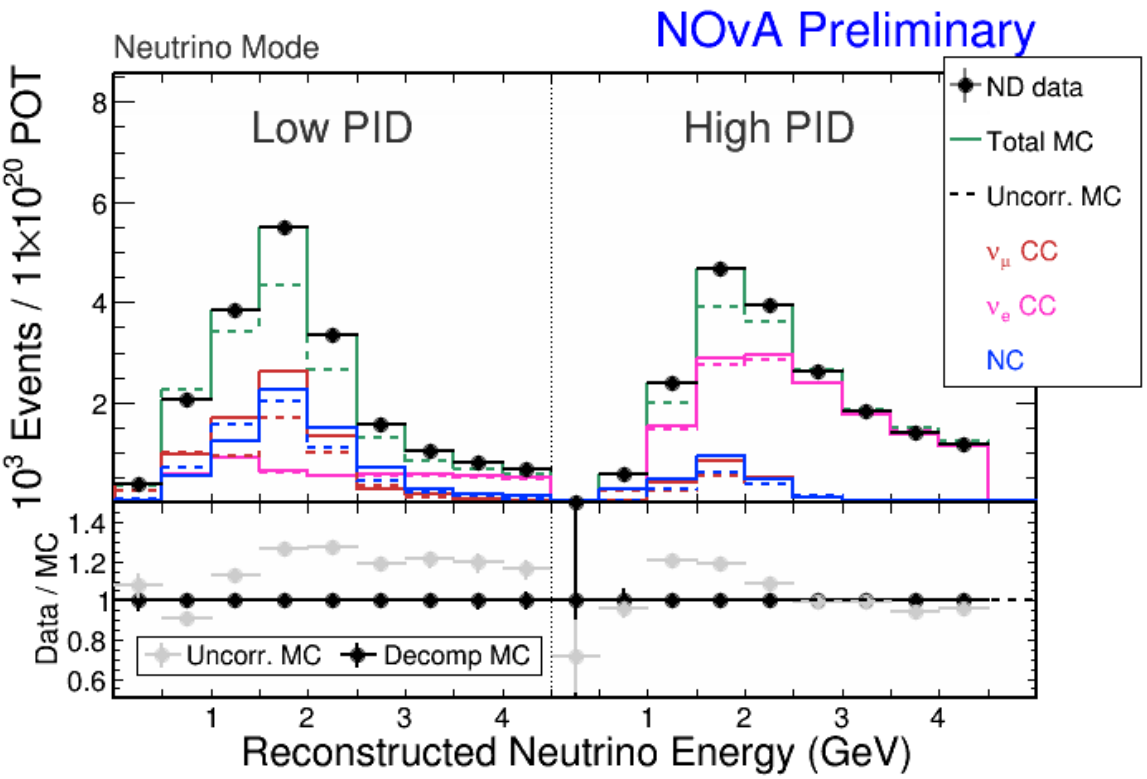

Figure 6.17. Distributions of ND ν_e selected data and MC (stacked) samples in bins of PID/energy before (dashed) and after (solid) decomposition corrections applied with ratio of data to MC shown at bottom

Table 6.6. Changes of MC Components

0–4.5 GeV	ν_e CC	ν_μ CC	NC
FHC	+2.2%	+32.6%	+16.4%

position techniques. It is called proportional decomposition. It scales all the MC components by the same factor in each bin of the MC distribution. In the end, the total MC sample distribution matches the selected data sample distribution. Using the ND ν_e selected data and MC samples in bins of PID/energy, the scaling factor $f(i)$ at bin i is defined by $\frac{\text{data}(i)}{MC(i)}$, where data($i$) is the number of observed data candidates in bin i, and MC(i) is the number of MC events in bin i. This is the simplest way to handle the data/MC discrepancy, and it is efficient when the statistics of the samples are insufficient to employ more complicated analysis techniques. NOvA employed

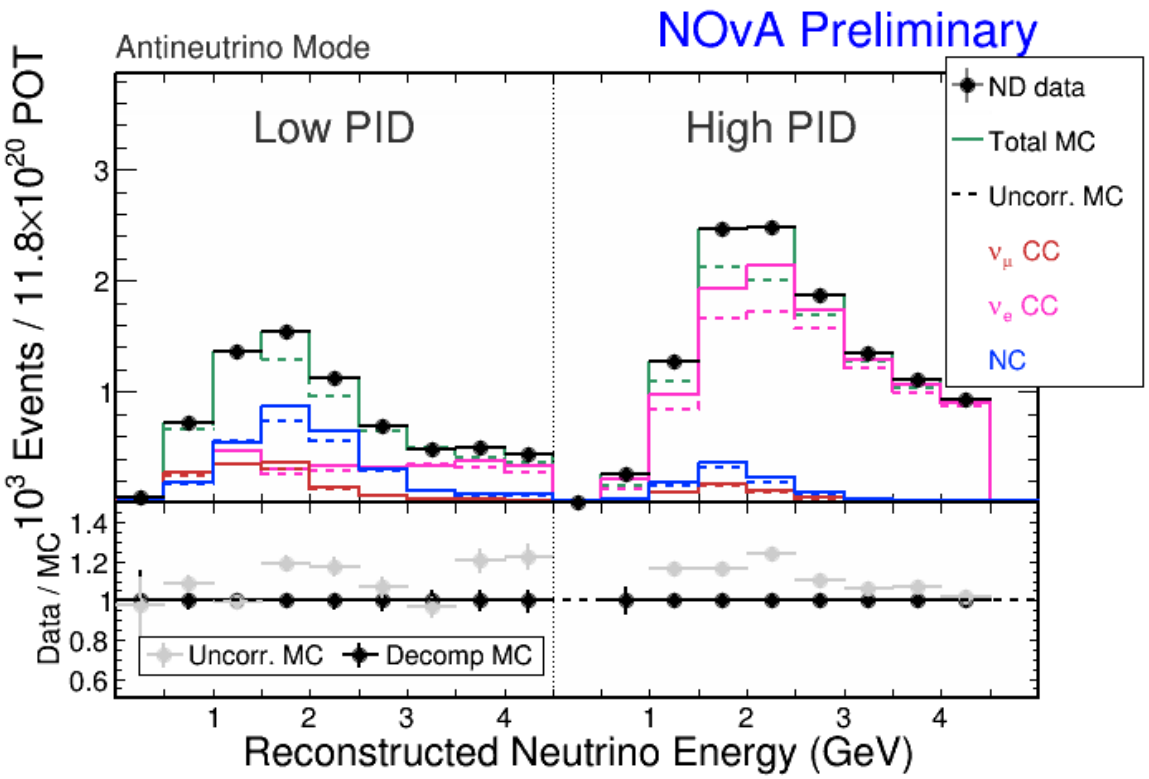

Figure 6.18. Distributions of ND $\bar{\nu}_e$ selected data and MC (stacked) samples in bins of PID/energy before (dashed) and after (solid) decomposition corrections applied with ratio of data to MC shown at bottom

the proportional decomposition technique for its first published results [45]. The ND selected $\bar{\nu}_e$ data and MC samples are plotted in Figure 6.18 [9].

6.2.3 $\overset{(-)}{\nu}_e$ Extrapolation. Using the decomposition techniques, we use the ND selected data samples to correct the MC components such that the corrected MC sample better describes the observed ND data. The near-to-far extrapolation then propagates the corrections as weights to reweight the MC components individually in the FD selected MC samples. Both true- and reco-extrapolation methods are used in the ν_e analysis. The true-extrapolation is used in the ν_e and $\bar{\nu}_e$ appearance channels. It is similar to that of the ν_μ analysis, where the ND decomposition correction weights are propagated via the two 2D matrices (ND reco-to-true and FD true-to-reco). The other channels follow reco-extrapolation, which reweights the FD

MC in bins of PID/energy. The FD true-to-reco matrix is used to apply oscillation probabilities, if any, as weights to the oscillated MC components.

6.2.4 Prediction at FD. After extrapolation, the cosmic ray background component needs to be added to the FD predicted MC samples. The cosmic data sets are collected during the time between NuMI spills. The predicted MC samples at the FD with the oscillation probabilities, using the NOvA 2020 analysis results [19], applied are already shown in Figure 6.9.

6.3 Oscillation Result of Joint Analysis

The final oscillation analysis combines the four analyses: ν_μ, $\bar{\nu}_\mu$, ν_e, and $\bar{\nu}_e$. The FD predicted MC samples from these four analyses are fit to the data samples simultaneously for oscillation parameter extraction. There are several neutrino oscillation experiments which have set constraints on the oscillation parameters, such as MINOS, T2K, IceCube, and Super-K, which have constrained $\sin^2\theta_{23}$ and Δm^2_{32}, and T2K has further constrained δ_{CP}. Since NOvA has the longest baseline of any accelerator neutrino experiment to date, NOvA's ν_μ and $\bar{\nu}_\mu$ analyses provide a powerful constraint on the $\sin^2\theta_{23}$ and Δm^2_{32} values, and the ν_e and $\bar{\nu}_e$ samples give us a chance to further measure the value of δ_{CP}. The results from these experiments are compared and discussed later in the section after we discuss the fitting method, results, and the analysis systematic uncertainties.

6.3.1 Oscillation Fitting Method. In the oscillation fit, we seek a point in oscillation parameter space at which the combination of $\sin^2\theta_{23}$, Δm^2_{32}, and δ_{CP} values predicts MC samples that best describe the data; we call this the best-fit point. Frequentist statistical inference [42] is employed to search for the best-fit point

by minimizing a Poisson log-likelihood function defined by

$$-2\ln\lambda(\vec{\theta}) = 2\sum_{i=1}^{N}\left[p_i(\vec{\theta}) - o_i + o_i\ln\frac{o_i}{p_i(\vec{\theta})}\right], \tag{6.9}$$

where N is the number of analysis bins of all the samples, including ν_e and $\bar{\nu}_e$ in bins of PID/energy, and ν_μ and $\bar{\nu}_\mu$ in bins of quartile and energy; $p_i(\vec{\theta})$ represents the number of predicted MC events in bin i, using the oscillation parameters $\vec{\theta} = (\theta_{23}, \Delta m^2_{32}, \delta_{CP})$; and o_i represents the number of observed data candidates in bin i of the data samples. The distribution of the values calculated from the log-likelihood function (Equation 6.9) is asymptotic to a χ^2 distribution, given some regularity conditions [42]:

$$\chi^2 = -2\ln\lambda(\vec{\theta})\,. \tag{6.10}$$

The χ^2 values tell us the deviation of the observed data from the predicted MC samples. At the best-fit point ($\hat{\theta} \equiv \vec{\theta}_{\text{best}}$), the log-likelihood function in Equation 6.9 is minimized as

$$\chi^2_{\text{best}} \equiv \min_{\vec{\theta}}(\chi^2(\vec{\theta}))\,. \tag{6.11}$$

Using χ^2_{best}, we can define a non-negative test statistic as

$$\Delta\chi^2(\vec{\theta}) = \chi^2(\vec{\theta}) - \chi^2(\hat{\theta})\,. \tag{6.12}$$

With the $\Delta\chi^2(\vec{\theta})$ test, we can compare two sets of oscillation parameters. A smaller $\Delta\chi^2(\vec{\theta})$ value means that the parameter point describes the observed data better. We assume large samples such that the χ^2 distribution is approximated by a Gaussian distribution [42]. In this way, we estimate the central values of the parameters and the

corresponding sensitivities. Then the unified approach of Feldman and Cousins (FC method) [47] is employed to construct confidence intervals for the fitted parameters.

6.3.2 Systematic Uncertainties. The systematic uncertainties are assumed as independent Gaussian distributions and added to the likelihood function as nuisance parameters, which are free during the fit. At each point of the oscillation parameter space, the updated $\chi^2(\vec{\theta})$ is then minimized with respect to the systematic nuisance parameters using penalty terms.

We do not expect the nominal MC samples to be perfect descriptions of the data samples. We estimate the systematic uncertainties, and add them to correct the predicted MC samples. To account for the systematic uncertainty effects in the oscillation fit, we update the Poisson log-likelihood function (Equation 6.9) as

$$-2\ln\lambda(\vec{\theta},\vec{s}) = 2\sum_{i=1}^{N}\left[p_i(\vec{\theta},\vec{s}) - o_i + o_i\ln\frac{o_i}{p_i(\vec{\theta},\vec{s})}\right], \tag{6.13}$$

where $p_i(\vec{\theta},\vec{s})$ is the updated number of predicted MC events in bin i, which is affected by both oscillation parameters $(\vec{\theta})$ and systematic uncertainties $(\vec{s})$. All the remaining terms are the same as those in Equation 6.9. Since the likelihood is now a function of the systematic nuisance parameters $\vec{s}$ as well as of $\vec{\theta}$, then so is the χ^2 function, which we now write as follows:

$$\chi^2(\vec{\theta},\vec{s}) = \min_{\vec{s}}\left(-2\ln\lambda(\vec{\theta},\vec{s}) + \sum_{i=1}^{Syst.}\frac{s_i^2}{\sigma_i^2}\right), \tag{6.14}$$

where i runs through all the systematic uncertainties $(Syst.)$, s_i is the nuisance parameter of systematic i, and σ_i^2 represents the number of MC events in a 1σ range of the predicted MC sample when systematic i is applied. A large value of σ_i^2 corresponds to a small weight of the systematic i during the fit. $\frac{s_i^2}{\sigma_i^2}$ is thus used as a penalty term, which tends to keep the systematic effects in the oscillation parame-

ter fit within their 1σ ranges. Using the updated $\chi^2(\vec{\theta}, \vec{s})$ function, the oscillation fit gives us the best estimate of not only the oscillation parameters, but also the nuisance parameters.

6.3.3 Fitting Details. The oscillation probability depends on several physics quantities, such as baseline and average matter density (to account for the matter effect). To have a powerful constraint on the parameters of interest, θ_{23}, Δm^2_{32}, and δ_{CP}, we constrain the remaining oscillation parameters by using the results measured previously by several experiments [42]. The input quantities and parameters are as follows:

$$L = 810 \text{ km}, \tag{6.15}$$

$$\rho = 2.84 \text{ g/cm}^3, \tag{6.16}$$

$$\Delta m^2_{21} = 7.53 \times 10^{-5} \text{ eV}^2/c^4, \tag{6.17}$$

$$\sin^2(2\theta_{12}) = 0.851, \tag{6.18}$$

where L is the NOvA baseline, and ρ is the average density of the earth, estimated using the average depth of the two detectors [48]. The parameter θ_{13} is constrained by the world average $\sin^2(2\theta_{13}) = 0.085 \pm 0.003$ [42].

6.3.4 Joint Fit result. The results of the joint fit for the central values of the oscillation parameters before applying the FC method are: $\sin^2\theta_{23} = 0.57$, $\Delta m^2_{32} = 2.41 \times 10^{-3}$ eV$^2/c^4$, and $\delta_{CP} = 0.82\pi$. The 2D plots shown in Figures 6.19 and 6.20 are filled by the χ^2 values of points in the oscillation parameter space before the FC method is applied. The contours indicate the boundaries of the 1, 2, and 3σ regions, corresponding to 68%, 95%, and 99.7% confidence level (C.L.). The official results are corrected using the FC method, as shown in Figures 6.21 and 6.22, and the best-fit

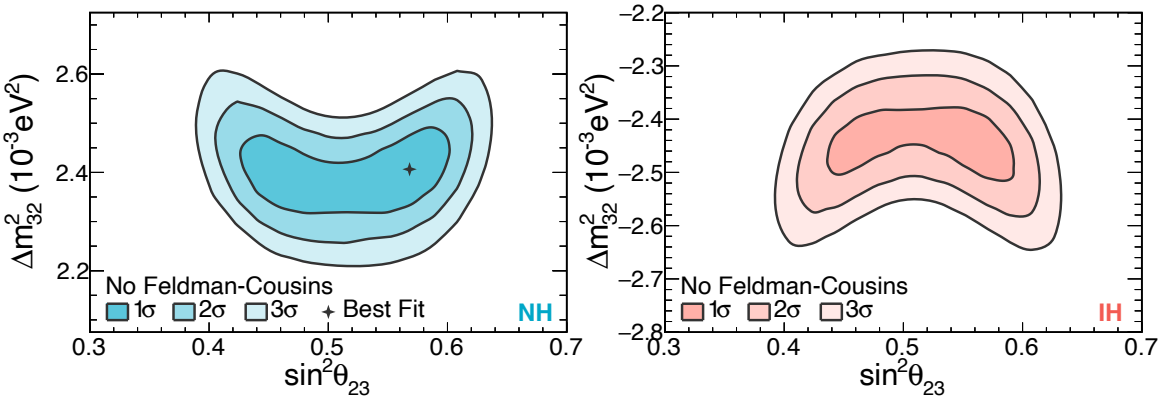

Figure 6.19. Two dimensional spectra of Δm^2_{32} vs. $\sin^2\theta_{23}$ by assuming normal (left) or inverted (right) mass ordering with colors representing significance levels before FC method is applied

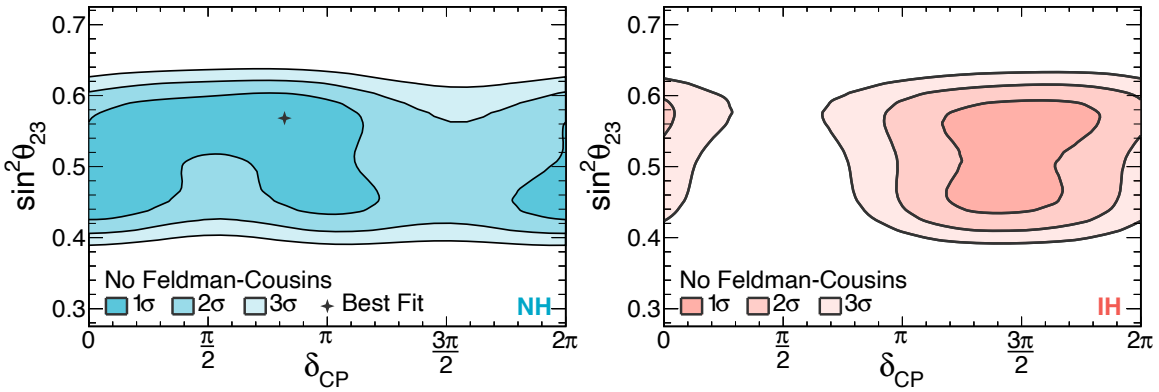

Figure 6.20. Two dimensional spectra of $\sin^2\theta_{23}$ vs. δ_{CP} by assuming normal (left) or inverted (right) mass ordering with colors representing significance levels before FC method is applied

Table 6.7. Best-fit Oscillation Parameters of NOvA 2020 Analysis[10]

$\sin^2\theta_{23}$	Δm^2_{32} (10^{-3} eV$^2/c^4$)	δ_{CP}
$0.57^{+0.03}_{-0.04}$	$2.41^{+0.07}_{-0.07}$	0.82π

oscillation parameters with their 1σ intervals [19] are listed in Table 6.7.[10]

In Figure 6.23 [9], the 90% C.L. contours in $\sin^2\theta_{23}$ and Δm^2_{32} space assuming normal neutrino mass ordering from different experiments are plotted and compared with each other. NOvA's 90% C.L. region is compatible with those of the other ex-

[10] δ_{CP} has a wide 1σ interval, [0,1.06] $\cup$ [1.82,2], which is not listed in the table.

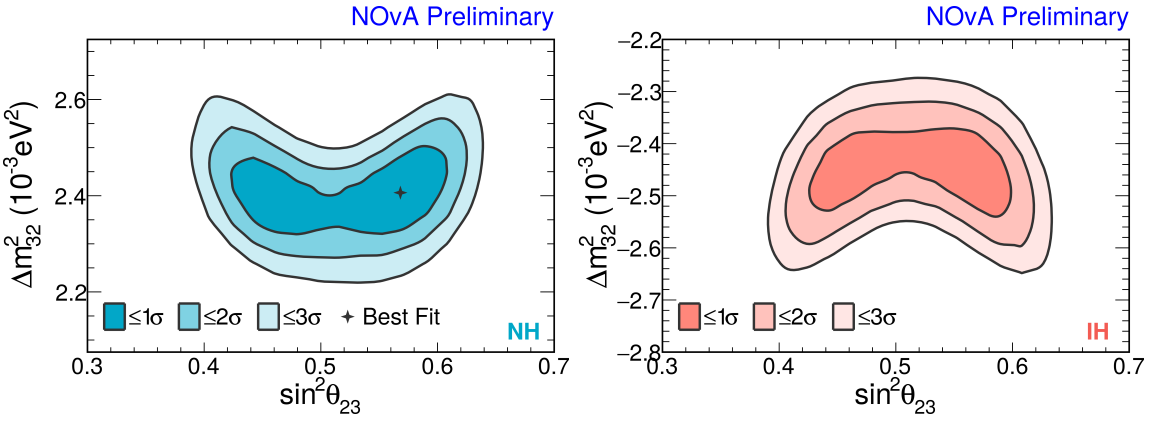

Figure 6.21. Two dimensional spectra of Δm^2_{32} vs. $\sin^2\theta_{23}$ by assuming normal (left) or inverted (right) mass ordering with colors representing significance levels after FC method is applied

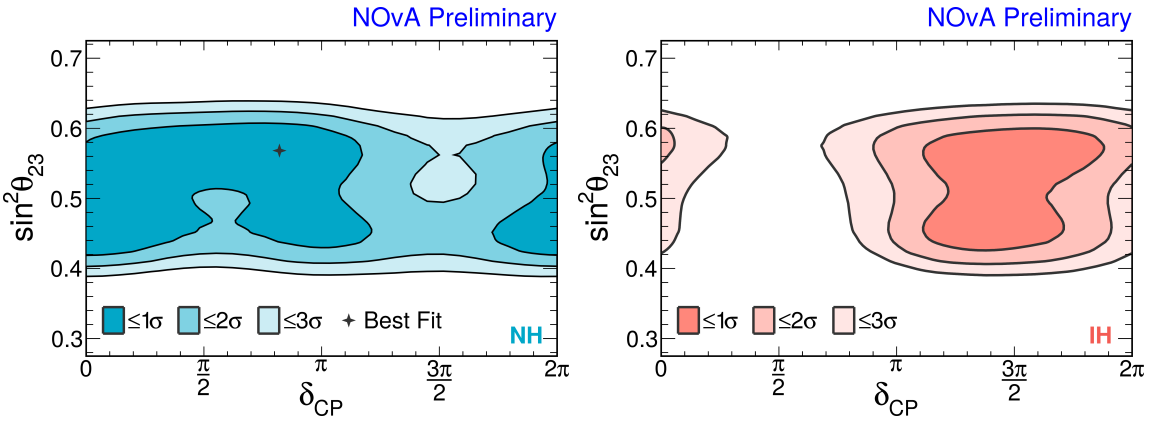

Figure 6.22. Two dimensional spectra of $\sin^2\theta_{23}$ vs. δ_{CP} by assuming normal (left) or inverted (right) mass ordering with colors representing significance levels after FC method is applied

periments and much narrower in Δm^2_{32}. MINOS and NOvA share the same beam, the NuMI beam, and both are long-baseline neutrino oscillation experiments with similar baselines using two detectors, which may lead to similarly shaped confidence regions. The value of Δm^2_{32} is highly constrained by the ν_μ and $\bar{\nu}_\mu$ disappearance analyses. The NuMI beam facility provides a well understood ν_μ flux for both MINOS and NOvA, which has been optimized to measure ν_μ disappearance. Hence, MINOS and NOvA are more sensitive to Δm^2_{32} compared to the atmospheric neutrino experiments shown, i.e., Super-K and IceCube. T2K also has a well-studied beam flux, but it has a

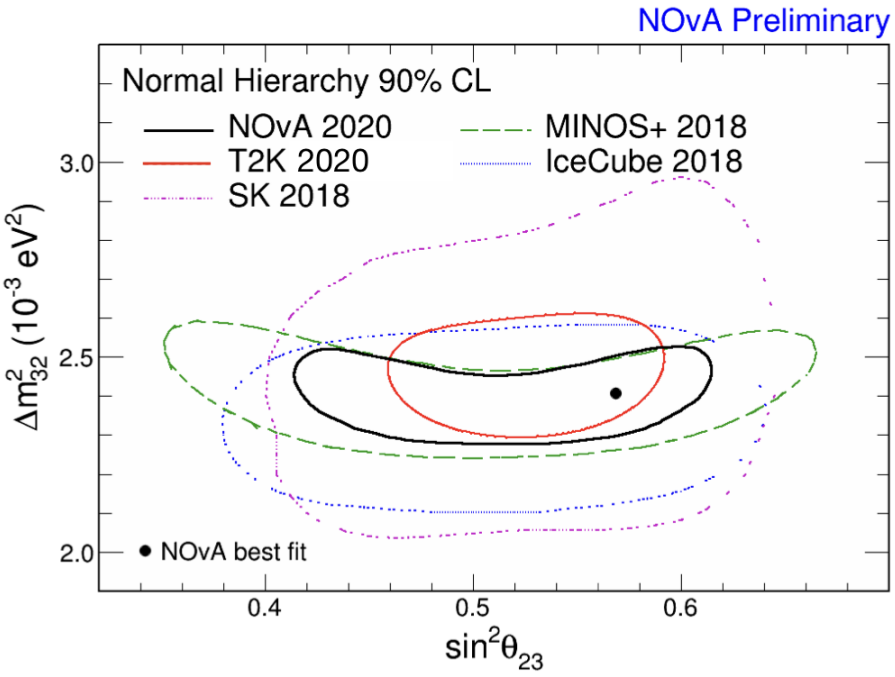

Figure 6.23. Contours of 90% C.L. for $\sin^2\theta_{23}$ and Δm^2_{32} space with colors representing different experiments

shorter baseline and incurs less matter effect from the Earth. So it is less constrained by the antineutrinos and slightly wider in the range of Δm^2_{32}. Another possible reason for the shape differences of the T2K and NOvA (and MINOS) contours is differences in the detector designs. The near detector of T2K is quite different from the far detector, which is the Super-K detector, while NOvA and MINOS each have a near and a far detector that are functionally identical, and their FD predicted MC simulations are corrected by using the ND data. MINOS and NOvA also share similar analysis techniques, which could be another reason that their contours have similar shapes. The NOvA best-fit point sits in the common area of all the regions. All the contours are compatible with each other, and with the maximal mixing point ($\sin^2\theta_{23} = 0.5$). The significance values of $\sin^2\theta_{32}$, Δm^2_{32}, and δ_{CP} after applying the FC method are plotted as 1D curves in Figure 6.24 [9].

The categorized systematic uncertainties are plotted in Figure 6.25 [9] as bar

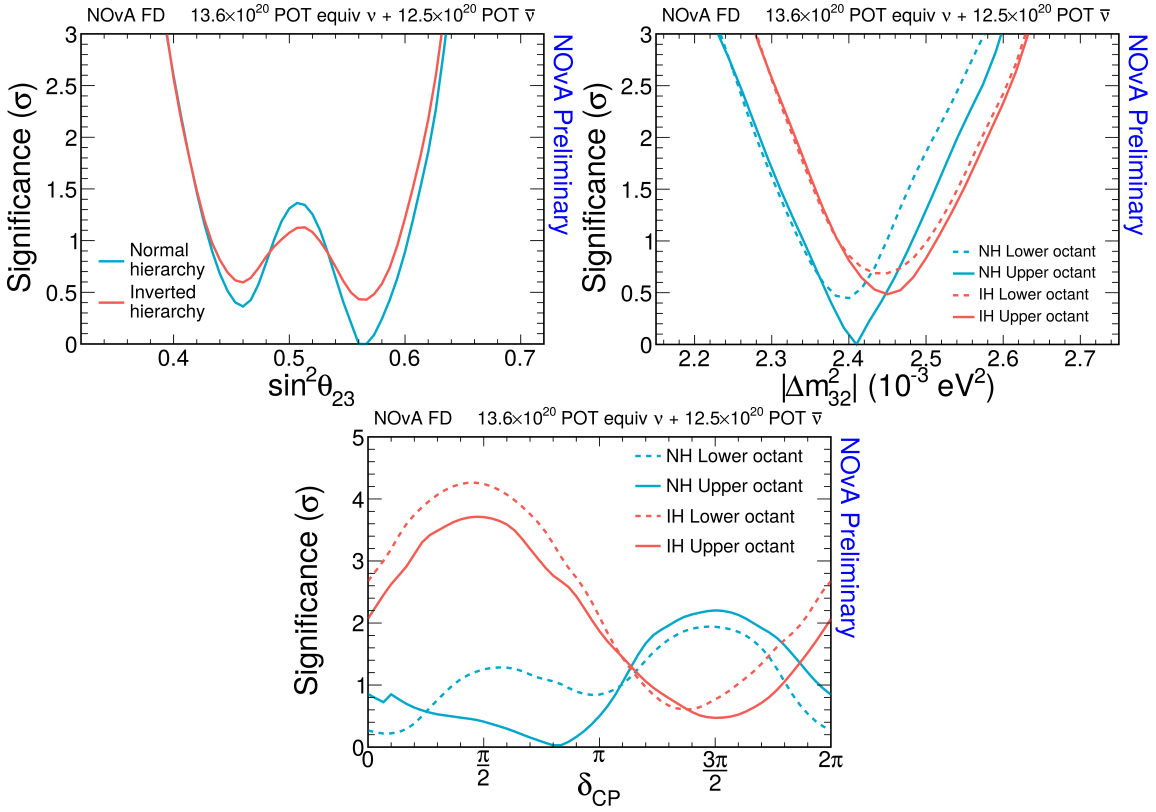

Figure 6.24. Significance vs. oscillation parameter values by assuming normal (blue) or inverted (red) mass ordering, or assuming $\sin^2\theta_{23} > 0.5$ (solid) or $\sin^2\theta_{23} < 0.5$ (dashed) after FC method is applied

charts to show their effects on the numbers of events for each analysis; the statistical uncertainties are also shown, and in all cases exceed the systematic ones. The systematic uncertainties are calculated as the differences of the number of predicted MC candidates with and without the systematics applied, divided by the number of predicted MC events without systematic uncertainties applied. As already described, the $\overset{(-)}{\nu}_\mu$ samples have higher statistics than the $\overset{(-)}{\nu}_e$ samples. As shown in Figure 6.25, the 1σ statistical uncertainty on the number of events in the selected ν_μ ($\bar{\nu}_\mu$) sample is approximately $\pm 6.7\%$ ($\pm 10\%$). For the ν_e ($\bar{\nu}_e$) analysis, this number is 10.5% (17%).

The categorized systematic uncertainty effects on the oscillation parameters are shown as the bar charts in Figure 6.26 [9]; the statistical uncertainties are also

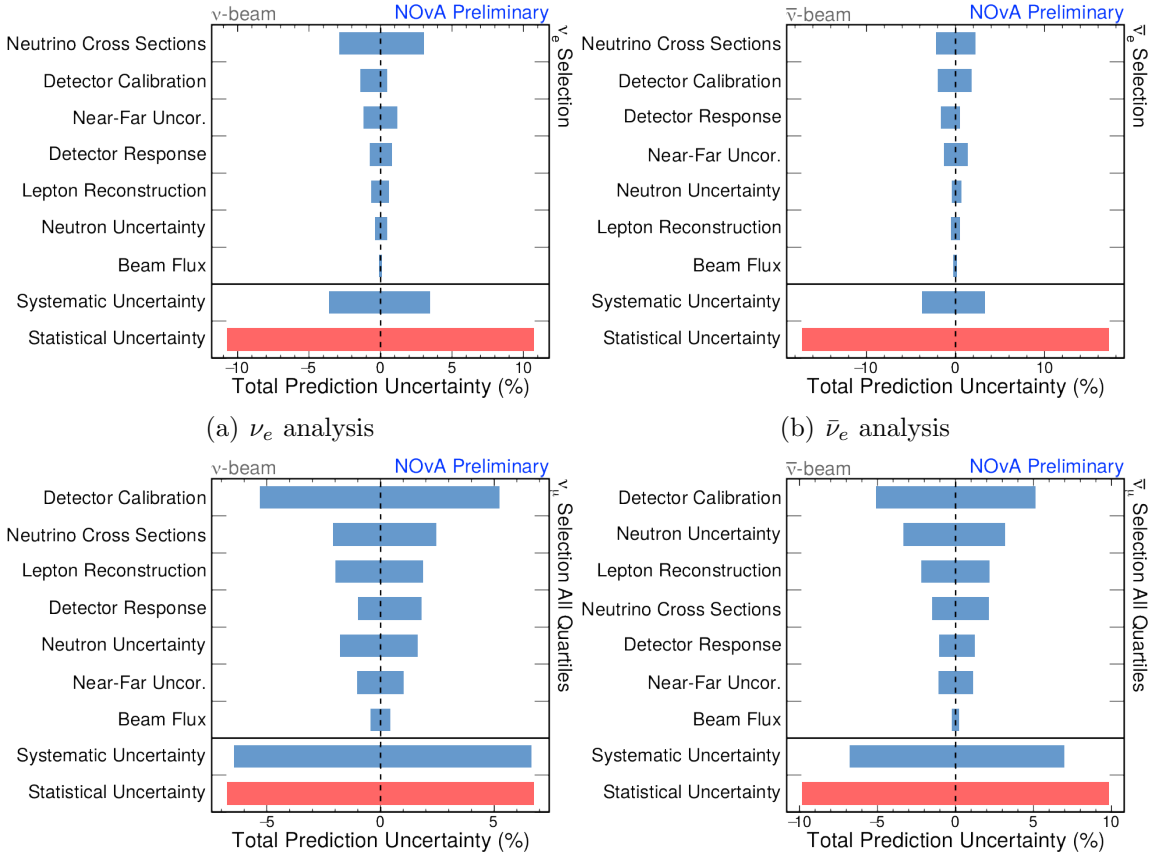

(a) ν_e analysis (b) $\bar{\nu}_e$ analysis

(c) ν_μ analysis (d) $\bar{\nu}_\mu$ analysis

Figure 6.25. Categorized systematic (blue) and statistical (red) uncertainties in numbers of events for predicted FD MC samples

shown, and in all cases exceed the systematic ones. These plots show that the uncertainties of all the parameters are still statistics dominated, and especially so for the δ_{CP} parameter. This is because δ_{CP} is mainly constrained by the ν_e and $\bar{\nu}_e$ appearance analyses, which have lower statistics than the ν_μ and $\bar{\nu}_\mu$ disappearance analyses. For all of the parameters, the largest systematic uncertainty is contributed by the detector calibration. Both $\sin^2\theta_{23}$ and Δm^2_{32} are mainly constrained by the ν_μ and $\bar{\nu}_\mu$ disappearance samples and are sensitive to the neutrino energy reconstruction, which heavily relies on the detector calibration. Thus, the calibration systematic uncertainty becomes the largest uncertainty in measuring these parameters compared to the remaining systematics, but the results are still statistics dominated. The functionally

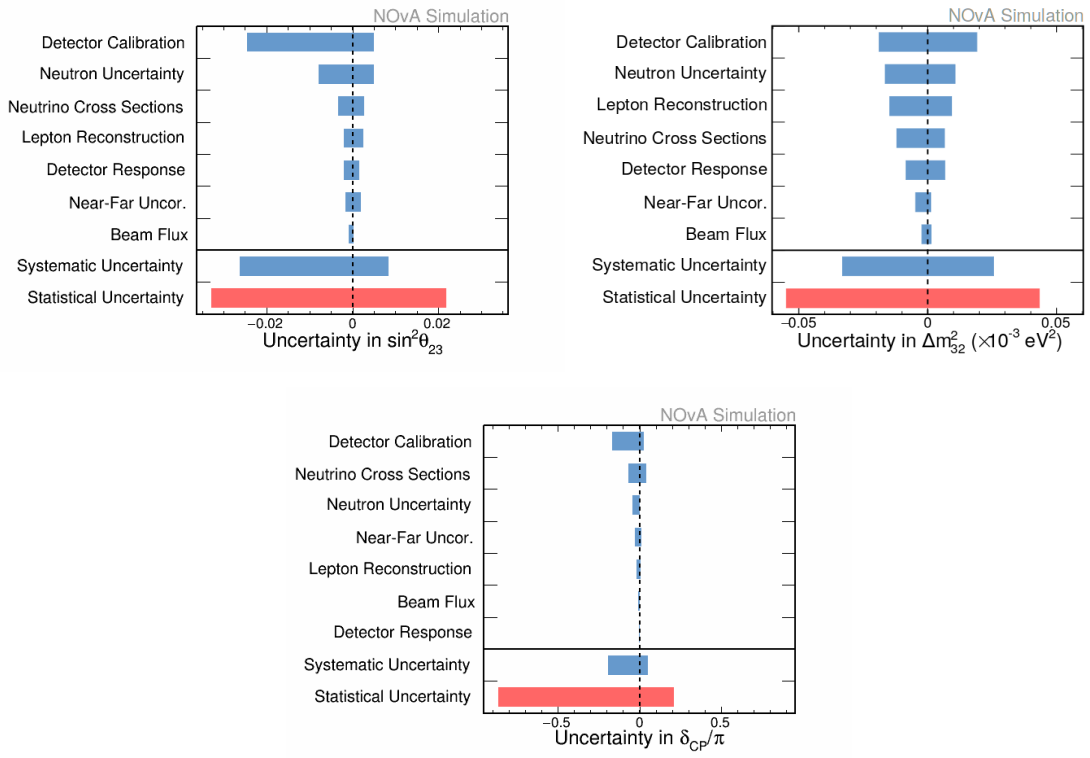

Figure 6.26. Categorized systematic (blue) and statistical (red) uncertainties in oscillation parameters for predicted FD MC samples

identical detector design, the background estimation techniques, and the extrapolation methods play an important role in reducing the systematic uncertainties in the oscillation analysis.

CHAPTER 7

CONCLUSION

The NOvA experiment has set new constraints on the oscillation parameters, θ_{23}, Δm^2_{32}, and δ_{CP}, by studying the four oscillation channels: $\overset{(-)}{\nu}_\mu$ disappearance and $\overset{(-)}{\nu}_e$ appearance. In this joint analysis, the NOvA detectors have been exposed to 13.61×10^{20} (12.54×10^{20}) protons on target (POT) when the NuMI facility was in the mode of running ν_μ ($\bar{\nu}_\mu$) beam. The neutrino dataset was collected during 2012–2020. The antineutrino dataset was collected during 2016–2018.

The ν_μ and $\bar{\nu}_\mu$ disappearance and ν_e and $\bar{\nu}_e$ appearance analyses set a powerful constraint on the values of θ_{23} and Δm^2_{32}, and the appearance analyses provide additional constraints on the value of δ_{CP}, to which the disappearance analyses are insensitive. The best-fit point is $\sin^2\theta_{23} = 0.57^{+0.03}_{-0.04}$, $\Delta m^2_{32} = 2.41^{+0.07}_{-0.07} \times 10^{-3}$ eV$^2/c^4$, and $\delta_{CP} = 0.82\pi$, where the 1σ interval of the δ_{CP} parameter is [0,1.06] $\cup$ [1.82,2]. Using the oscillation parameter values at the best-fit point, the FD predicted MC samples for $\overset{(-)}{\nu}_e$ and $\overset{(-)}{\nu}_\mu$ analyses are plotted in Figures 7.1 and 7.2 [9].

The oscillation dip region around $E = 1.8\,\text{GeV}$ corresponds to a maximal point of ν_μ disappearance probability, which is defined by

$$P(\nu_\mu \text{ disappearance}) \approx \sin^2(2\theta_{23}) \sin^2\left(\frac{1.27\Delta m^2_{32} L}{E}\right), \tag{7.1}$$

where L and E are the travel distance and energy of the neutrinos. A large $\sin^2(2\theta_{23})$ value corresponds to a bigger probability of ν_μ disappearing. The fine bins in the oscillation dip region give strong constraints on the values of Δm^2_{32} and $\sin^2(2\theta_{23})$. Compared to the unoscillated MC spectra, if more events disappear from the oscillation dip region, we will see a larger value of $\sin^2(2\theta_{23})$. The location of the oscillation dip determines the value of Δm^2_{32}, which determines the frequency of the disappear-

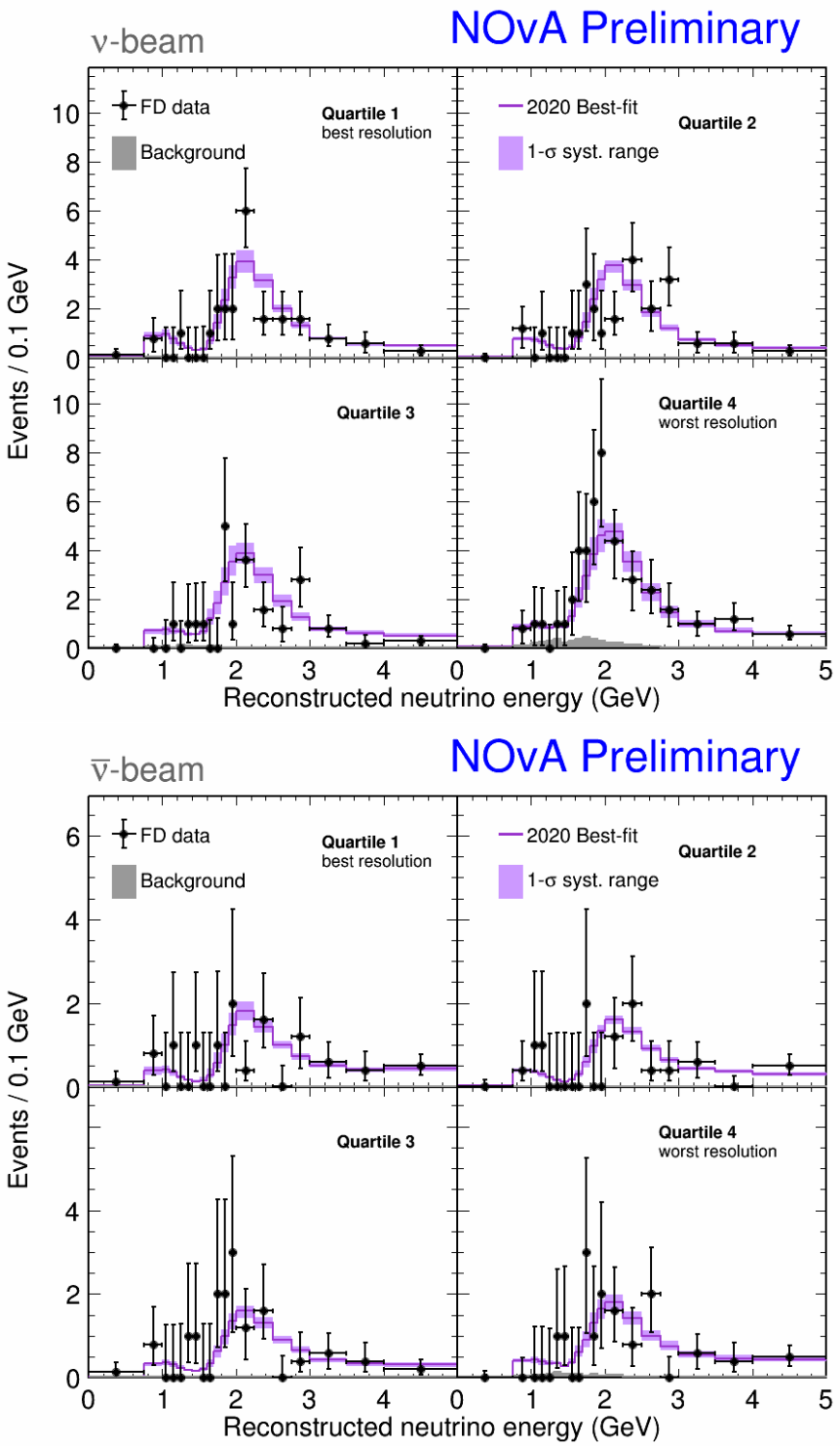

Figure 7.1. Distributions of ν_μ (top) and $\bar{\nu}_\mu$ (bottom) data and predicted MC samples at FD

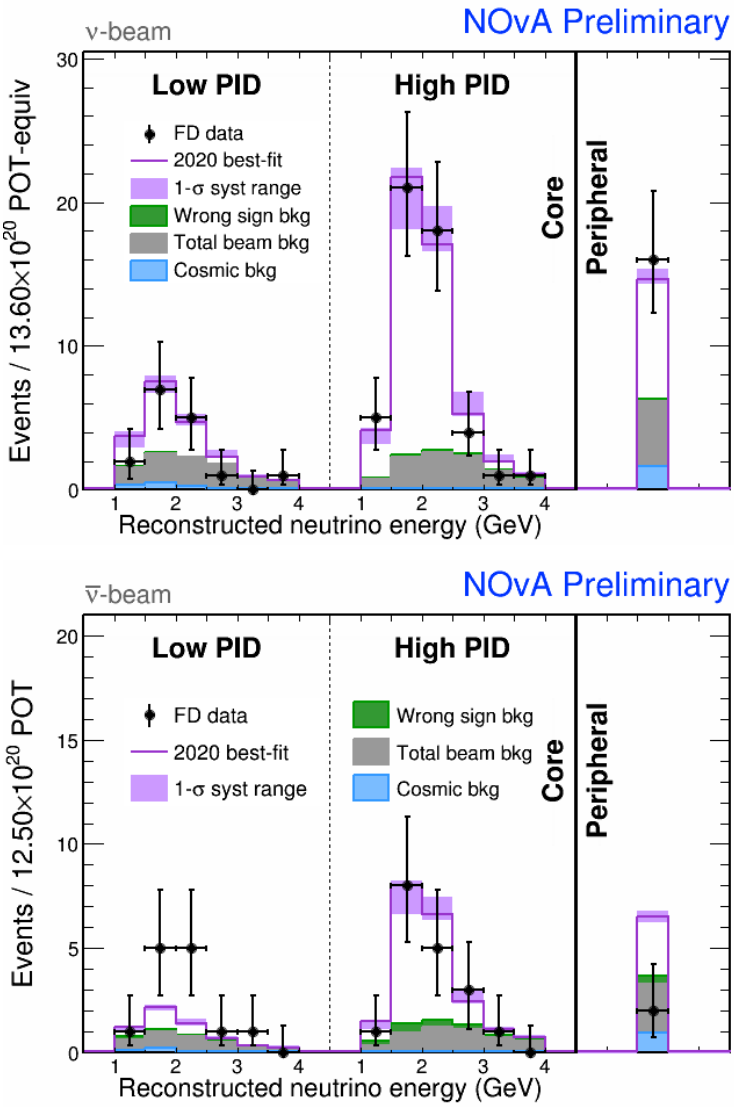

Figure 7.2. Distributions of ν_e (top) and $\bar{\nu}_e$ (bottom) data and predicted MC samples at FD

ance probability.

The $\overset{(-)}{\nu}_e$ appearance probability functions are more complicated and cannot directly show the values of the oscillation parameters as the disappearance probability functions do. Therefore, we use a probability plot with combined ν_e and $\bar{\nu}_e$ analyses as shown in Figure 7.3 to illustrate how the $\overset{(-)}{\nu}_e$ appearance analyses constrain the values of the oscillation parameters. The $\bar{\nu}_e$ and ν_e combined appearance probability curves traces out an ellipse as the value of δ_{CP} varies from 0 to 2π, and the position

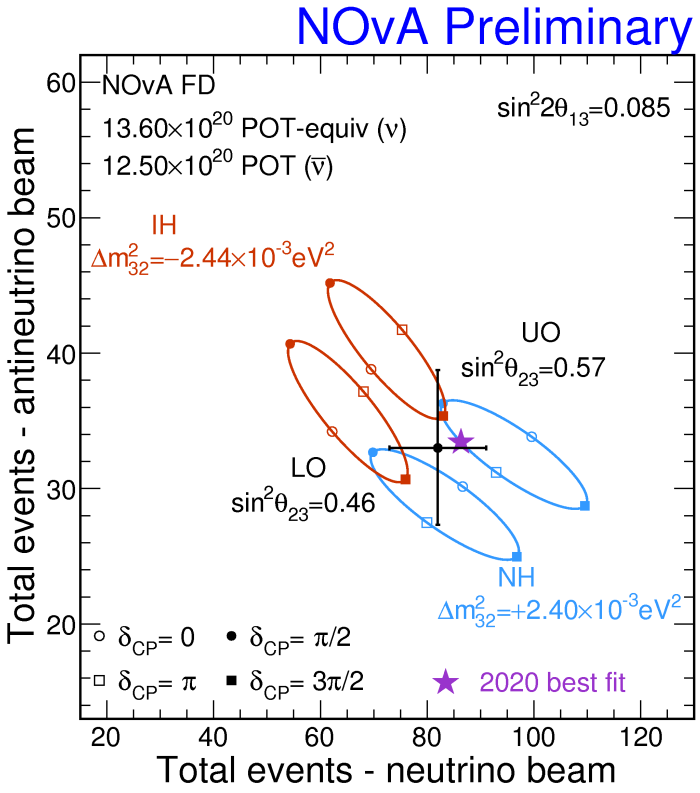

Figure 7.3. Electron antineutrino and neutrino combined appearance probability curves with normal (blue) and inverted (red) mass orderings, preferred values of the remaining oscillation parameters, observed data samples (black cross), and best-fit point (purple star) of NOvA 2020 analysis

of the ellipse on the plot depends on the mass ordering and the value of $\sin^2\theta_{23}$. The ellipses partially overlap in the region where the data point sits. The bars of the data point correspond to the statistical uncertainties of the data samples. The combined ν_e and $\bar{\nu}_e$ data samples disfavor regions of parameter space that are far from the data point. For example, in the inverted mass ordering, $\delta_{CP} = \pi/2$ is excluded by $> 3\sigma$; in the normal mass ordering, $\delta_{CP} = 3\pi/2$ is disfavored by approximately 2σ [19]. However, the current analysis is not sufficient to determine value of δ_{CP}.

The NOvA experiment will continue running through 2025, and anticipates achieving $> 3\sigma$ sensitivity to the mass ordering for 30–50% of the δ_{CP} range. The anticipated exposure of NOvA is 31.5×10^{20} for each of the neutrino and antineu-

trino datasets. The NOvA Test Beam program will improve the detector calibration systematic uncertainties. The joint analysis with T2K will further improve the sensitivity. In the longer term future, the DUNE and Hyper-K experiments will be able to observe CP-violation in some favored ranges of δ_{CP} values at up to the 5σ confidence level.

BIBLIOGRAPHY

[1] F. Reines and C. Cowan, Los Alamos Sci. **25**, 4 (1997).

[2] M. Goldhaber, L. Grodzins, and A. W. Sunyar, Phys. Rev. **109**, 1015 (1958).

[3] J. N. Bahcall and R. D. Jr., Science **191**, 264 (1976).

[4] Y. Fukuda et al. (Super-Kamiokande Collaboration), Phys. Rev. Lett. **81**, 1562 (1998).

[5] Q. R. Ahmad et al. (SNO Collaboration), Phys. Rev. Lett. **87**, 071301 (2001).

[6] K. Eguchi et al. (KamLAND Collaboration), Phys. Rev. Lett. **90**, 021802 (2003).

[7] S. Abe et al. (KamLAND Collaboration), Phys. Rev. Lett. **100**, 221803 (2008).

[8] D. S. Ayres et al., Fermi National Accelerator Laboratory report No. FERMILAB-DESIGN-2007-01, 2007.

[9] NOvA Official Plots Database, `https://nusoft.fnal.gov/nova/blessedplots`.

[10] S. M. Kasahara, Physics Procedia **37**, 1876 (2012).

[11] A. Norman, J. Phys.: Conf. Ser. **396**, 012035 (2012).

[12] O. B. Samoylova et al., in: *Proceedings of NEC 2019* (JINR, Dubna, Moscow Region, Russia, 2019), pp. 439-442.

[13] R. Brun and F. Rademakers, Nucl. Instrum. Meth. A **389**, 81 (1997).

[14] C. Hagmann et al., Lawrence Livermore National Laboratory Report No. UCRL-TM-229453, 2012.

[15] S. Agostinelli et al. (GEANT4 Collaboration), Nucl. Instrum. Meth. A **506**, 250 (2003).

[16] L. Aliaga et al. (MINERvA Collaboration), Phys. Rev. D **94**, 092005 (2016).

[17] R. E. Kalman, Physics Procedia **37**, 1876 (2012).

[18] N. Raddatz, Internal Document NOvA DocDB No. 11206, 2014. (unpublished)

[19] M. Baird, L. Suter, and J. Wolcott, Internal Document NOvA DocDB No. 44422, 2020. (unpublished)

[20] L. Fernandes and M. Oliveira, Pattern Recognition **41**, 299 (2008).

[21] M. Ohlsson and C. Peterson, Computer Physics Communications **71**, 77 (1992).

[22] R. Krishnapuram and J. M. Keller, IEEE Trans. Fuzzy Syst. **1**, 98110 (1993).

[23] E. Niner, Ph.D. thesis, Indiana University, 2015.

[24] M. Sandler et al., IEEE Conference on Computer Vision and Pattern Recognition **2018**, 4510 (2018).

[25] A. Collette, Python and HDF5 (O'Reilly Media, 2013).

[26] Keras, `https://keras.io` (2015).

[27] A collection of resources for training neural networks in NOvA, `https://github.com/novaexperiment/TensorFlowTrainingUtils/releases/tag/2Dprong` (2019).

[28] D. E. Rumelhart, G. Hinton, and R. Williams, Nature **323**, 533 (1986).

[29] Y. LeCun, L. Bottou, G. B. Orr and K. R. Müller, Neural Networks: Tricks of the Trade, (Springer, Berlin, Heidelberg, 1998).

[30] J. Long, Regression models for categorical and limited dependent variables, (SAGE Publications, Thousand Oaks, CA, 1997).

[31] R. Acciarri et al. (MicroBooNE collaboration), JINST **12**, 03011 (2017).

[32] D. Guest, K. Cranmer, and D. Whiteson, Annu. Rev. Nucl. Part. Sci. **68**, 1 (2018).

[33] S. Yu and Z. Djurcic, Internal Document NOvA DocDB No. 43814, 2020. (unpublished)

[34] P. Adamson et al. (NOvA Collaboration), Phys. Rev. Lett. **118**, 231801 (2017).

[35] M. A. Acero et al. (NOvA Collaboration), Phys. Rev. D **98**, 032012 (2018).

[36] F. Psihas et al., Phys. Rev. D **100**, 073005 (2019).

[37] K. Bays, Internal Document NOvA DocDB No. 11205, 2017. (unpublished)

[38] D. Torbunov, Internal Document NOvA DocDB No. 23342, 2017. (unpublished)

[39] L. Vinton, Ph.D. thesis, Sussex University, 2018.

[40] M. A. Acero et al. (NOvA Collaboration), Eur. Phys. J. C (to appear).

[41] A. Mislivec, Internal Document NOvA DocDB No. 44401, 2020. (unpublished)

[42] M. Tanabashi et al. (Particle Data Group), Phys. Rev. D **98**, 030001 (2018).

[43] K. K. Maan, H. Duyang, and S. R. Mishra, Internal Document NOvA DocDB No. 15081, 2016. (unpublished)

[44] C. Backhouse and A. Himmel, Internal Document NOvA DocDB No. 26699, 2018. (unpublished)

[45] P. Adamson et al. (NOvA Collaboration), Phys. Rev. Lett. **116**, 151806 (2016).

[46] S. S. Wilks, Ann. Math. Statist. **9**, 60 (1938).

[47] G. J. Feldman and R. D. Cousins, Phys. Rev. D **57**, 3873 (1998).

[48] C. Bassin, G. Laske, and G. Masters, EOS: Trans. Am. Geophys. Un. **81**, 897 (2000).